Lehrstuhl E15
Physik - Department

# A new approach to NTLE cryogenic light detectors

Master Thesis

Elizabeth Mondragón

Technische Universität München

TECHNISCHE UNIVERSITÄT MÜNCHEN

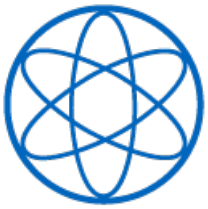

FAKULTÄT FÜR PHYSIK
LEHRSTUHL E15

Master's Thesis

# A new approach to NTLE cryogenic light detectors


| | |
|---|---|
| Author: | Elizabeth Mondragón |
| Supervisor: | Prof. Dr. Stefan Schönert |
| Advisor: | Dr. Xavier Defay |
| Submission Date: | December 12, 2016 |

I confirm that this master's thesis is my own work and I have documented all sources and material used.

Munich, December 12, 2016 Elizabeth Mondragón

**Abstract**

The purpose of this master's thesis is to improve the performance of cryogenic light detectors, such as those used in the CRESST experiment, by taking advantage of the Neganov-Trofimov-Luke Effect (NTLE). This effect enhances the thermal signal of particle interactions in a semiconductor absorber operated at cryogenic temperatures by drifting the electron-hole pairs created within an electric field. One of the main problems with such detectors comes from an incomplete charge collection. I present here the results obtained with a new type of NTLE detector using implanted contacts to improve the charge collection within the semiconductor.

# Contents

# Chapter 1

# Introduction

The existence of dark matter in the Universe is today commonly admitted in modern cosmology and astrophysics. However, its nature remains a mystery. It is estimated that 27% of the energy density of the universe consists of DM. To understand more about this significant part of the universe, it is necessary to analyse the evidence and determine what research approaches are the most advantageous. One possibility to determine the nature of dark matter is to measure the direct interaction of dark matter in detectors based on earth.

One of these dark matter direct detection experiments is CRESST - Cryogenic Rare Event Search with Superconducting Thermometers. The study developed in this thesis is motivated in the framework of CRESST. The CRESST experiment benefits from a particle discrimination mechanism called phonon-light technique. This double channel discrimination mechanism is a highly efficient active background suppression technique and is therefore very often used in cryogenic rare event search experiments in both the fields of Dark Matter and neutrinoless double beta decay ($0\nu\beta\beta$).

The phonon-light technique is based on the simultaneous measurement of the heat signal in a cryogenic phonon detector (a scintillating crystal) and a light signal with a separate cryogenic light detector. For CRESST-III, about 6% of the deposited energy is then transformed into light and 30% of this light is then detected by the photon detector.

The current aim of the CRESST experiment is to drastically decrease its detection threshold. The particle discrimination increases when the resolution of the light detector improves. A high energy resolution on the light detector is thus crucial in order to have a very good discrimination down to the threshold. The Neganov-Trofimov-Luke-Effect (NTLE) is an effect which enhances the heat signal in the light detectors allowing to improve the signal-to-noise of the measurement. This idea prompts the study and possible implementation of the NTLE for the light detectors.

One of the main problems with NTLE-detectors comes from an incomplete and unreliable charge collection. In this thesis, a new type of NTLE detector was developed and studied taking advantage of the implanted contacts.

Results of experiments with optical photons and X-rays are reported with the aim of determining the thermal gain of the NTLE and the evaluation of the signal-to-noise improvement. The charge collection was simultaneously studied with the phonon signal by measuring charge signal with a charge amplifier. Additionally, the influence of a metallic layer on the bandwidth of the phonon signal was studied.

# Chapter 2

# Dark Matter

The existence of dark matter (DM) in the Universe is today commonly admitted in modern cosmology and astrophysics. At different scales in the Universe, there is compelling evidence for dark matter in dwarf galaxies, spiral galaxies, and galaxy clusters as well as at cosmological scales. However, its nature remains a mystery. It is estimated that 27% of the energy density of the universe consists of DM. To understand more about this significant part of the universe and to unravel the mysteries around it, it is necessary to analyse the evidence and determine what research approaches are the most advantageous. Dark matter is invisible to telescopes; yet it is still possible to study it through its gravitational interaction. Nevertheless, the direct detection of DM is crucial because that would be a way to determine its nature. Many methods of both direct and indirect detection have been developed and are currently in progress. Alternatively, accelerator experiments are conducted to try to create DM (see chapter 3). Despite all these complementary efforts, dark matter has not yet been detected. Thus it is necessary to pursue its search with all means available to us.

## 2.1 Evidence

The name *Dark Matter* comes from the fact that DM does not absorb or emit electromagnetic radiation, and is therefore *dark*.

The Standard Model of cosmology describes the universe as constituting of 68.3% dark energy, of 26.8% dark matter and only of 4.9% of baryonic matter [1]. Therefore, DM constitutes 84.5% of the total mass of the universe. DM dominates, and consequently exerts important gravitational effects. The existence and properties predicted for DM are thus inferred from astronomical observations of its gravitational effects, some of which will be discussed in section 2.2.

## Velocity of galaxies in clusters and rotation curves of spiral galaxies

In 1933, F. Zwicky [2] suggested for the first time the existence of DM. He based that hypothesis on an unexplainable gravitational effect at the edge of the Coma galaxy cluster. By applying the virial theorem he inferred that some unseen matter must be providing the mass needed to hold the cluster together via gravitational attraction for such fast orbits.

Later on, in the 1960s, V. Rubin [3] provided further evidence of such hidden mass. Rubin measured the rotation curve on spiral galaxies with greater accuracy. From the measurement of these velocities, the total mass of the galaxy could be calculated according to the virial theorem. Comparing the calculated mass with the observed luminous matter, she found a huge discrepancy leading to a mass much larger than the one observed.

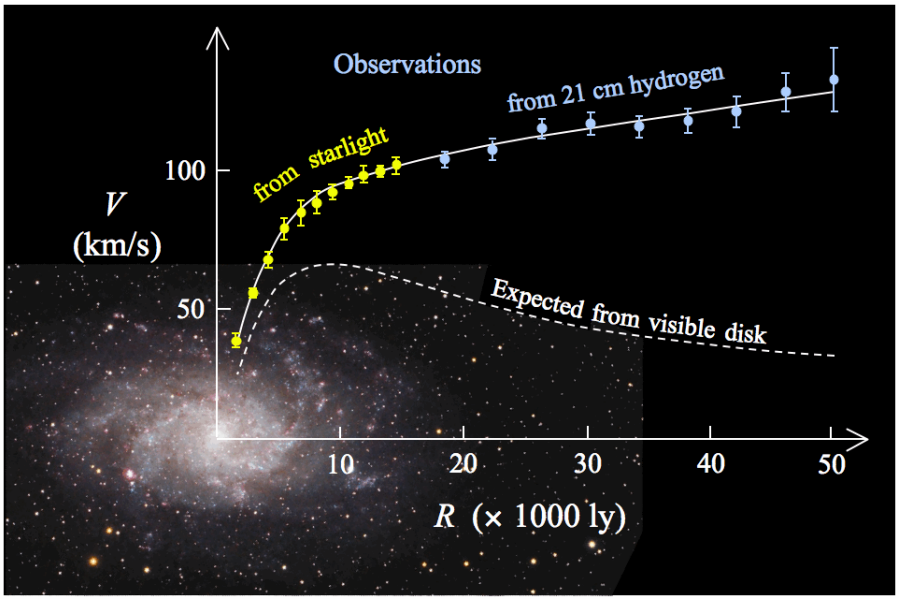


Figure 2.1: Graphic of the rotation curve of the typical spiral galaxy. Galaxy M33 in the background. Source: [5].

Despite the later discovery of the presence of hot gas through X-ray telescopes, there is still a missing mass of about 10 times the visible matter (luminous plus gaseous) to account for the calculated velocities [4]. Moreover, there was another troubling unexplained fact: the gravitational force produced by the luminous matter would not be enough to bind the hot gas to the cluster.

To account for the observed motion, DM must be symmetrically distributed in a big halo around the galaxies. The luminous matter would be then confined in a central disc surrounded by the DM-halo (see fig. 2.2).

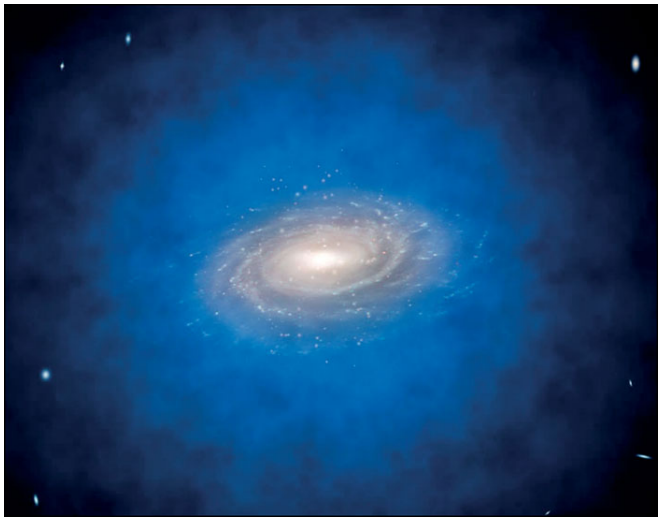

Figure 2.2: Artistic image of the Milky Way, embedded in a spherical halo of dark matter (shown in blue). Source: [6].

## Cosmic microwave background radiation

The CMB is a picture of the earliest light of the universe. This light comes from when the universe was 380.000 years old. It shows tiny temperature fluctuations corresponding to regions with slightly different densities. Those fluctuations are, in turn, the origin of all the future structures in the universe [10].

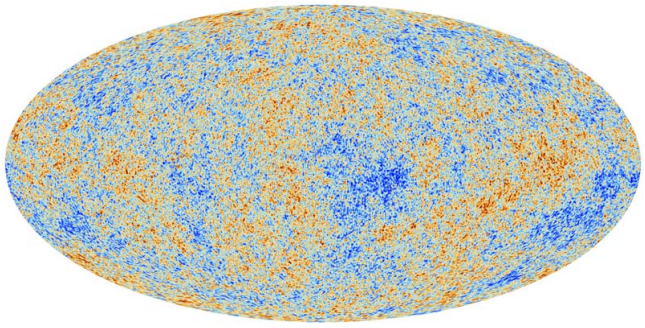

Figure 2.3: The anisotropies of the Cosmic microwave background (CMB) as observed by Planck. The CMB is a snapshot of the oldest light in the Universe, imprinted on the sky when the Universe was just 380,000 years old. It shows tiny temperature fluctuations that correspond to regions of slightly different densities, representing the seeds of all future structure: the stars and galaxies of today. Source: [11].

CMB-photons come from the moment when the Universe became transparent. This happened when the Universe expanded and cooled enough for the free charges to recombine into hydrogen. At that moment (T$\simeq$ 3000 K), there was no longer Thompson scattering off electrons and protons; photons decoupled leading to hardly

any interaction between radiation and matter.

The CMB constitutes a close to perfect black body spectrum due to the thermal equilibrium before the decoupling. The average temperature of the CMB today is 2.725 K [7]. The characteristics of the small deviation from the absolute isotropy and homogeneity, of the order of $10^{-5}$, indicate the presence of DM with a density ($\Omega_{DM} = 0.268$). These inhomogeneities, caused by gravitational red-shifts, lead to the large-scale structures of the visible matter. In order to model properly the evolution of these structure in time and reproduce the current observation of the Universe, a non-baryonic component of the matter is necessary [8, 9].

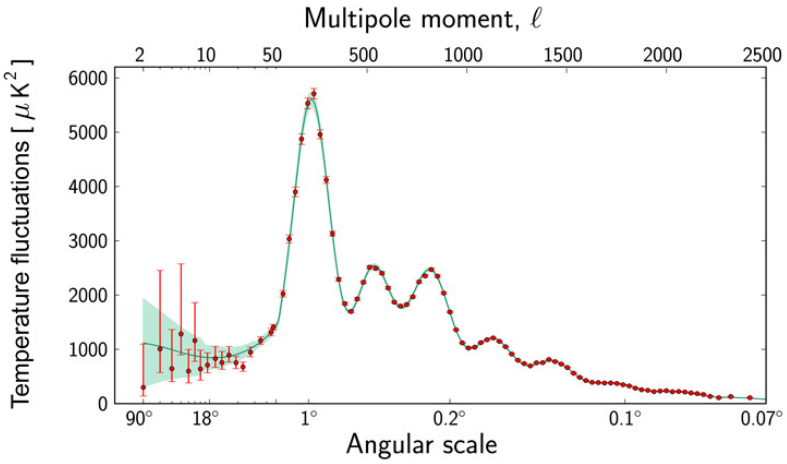


Figure 2.4: This graph shows the temperature fluctuations in the Cosmic Microwave Background detected by Planck at different angular scales on the sky. This curve is known as the power spectrum. The largest angular scales, starting at angles of ninety degrees, are shown on the left side of the graph, whereas smaller and smaller scales are shown towards the right. (For comparison, the diameter of the full Moon in the sky measures about half a degree.) The red dots correspond to measurements made with Planck; these are shown with error bars that account for measurement errors as well as for an estimate of the uncertainty that is due to the limited number of points in the sky at which it is possible to perform measurements. This so-called cosmic variance is an unavoidable effect that becomes most significant at larger angular scales. The green curve represents the best fit of the 'standard model of cosmology' – currently the most widely accepted scenario for the origin and evolution of the Universe – to the Planck data. The pale green area around the curve shows the predictions of all the variations of the standard model that best agree with the data. Source: [11].

## The Bullet Cluster and gravitational lensing

The bullet cluster (1E 0657-558) is the name given to a collision of two clusters and represents one of the most popular arguments for the existence of DM. The evidence of DM can be deduced from the two-in-one picture of the collision, in which the event is seen through an X-rays telescope and by gravitational lensing [12].

When the clusters collide, the stars, the gas and the DM would interact differently. For the stars, the major outcome of the collision is that they will slow down due to the gravitational effects but will be not otherwise altered. For the gas the behaviour is much more pronounced. The gas, which is basically baryonic matter, can be seen through the X-ray window since it also interacts electromagnetically. The response for DM is observed via gravitational lensing from background objects. The light from these background objects is bent when passing by a massive object. Hence, gravitational lensing provides the gravitational potential out of optical images.
It would be expected that the distorted images from the background were out shaped in the region of the baryonic visible matter. However, as it can be seen in fig. 2.5, the most massive area does not correspond to the baryonic matter one. The X-ray signal from the baryonic matter and the gravitational lensing signal from dark matter are clearly separated in these colliding clusters. Gravitational lensing occurs around the cluster collision, a place where nothing can be seen. This does not only show that indeed there is some invisible massive matter there, but also, that this matter must interact gravitationally. The observations do not exclude that DM can also interact via the weak interaction.

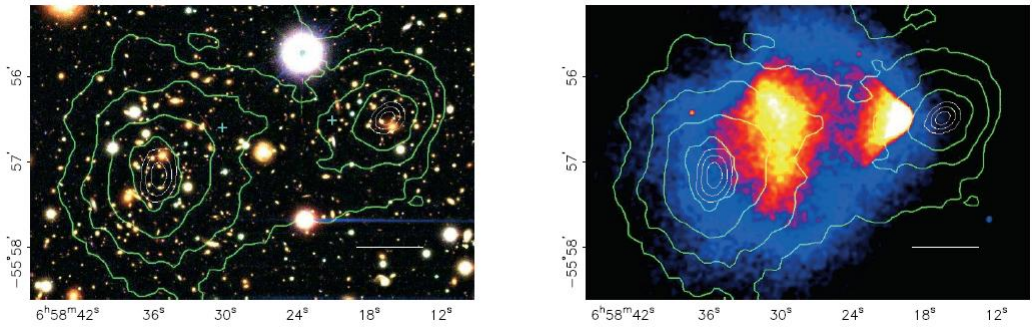


Figure 2.5: X-ray photo by Chandra X-ray Observatory of the Bullet Cluster (1E0657-56). Based on today's theories this shows the cluster to be about 4 billion light years away. In this photograph, a rapidly moving galaxy cluster with a shock wave trailing behind it seems to have hit another cluster at high speed. The gases collide, and gravitational fields of the stars and galaxies interact. When the galaxies collided, based on black-body temperature readings, the temperature reached 160 million degrees and X-rays were emitted in great intensity, claiming the title of the hottest known galactic cluster. Studies of the Bullet cluster, announced in August 2006, provide the best evidence to date for the existence of dark matter. Source: [15].

## 2.2 Candidates

From the four known fundamental forces that dark matter could interact with, the electromagnetic one is out of consideration. Clearly, DM needs to be electrically neutral, otherwise the electromagnetic emission or absorption of radiation would have probably been detected.

Considering also the evidence previously presented, it is understood that DM interacts gravitationally.

On the other hand, nothing observed so far prohibits DM to interact weakly. Hence, this becomes a reasonable assumption for the DM search. It can can also be assumed that the interaction rate of a possible DM-particle is very low or it would have conceivably been already observed. Also, it has to be colour-neutral to not interact via the strong force.

Another assumption that can be made is that DM is *Cold Dark Matter*. *Hot Dark Matter* implies that the possible DM-particles were relativistic at the time of the structure formation. This alternative has been excluded based on the fact that clumps of certain sizes impossible to achieve under a *Hot Dark Matter* Universe have been observed. The density fluctuations would have evened up in less time that the one needed to form these clumps.

Dark matter has to be present both in the early universe and today: if this were not the case, the evidence presented could not be explained. This means DM candidates have to be stable (lifetime equal to the age of the Universe) or following a production mechanism. However, the DM density has somehow been reduced.

Some possible DM candidates have been postulated that fulfill these requisites. Among them are axions, gravitinos, the Kaluza-Klein particles, MACHOs, asymmetric DM and the WIMPs, to mention the most popular ones. In this work some of these candidates will be discussed in more detail for being in the context of the CRESST experiment (see chapter 4). For further information about this topic see [13] or [14] for example.

### Weakly Interacting Massive Particles

WIMPs are hypothetical particles motivated by the Supersymmetry theory. They belong to the non-baryonic cold dark matter candidates. They would interact only via the weak and the gravitational forces with the surrounding matter. WIMPs are expected to be gravitationally bound in a roughly isothermal halo around the visible part of our galaxy with a density of about 0.3 GeV/cm$^3$ [14] at the position of the Earth. Cryogenic experiments, such as CRESST, are dedicated to its detection since they are well adapted to the small energy deposit a WIMP would leave. Their interaction with ordinary matter is expected via elastic scattering off nuclei. The elastic

nuclear scattering can occur via coherent ("spin independent") or spin-dependent interactions. For the coherent case, is expected a dependence in the cross section as $A^2$ [24], favoring heavy nuclei.

## Low-mass DM particles

Driven by the so far no-detection in the search for heavy DM, some other alternatives need to be considered. According to most theories, the cross-sections for DM collisions with nucleons are very small. This implies the need of experiments with huge volumes containing ordinary matter particles to attempt its detection.

Hence, it is interesting to study low-mass DM using experiments meanwhile the door for alternatives to the heavy DM is still open. The CRESST experiment is currently also exploring the region of low mass WIMPs with the aim of pursing the search in a direction that might bring some new results. Cryogenic experiments are particularly well suited for low mass dark matter because they have a very low threshold which is required for the detection of low mass wimp (see section 5.1).

Axions and sterile neutrinos are also typically considered in the search for low mass DM. These particles decay very slowly or they annihilate producing mono-energetic X-rays. The X-rays could be regarded as a smoking gun signature for such a type of DM.

Recently, a detection of a line signal at 3.6 keV [16, 17] has attracted the attention of the community, but it still needs to be verified before it can be claimed as a discovery. Other experiments like dedicated satellite experiments have set the limits for its existence excluding a great part of the parameter space directly or indirectly, leaving a small range in which such a particle could exist [18].

## Asymmetric DM

There is yet another issue related with the standard WIMP; the WIMP paradigm. In it, the densities of DM and baryonic matter are not necessarily related to each other in the way $\rho_{\mathrm{DM}}/\rho_{\mathrm{B}} \simeq 5$. In the WIMP freeze-out paradigm $\rho_{\mathrm{DM}}$ is fixed meanwhile the annihilation rate drops because of the Hubble expansion [19, 20].

The DM density in the universe today is related to the annihilation cross-section. The baryon density is set by CP-violating parameters and out-of-equilibrium dynamics associated with baryon number violating processes occurred during the baryogenesis. Therefore, the quantities that set each of these densities are unrelated. Due to the proximity of both energy densities, this non-relation seems surprising. Hence, it is suggested that dynamics plays a role tiding up both densities.

From this relation, the idea of DM having an asymmetry in its matter density

over its anti-matter density, comes naturally. DM matter asymmetry could be then directly connected to the baryonic asymmetry.

# Chapter 3

# Unravelling the nature of Dark Matter

The search for dark matter uses three different and complementary determination methods: direct and indirect detection experiments, and synthesis in particle accelerators. The direct detection experiments use deep underground facilities aiming at the scattering of DM particles off nuclei in terrestrial detectors. The indirect detection experiments look for the products of dark matter particle annihilation. Particle accelerators look for missing transverse energy after collisions that match the energy corresponding to a dark matter particle. Accelerators can set a value for the mass, while the others cannot and require a prior range for the mass of to search for. In this chapter a brief introduction to these three methods is given.

## 3.1 Synthesis mechanisms in accelerators

In particle colliders such as the Large Hadron Collider (LHC), dark matter particles could be generated by the collision of Standard Model particles at high energies. One type of DM-matter particle candidate that could be generated in such a way are WIMPs. WIMPs would not interact with the detector after being created. By analysing the missing transverse energy, it is possible in principle to infer the existence of a certain particle with defined properties, even without actually detecting the particle itself.

A drawback of using particle detectors is that it is not possible to prove that the dark matter particles have a lifetime longer than the age of the universe. Nevertheless, they provide an important input for the other two approaches setting the general mass scale of these beyond-the-standard-model particles.

No conclusive results have been achieved at the moment using particle accelerators.

## 3.2 Indirect DM detection

The indirect detection experiments search for the products of DM-annihilation. Experiments of this kind (PAMELA, Fermi Gamma-Ray Space Telescope, MAGIC, HESS...) peer at regions expected to have a high DM-density like the galactic centre, galaxy clusters or dwarf spheroidal galaxies.

In the dark matter annihilation Standard Model particles can be created. Some of the particles searched for from this annihilation are positrons, anti-protons and $\gamma$-rays (see fig. 3.1). Positrons and anti-protons are not abundant in the cosmic rays due to the baryon asymmetry of the universe.

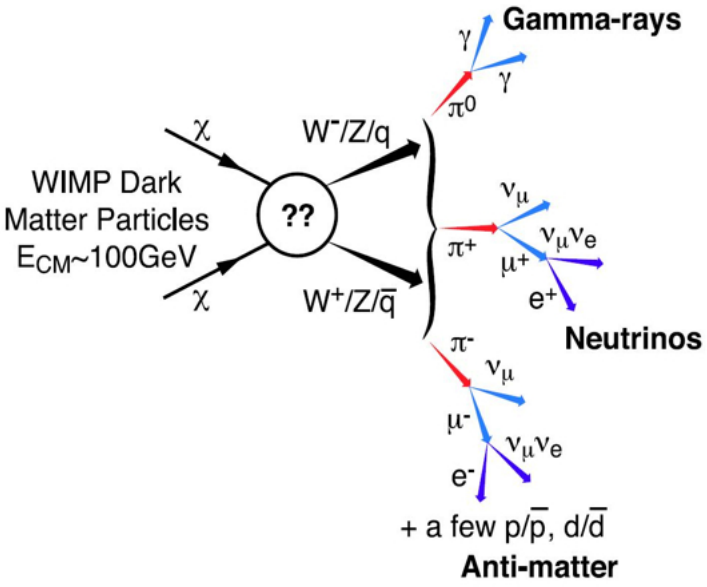


Figure 3.1: It can be seen in this graphic the annihilation process for dark matter particles. When a DM particle and antiparticle annihilate secondary particles are produced: $\pi^0$, $\pi^-$ or $\pi^+$. These products decay emiting gamma-rays, neutrinos or antimater. Source: [21].

Neutrinos are other possible source of information in this respect. When neutrinos scatter in the interior of the sun or the Earth, they get trapped by gravitational effects. They therefore enhance the density and thus the annihilation rate therein [33] producing a signal in the form of neutrino flux. This effect it is not negligible because the annihilation rate grows quadratically with the number of DM-particles. Meanwhile strongly and electromagnetically interacting particles would be stopped in the interior of the sun, while neutrinos would escape easily. Hence, detecting high energetic neutrinos coming from the sun would be a very remarkable verification of this process. Moreover, this detection would allow estimating the mass of the dark matter particle annihilating. Example of experiments searching for this sort of neutrinos are IceCube and ANTARES.

Neutrino telescopes can compete when targeting spin-dependent or no-coherent scattering of dark matter. Particularly, protons (spin -1/2) coming from the sun that consists of $\sim 71\%$ hydrogen.

As mentioned already, the annihilation rate of DM-particles has a quadratic dependence with the density and this is an important feature for indirect detection. It has been discovered using numerical simulations that galactic halos contain a great number of "sub-halo". This means that there is a great potential for discovering dark matter particles through their annihilation into $\gamma$-rays, another target mentioned before. This is very convenient because due to their high energy, they point back at the location where the annihilation took place. They do not scatter or are absorbed either because the cross section for scattering on electrons and nuclei is very small for energies going from GeV to TeV.

One way to distinguish photons coming from dark matter origin is by analysing the energy distribution resulting from these astrophysical processes. These photons are limited by the rest mass of the annihilating particle. The annihilating particles are expected to annihilate at rest mass, estimated to be $v/c = 10^{-3}$, which means that the photons will emerge back-to-back each with an energy $E_\gamma = m_\chi$. This is the signature to look for to track these photons.

Recently, the Fermi collaboration has started to probe the interesting WIMP region by stacking data from several dwarf galaxies and also from observations around the vicinity of the galactic center [21].

## 3.3 Direct DM detection

The dark matter interaction is expected to be very rare. The direct detection technique aims at the detection of DM-particles from their scattering off nuclei. Due to the very low expected rate of DM-particles passing through the Earth, these experiments are located in deep underground laboratories to reduce the cosmic background as much as possible. The signal induced by the nuclear recoil can be measured in several ways: ionization signals, phonon signals and scintillation signals. These experiments usually employ simultaneously two of these ways to make a particle discrimination.

Examples of experiments that use a two channel readout are Cryogenic Dark Matter Search (CDMS) [34], Cryogenic Rare Event Search with Superconducting Thermometers (CRESST) [36], EDELWEISS [40],XENON100 [38] and Large Underground Xenon (LUX [39]) among the most important ones.

The results from the search of dark matter experiments are commonly displayed in the exclusion plots (see fig. 3.2). These plots show the WIMP-nucleon cross sec-

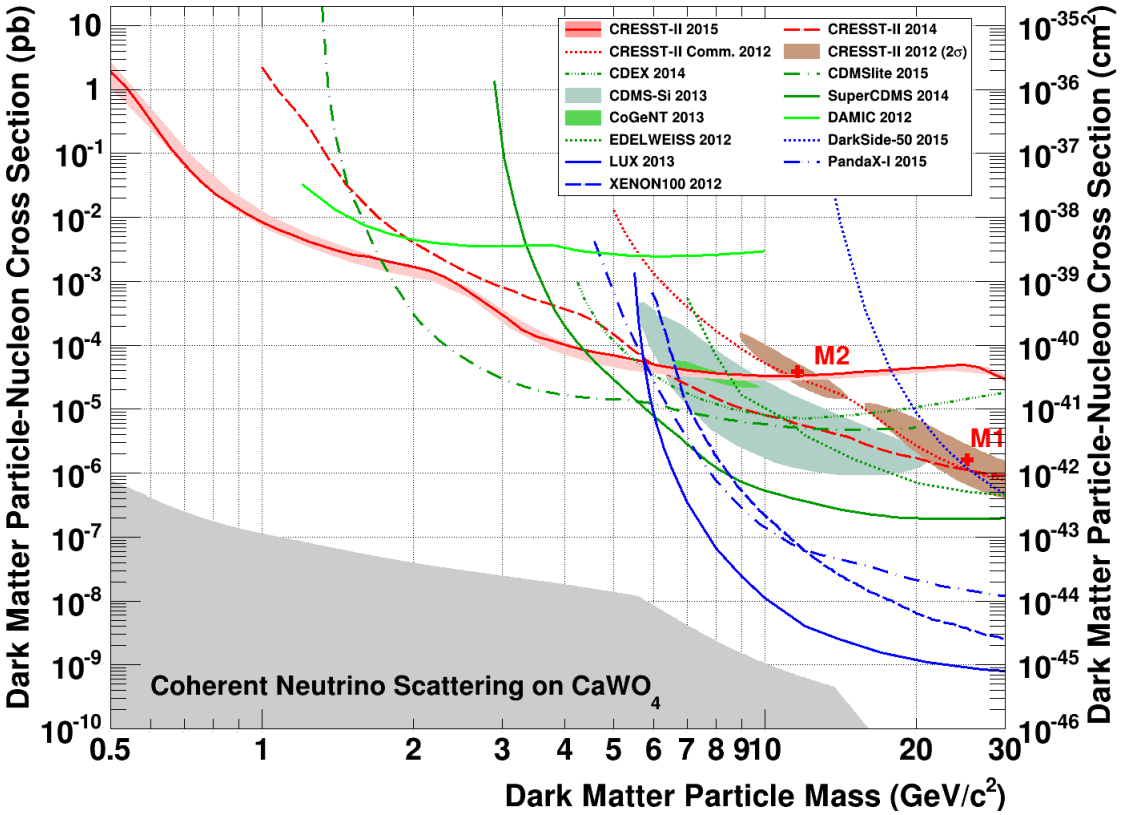


Figure 3.2: Dark matter exclusion plot. This plot shows the WIMP-nucleon cross section versus the mass of the WIMP. The solid and dashed lines are exclusion limits set by the different experiments which did not detect a WIMP signal – the parameter space above is excluded. The grey area is the limit for the coherent neutrino scattering. Source: [36].

tion versus the mass of the WIMP. The islands represent the experiments that claim the detection of a WIMP signal. The solid and dashed lines are exclusion limits set by the different experiments which did not detect a WIMP signal – the parameter space above is excluded. The grey area is the limit for the coherent neutrino scattering.

Some experiments, such as DAMA/Libra or CoGeNT, have claimed the detection of a WIMP signal. [41, 42]. Experiments like XENON100, LUX, SuperCDMS, CDMSlite, EDELWEISS, and CRESST-II phase 2 reported though a negative result (see for example [43, 44, 45]).

According to the evidence (section 2.1) dark matter is located in a halo surrounding our galaxy. These particle would travel in the Solar System passing through Earth at galactic velocities of 200 km/s. This velocity corresponds to a v/c ratio of $10^{-3}$, as mentioned in the previous section. It is possible to model the Milky Way rotation curve to obtain that the local mass density of DM should be 0.3 GeV/cm$^3$.

Knowing the velocity and density of the DM passing through Earth, for supersymmetric WIMPs the scattering cross-section is calculated to be in the order of $10^{-8}$ pb.

Direct detection experiments have increased enormously in sensitivity during the last few years, especially in the low-mass range (below 100 GeV mass). This is the case for CRESST that aims to detect rare events using a combination of scintillation and phonon signals (see chapter 4). Another example of this kind is the CDMS experiment that uses ionization signals combined with heat signals.

At high mass, direct detection experiments using terrestrial targets are no longer that sensitive. The rate of DM-particles is proportional to the DM-flux from the halo ($n_\chi = \frac{\rho_\chi}{m_\chi}$). Therefore, the higher the mass the lower the sensitivity for these candidates.

# Chapter 4

# The CRESST Experiment

The Cryogenic Rare Event Search with Superconducting Thermometers (CRESST) [36] is located at the Laboratori Nazionali del Gran Sasso (LNGS) in Italy, under 1400 m of rock that serves as shielding from cosmic rays for the rare-event search.

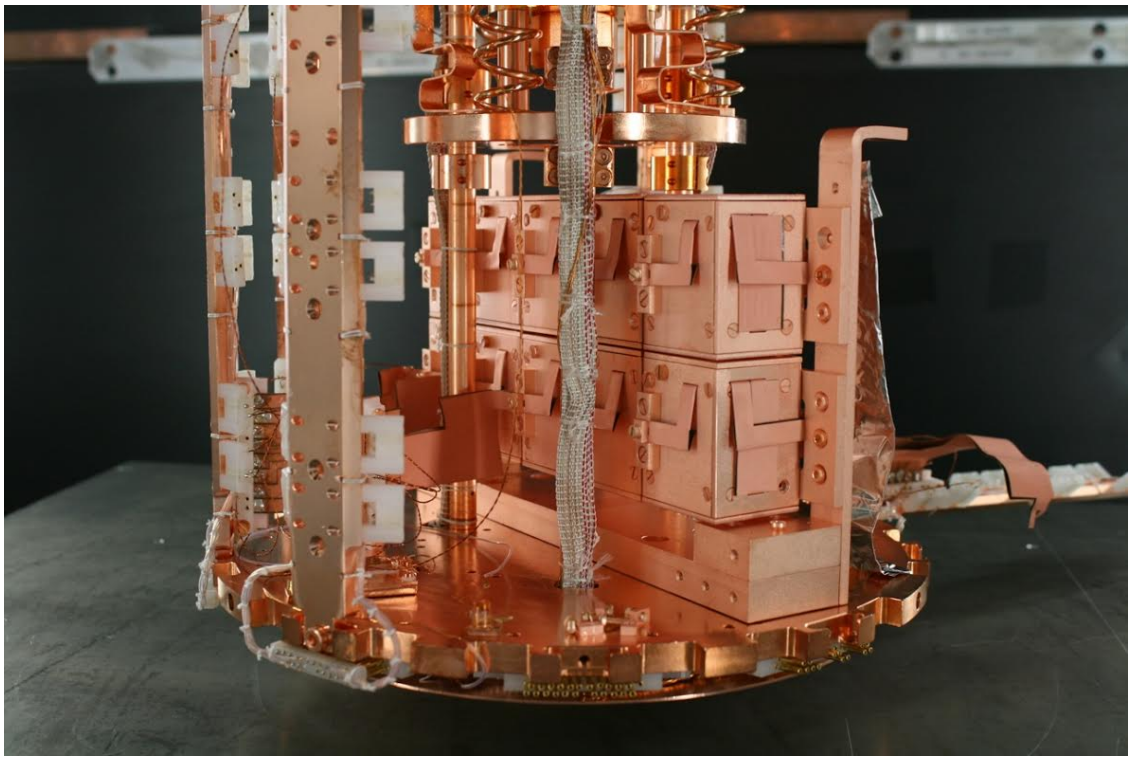

Figure 4.1: Ten modules mounted in the carousel inside the CRESST cryostat at the LNGS for the CRESST-III phase-1 experiment. Each module consists of a phonon and a light detector as can be seen in fig. 4.2. Source: CRESST collaboration.

## 4.1 CRESST detector concept

CRESST aims to detect WIMPs via elastic scattering off nuclei in scintillating crystals. The energy deposited by a particle interaction in the scintillating $CaWO_4$ crystal is read out by a TES sensor. The scintillation light is then collected by the light detector and also read using a TES. Measuring independently these two signals allows an event-by-event background discrimination.

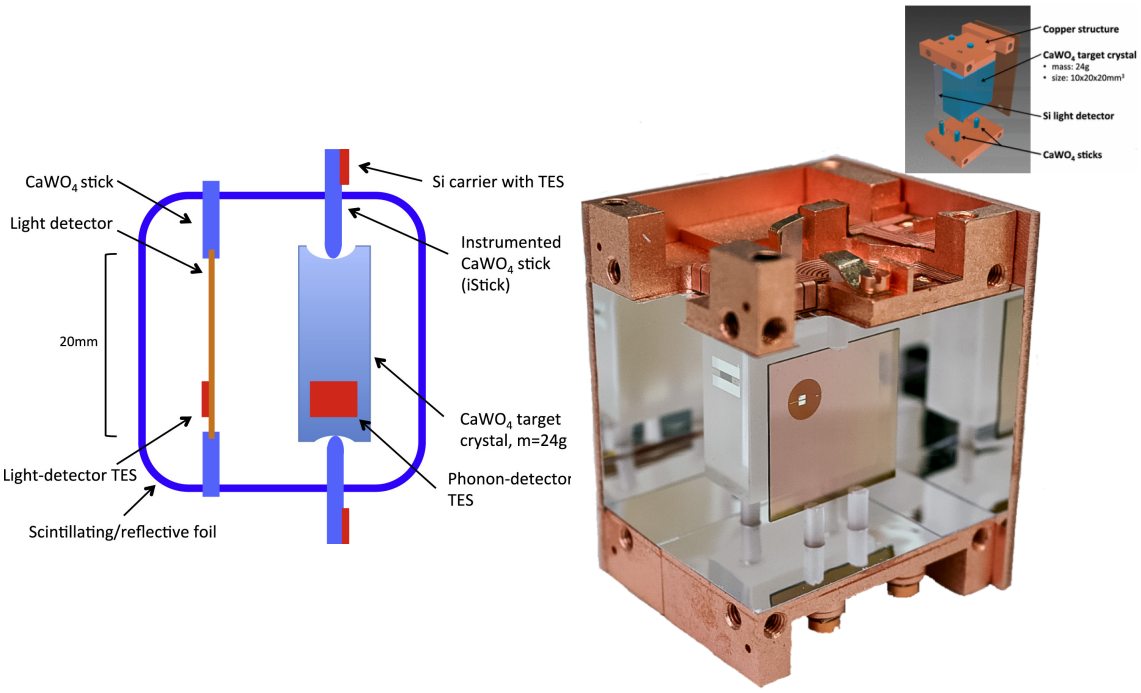


Figure 4.2: On the left: Schematic view of the CRESST-III detector module. Source: [53]. On the right: Picture of one the modules. On the top-right of the image, the different components of the module are indicated. Source: CRESST collaboration.

The detectors in CRESST are separated into several modules all operated at cryogenic temperatures (see figs. 4.1 and 4.2). In order to reach the operating temperature of the TES (20-25 mK), the detectors are installed in a dilution refrigerator with a base temperature of typically 10 mK. Working at cryogenic temperatures is crucial for detecting the very small energy deposited in the absorbers by the recoil of a WIMP because most of the energy deposited by this kind of particle is transformed into heat. Hence, the use of very low temperatures allows a unique sensitivity. The detector modules consists of two independent calorimeters, a $CaWO_4$ crystal and a silicon-on-sapphire-wafer acting as the light detector. A short description of the detectors and the read-out system is given below:

1. **Phonon detector**

   CRESST-III is using 24 g $CaWO_4$ crystals as the absorber-detector ($20\times20\times10$ $mm^3$). Each calorimeter is equipped with a temperature sensor which is directly evaporated onto the crystal and linked to the heat bath – the cryostat

(see fig. 4.2). When a particle deposits energy within the crystal, the rise in temperature ($\delta T$) is approximately related to the energy deposited ($\delta E$) and to the heat capacity ($C$) as follow:

$$\delta T \simeq \frac{\delta E}{C} \tag{4.1}$$

For a more detailed description of this relation see [55]. For cryogenic temperatures the heat capacity of semiconductors scales with the temperature as $C \propto T^3$ [56]. This cubic dependence with the temperature is the reason of the unique sensitivity of cryogenic experiments. The thermal link to the heat bath reestablishes the temperature in the detector after the particle interaction.

$CaWO_4$ crystals are multi-elements targets, a particularly convenient characteristic since it is in principle possible to distinguish from the recoils off the three different target nuclei (O, Ca and W) [23]. This translates in a wide range of sensitivity for the mass of the WIMPs candidates. WIMPs are more likely to scatter off W (A = 184) than in Ca (A = 40) and O (A = 16) since the scattering cross-section is proportional to the atomic number as $\propto A^2$ [24]. Ca and O become relevant though when searching for low mass dark matter particles, the energy transferred on a lighter atom (Ca or O) will be higher and therefore more detectable.

Other advantage of using $CaWO_4$ as the target material are its scintillating properties at low temperatures and the absence of a noticeable degradation of the light yield for events near the crystal surface [22]. Besides, there are no radioactive isotopes of Ca and O. This is imperative for DM-experiments where the background and the radioactive contamination have to be reduced to their minimum [25, 26].

2. **Light detector**

   The photon detector is a $20\times20\times0.4$ mm$^3$ silicon-on-sapphire-wafer (SOS-wafer) also equipped with a thermal sensor. It is also mounted in the reflective and scintillating housing facing one of the large surfaces of the $CaWO_4$ crystal (see fig. 4.2). The reflecting and scintillating housing is made of a highly reflecting polymeric foil to achieve a high light collection efficiency ("3M-Vikuiti") [62]. A small amount of the deposited energy in the absorber is emitted as scintillation light. For CRESST-III, about 6% of the deposited energy is then transformed into light and 30% of this light is then detected by the photon detector [36]. The emission time of light from $CaWO_4$ is of the order of milliseconds at cryogenic temperatures [67].

3. **Transition Edge Thermometer (TES)**

   The temperature sensors developed for CRESST are superconducting phase transition thermometers consisting of thin tungsten films (W) evaporated onto

a surface of the absorbers. Using a resistive heater placed on the detector, the thermometers are stabilized in the transition from the normal conducting to the superconducting phase where a small temperature rise leads to a relatively large increase in resistance. This makes them extremely sensitive thermometers [35]. For more information about TESs see for example [27, 55].

The sensors are directly deposited on both the phonon and the light detectors. When an incoming particle deposits energy on the crystals, the temperature of the detector increases which leads to an increase of the TES temperature. In fig. 4.3 the working principle of the TES can be seen. The thin superconducting W is stabilized in its transition temperature from superconducting to conducting phase ($\sim$ 20 mK). The tiny increase in temperature caused by the deposited energy from the particle interaction, leads to a change in the tungsten resistance. This change is in turn read by a **SQUID** (Superconductive quantum interference device).

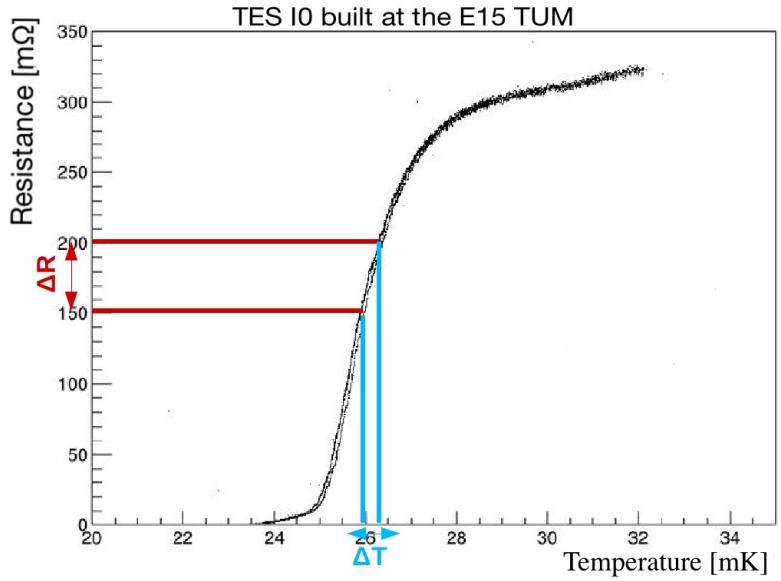


Figure 4.3: The TES is stabilized around its transition temperature, below the phase transition point. The tiny increase in temperature caused by the deposited energy from the particle interaction, leads to a relatively large change in the tungsten resistance. In this picture a very neat transition is visible; the steeper the slope, the more sensitive the sensor is. A wider transition or a multiple-steps transition, implies a loss of sensitivity. Source: E15 department, see appendix B.

4. **TES readout**

SQUID devices are very sensitive magnetometers, i.e., they can measure extremely low magnetic fields ($\sim 10^{-8}$ T). They are based on superconducting loops arranged with Josephson junctions. Their noise levels are also very low ($3\ \mathrm{fT}/\sqrt{\mathrm{Hz}}$) [29]. These characteristics allow them to detect tiny fluctuations

in the induced magnetic field produced by the change in the bias current after the phase transition of the TES [28].

The SQUID and a shunt resistor "$R_{shunt}$" (two in the case of the CRESST experiment) are connected in parallel to the TES (see fig. 4.4). They have a resistance of the order of few Ω. The circuit is biased by a current $I_{bias}$. This allows the SQUID to measure the change in the current produced by the change in the resistance. This change is then converted into a voltage (amplitude of the detected event-pulse) that is proportional to the change in current.

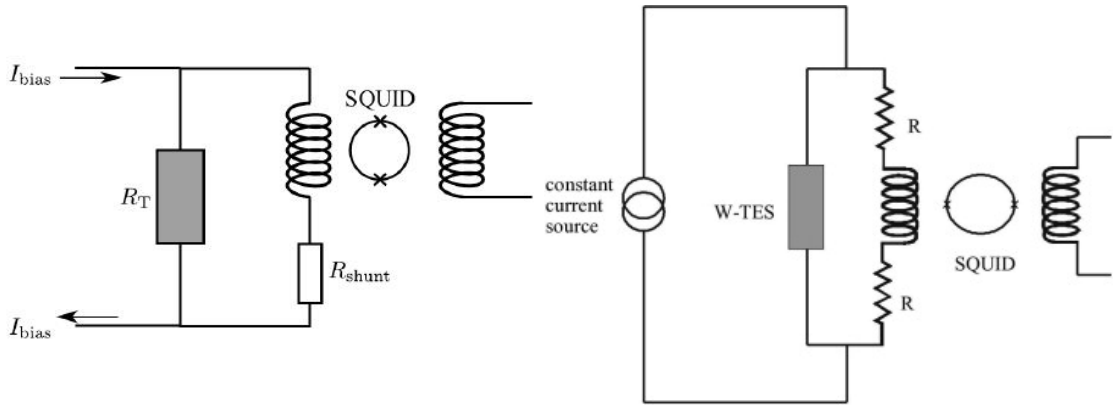


Figure 4.4: On the left: Scheme of the SQUID reading circuit. The shunt resistance ($R_{shunt}$) and the SQUID are in parallel with the TES ($R_T$). Small changes in the $R_T$ generate changes in the current that are detected by the $R_{shunt}$. These changes are read by the SQUID where tiny fluctuations in the induced magnetic flux are detectable. These flux fluctuations infer a current change in the secondary element (to the left) and this is then converted in pulses with different amplitudes measured in voltages. Source: [30]. On the right: Scheme of the SQUID system used for the CRESST experiment. Instead of one shunt resistance, there are two. Source: [54].

## 4.2 Background suppression and particle discrimination mechanism

One of the biggest difficulties in DM detection experiments is the fact that DM is expected to interact very rarely $\leq 0.1$ $kg^{-1}d^{-1}$ meanwhile a large density of highly energetic particles is bombarding the Earth constantly. Hence, a very good and efficient background suppression is essential.

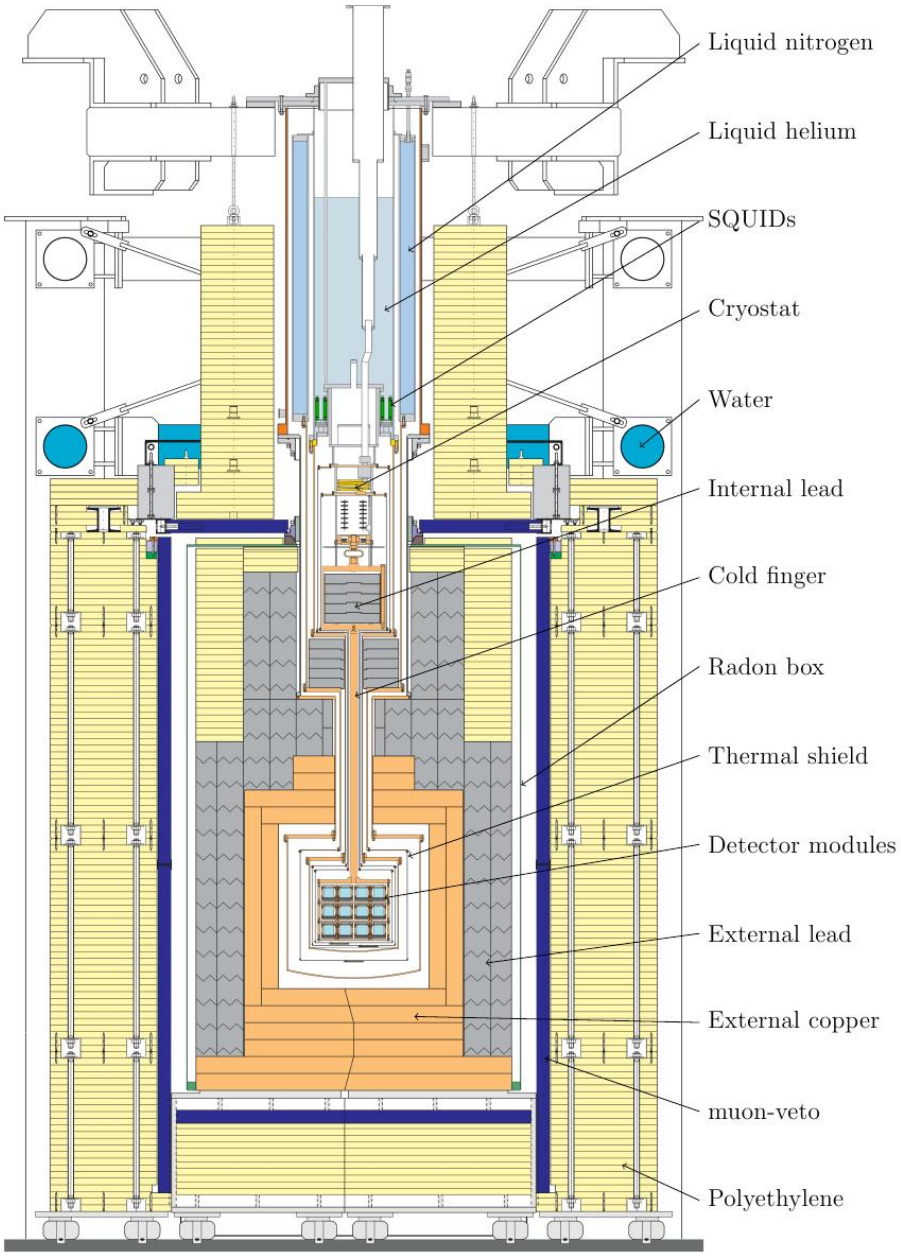


Figure 4.5: Scheme of the CRESST experiment inside. Source: [30].

In order to limit the flux of cosmic particles, direct dark matter experiments are placed deep underground. The LNGS is under 3500 meters of water equivalent rock overburden underneath the Gran Sasso massive. This reduces the muon flux to about 1 muon $m^{-2}h^{-1}$ [31]. The ambient radioactivity originating from the surroundings of the experiment is suppressed by multiple passive shielding layers. The detectors in CRESST are shielded by 14 cm of low radioactive copper and 20 cm of high radio-purity lead; these two layers reduce significantly the radiation in the vicinity of the detectors.

From CRESST-II on, 50 cm thick polyethylene neutron shield was installed around the cryostat together with a muon veto (see fig. 4.5). The inner shielding is entirely enclosed within a gas-tight radon box which is continuously flushed with $N_2$ gas. The muon veto consists of 20 plastic scintillator panels of area about $\sim$1 $m^2$ surrounding the radon box and the Cu/Pb shielding. The use of three different types of panels results in a total solid angle coverage of 98.7% [31]. Due to the very low event rate predicted for WIMP-nucleus elastic scattering, an additional background identification is required. Not only WIMPs, but also muons, electrons, photons and alpha particles will interact with the detector despite the shielding provided by these facilities. They come from natural radioactivity near the detector and from cosmic rays. Therefore, an additional discrimination technique is required.

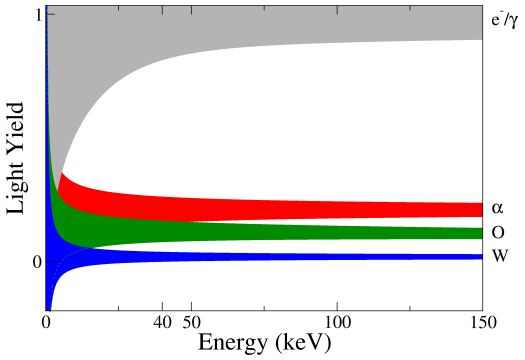


Figure 4.6: Light yield for different particles recoils at different energies. The nature of the target nucleus involved in the scattering (O in green and W in red) can be identified. Source: [35].

In the case of CRESST, this technique is called the phonon-light technique. CRESST exploits the fact that most common backgrounds produce some light in a scintillating material, while WIMPs are expected to induce nuclear recoils that produce little or no light. The dominant background comes from $e^-$ and $\gamma$ that are suppressed by the phonon-light mechanism. Consequently, by measuring the scintillation in addition to the phonon signal, most of the backgrounds can be removed.

The light detector permits a determination of the **Light Yield** for an event, allowing an effective separation of nuclear recoils from electron–photon backgrounds. The light yield, defined as the energy deposited by a particle recoil in the light detector divided by the energy deposited by the particle interaction in the phonon detector ($LY = E_{light}/E_{particle}$), varies for every event. This process is denominated **quenching** and allows this event-by-event discrimination (see fig. 4.6). The factor that quantifies the quenching of every event is denominated **Quenching Factor** [67]. The amount of scintillation light also depends on the mass of the recoiling nucleus. Thus, measuring the light yield allows to identify also the nature of the target nucleus involved in the scattering (W, Ca or O).

# Chapter 5

# Neganov-Trofimov-Luke Effect (NTLE)

This effect was discovered in 1985 by B. Neganov, V. Trofinov [57] and experimentally studied by P. N. Luke in 1988 [58] and is based on the amplification of a heat signal in a semiconductor absorber (silicon, germanium, etc.) operated at cryogenic temperatures ($\sim$ mK).

In this chapter, an overview of the utility of this effect in astroparticle experiments will be provided, together with a detailed explanation of the characteristics of this effect. It will be explained and demonstrated how the NTLE improves the measurement of the energy deposited by photons in a calorimeter increasing, in turn, the signal-to-noise ratio.

## 5.1 Aims: Lower the threshold and improve the resolution

Low energy threshold detectors operated at cryogenic temperatures for the search of dark matter particles and the study of low-energy neutrino scattering, were already studied in the 1980s [32]. They present a very powerful way to measure low energy ionization events ($\leq$1 keV), or equivalently, to measure low energy deposition, with a good energy resolution.

Making use of these advantages, cryogenic DM search experiments are currently focusing their search to the low mass region ($\sim$ keV). The nuclear recoils produced by DM events, are generally expected in the region below 40 keV in the phonon detectors. The energy spectrum of WIMPs increases exponentially when going to lower energies. For CRESST, the goal is to achieve the best resolution possible in the region just above its energy threshold (50 eV) [53]. It is also desirable for the light detector to have a very good discrimination down to the threshold with the future goal of achieving a sensitivity that reaches the coherent neutrino scattering

floor [37]. In the case of neutrinoless double beta decay ($0\nu\beta\beta$) experiments, the current generation is expected to reach a sensitivity on the half-life of $\sim 10^{25}$ years, and the future one aims for $10^{26}$-$10^{27}$ years [61].

The energy region of interest for both kinds of experiments differs significantly: from ∼100 keV for nuclear recoils in DM search experiments to electrons with energies up to MeV typical of $0\nu\beta\beta$ experiments. However, there is a common need for both cases of an improvement in the detector performance – achieving higher target masses without compromising the excellent resolution provided by terrestrial target experiments. Nevertheless, building large detectors with the resolution obtained in the terrestrial rare events search experiments, implies the assembly of multiple detectors together. This translates to multiple read-out channels that might increment the noise and contaminate these high purity ensembles due to the electronics.

Following section 4.2, thinner electronic recoil band leads to a better background discrimination. The particle discrimination increases when the resolution of the light detector improves. This idea prompts the study and possible implementation of the NTLE in the light detectors. The NTLE enhances the heat collection in the light detectors enhancing, in turns, the sensitivity of the calorimeters, which might help to enlarge the light detectors without compromising resolution and without the addition of multiple read-out channels.

Also, very low energy threshold can be achieved using the NTLE (see section 7.4.3 and section 7.4). Its study might provide a huge advantage in the optimisation of light detectors at cryogenic temperatures, which is the major motivation and goal in this work.

### 5.1.1 State of the art of cryogenic light detector calorimeters

Calorimeters are used in rare event search experiments that require very high sensitivity, such as DM direct detection, rare nuclear decays and $0\nu\beta\beta$ experiments. The electronics of normal solid state detectors do not work at very low temperatures meanwhile calorimeters can combine high quantum efficiency (QE) and high resolution at cryogenic temperatures. Calorimeters are based on an energy absorber linked to a temperature sensor. The signal is collected at cryogenic temperatures and consists of a thermal pulse read by the sensor. Therefore, they are the most effective solution to detect the few photons emitted by a larger mass crystal also operated at mK.

Cryogenic detectors also provide high sensitivity in a large energy range due to the temperature sensor; from just a few eV, to nuclear recoils in the range of 100 eV in DM search experiments and electrons with energies up to MeV typical of $0\nu\beta\beta$ experiments.

Germanium and silicon are the most common materials used as the energy absorber for light detectors in these experiments. These detectors can achieve very low thresholds and have excellent performances. The semiconductor industry is mainly focused on Si, even Ge is also commercial. As for the SOS, its use is restrained to scientific purposes.

The best energy resolution obtained for light detectors with a considerable size is 12 eV ($1\sigma = 5$ eV). This resolution was achieved with the CRESST light detectors [52]. CRESST is currently working on the reliability of its light detectors and on achieving single photon detectors – improve this value by a factor 4.

Remarkable developments have also been reported in the context of AMoRE and LUMINEU [47, 48, 49] by using photon detectors based on metallic magnetic calorimeters (MMCs). These detectors have rise times in the order of $\mu$sec with an energy resolution of 200 eV. Fast detectors like these are especially important for $0\nu\beta\beta$ experiments where two consecutive electron events can be regarded as a single event due to the short time lapse between the two events in comparison with the signal rise time. In the low activity environment found in the underground facilities the energy resolution does not suffer from the slow signal, but it is still desirable developing fast detectors to avoid random coincidence of events caused by slow detectors.

### 5.1.2 The NTLE in astro-particle physics detectors

Both SuperCDMS [34] and EDELWEISS [40] experiments have for years studied the use of the NTLE-based detectors. These experiments employ phonon and ionization channels to discriminate the particle interactions and therefore, they do not conduct studies of the NTLE on photon detectors. The implementation of NTLE-detectors for these experiments is currently under investigation [50, 51].

An experiment exploiting the NTLE in light detectors is LUMINEU [46]. Like in CRESST, it employs photon and phonon channels to make the particle discrimination. Its light detectors are made of Ge. To apply the $V_{NTL}$ aluminum concentric rings are evaporated onto the surface. No results on the energy resolution of these detectors have been recently reported.

At the TUM, NTLE-photon detectors have been consistently studied in the last decade in the context of the CRESST experiment [64, 66, 67]. NTLE-photon detectors consisting of $20\times20\times0.5$ mm$^3$ 24 g $TeO_2$ with a resolution of $1\sigma = 7.8$ eV have been reported from [59, 60]. Important results regarding the mitigation of the degradation of the signal with time by annealing the detectors in forming-gas mixture (95% $N_2$, 5% $H_2$) have been recently reported in [62]. These results correspond to $20\times20\times0.5$ mm$^3$ Si substrates with deposited aluminum strips onto the surface. The latest results achieved using an alternative geometry (section 5.1.3)

will be presented later in chapter 6 and can also be found in [63].

### 5.1.3 A novel geometry for NTLE

The E15 research group is currently studying simultaneously two different electrode configurations for NTLE-amplified cryogenic light detectors.

- The lateral field configuration: this configuration (see fig. 5.1) has been under study since 2005 [64]. It consists of a Si absorber crystal with two or more thin aluminium strips deposited onto one of the surfaces. These strips are used as the electrodes needed to apply the $V_{NTL}$ across the surface. In this way, the created electric field is parallel to the semiconductor's surface. This configuration had presented a degrading signal-amplitude with time due to the trapping of charge carriers around the electrodes [64, 65, 66]. This problem was improved by annealing of the absorbers in forming gas [62, 67]. Nevertheless, it has not been achieved yet the expected gain predicted in theory due to a non-complete charge collection. The development of this **lateral configuration** is currently ongoing.

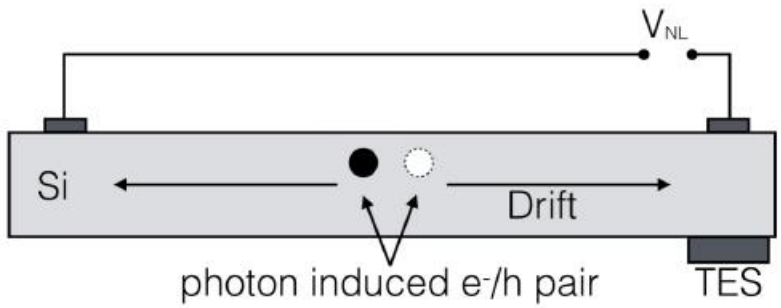


Figure 5.1: Scheme of a lateral field configuration NTLE-light detector.

- The vertical field configuration: the investigation of this configuration started in 2014 and is denominated **planar configuration** (more details in section 6.3.2). This thesis is focused on the study of this novel configuration and next chapters are dedicated to its description. Nonetheless, in few words the main difference relies on the electric field applied along the crystal bulk and perpendicular to the absorber's surfaces (see fig. 5.2). The electrodes are implanted contacts covering both surfaces. This characteristic presents two major advantages: no possible trapping on the free surfaces and a bigger electric field applied with very low leak currents.

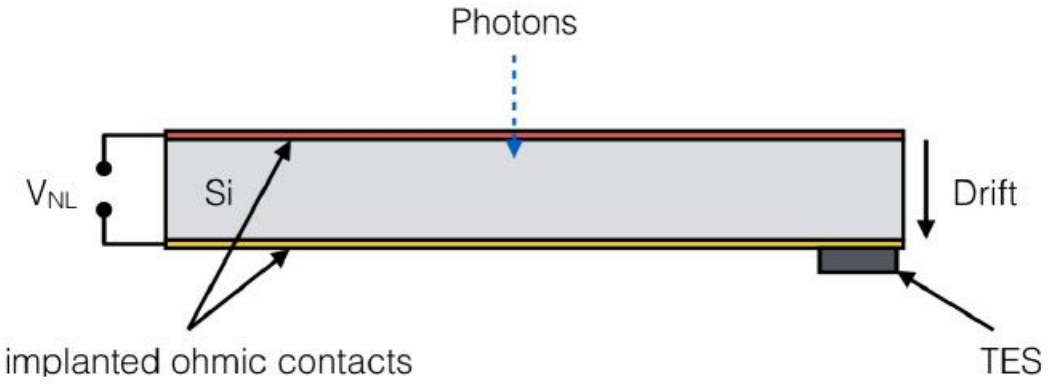


Figure 5.2: Scheme of a vertical field configuration NTLE-light detector.

## 5.2 Description of the NTLE

As described in section 4.2, the photons emitted from the scintillation of the $CaWO_4$ crystal are detected using a calorimeter equipped with a TES. When a photon deposits energy within the absorber, the temperature of the absorber rises. The principle of the NTLE is as follows: when photons interact within a semiconductor, electron-hole pairs (e-h pairs) are created. These e-h pairs can be drifted within an applied electric field resulting in an additional phonon signal, similar to the Joule effect. This effect is called Neganov-Trofimov-Luke-Effect (NTLE). Meanwhile the Joule effect originates from the heat of free charge-carriers going through the lattice, the NTLE is only induced by photo-generated carriers. The advantage of such a method is that the thermal signal of the light detector increases with the voltage applied, while the noise typically remains constant. This provides an increase in the signal-to-noise ratio. The sensor used to detect the rise in temperature can also be a TES (item 3).

It can seen in fig. 5.3, the displays pulses of a 16 keV energy deposition on a detector with no NTLE voltage applied on the left and 97 V on the right. At 0 V, the amplitude of the pulse is much smaller than the one on the right. Since the noise remains the same, one can notice that the signal-to-noise ratio improves significantly while applying the voltage. Hence, the sensitivity of the detector is also improved.

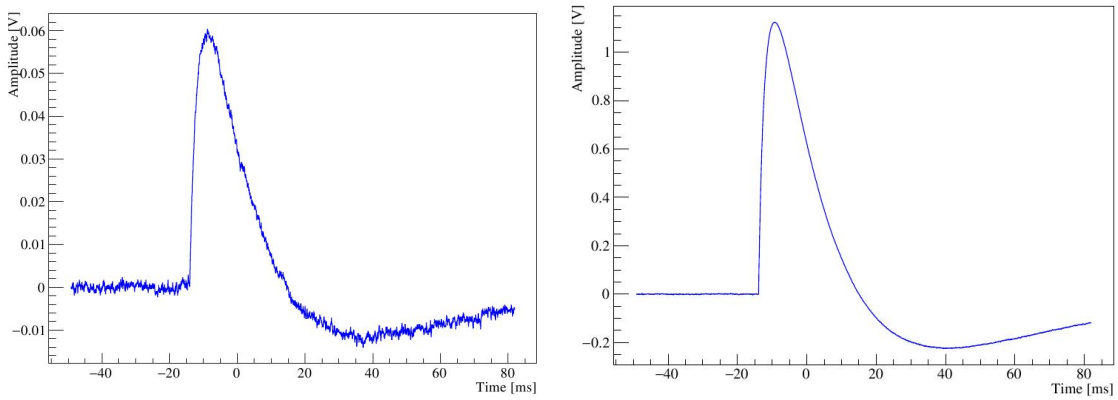


Figure 5.3: On the left: signal read-out on the TES when 0 V is applied on the NTLE detector for a 16 keV photon pulse deposited. On the right: signal read-out on the TES when 97 V is applied on the NTLE detector for the same energy deposited within the detector. The improvement of the signal to noise is striking.

### 5.2.1 Phonon Gain

The electric field needed to produce the NTLE is generated by applying a voltage across the absorber, this voltage is what from now on will be called the NTL-voltage designated by $V_{NTL}$. The electric field allows the e-h pairs created (electrons and holes in opposite directions) to drift across the absorber until they reach the electrodes. In addition to the initial heat deposition, there is a heat associated to the drift of the photo-generated carriers within this electric field.

The amount of e-h pairs created is given by $N = E/\epsilon$, where E is the energy deposited by the incoming radiation and $\epsilon$ is the the average energy needed to create an e-h pair.

Denoting the initial energy deposited on the the detector as $E_0$, the additional energy transferred to the phonon system once the $V_{NTL}$ is applied is as follows:

$$E_T = E_0\left(1 + \frac{e \cdot V_{NTL}}{\varepsilon_{e-h}}\right) \tag{5.1}$$

With $\varepsilon_{e-h}$ the average energy for creating an e-h pair in the material and for a specific light source, and $e$ the charge of the electron. Using this equation, the theoretical thermal gain is immediately deduced:

$$G = \frac{E_T}{E_0} = \left(1 + \frac{e \cdot V_{NTL}}{\varepsilon_{e-h}}\right) \tag{5.2}$$

### 5.2.2 Poisson Fluctuations

The desired ultimate signal to detect is a single photon. The detector is radiated with a flash of photons and this limits the amount of photons that can be detected. This

means that for two events with the same energy deposited in the $CaWO_4$ crystal, the number of photons detected can fluctuate following the Poisson statistics. The energy resolution can be described as follows:

$$\sigma_E = \frac{E}{\sqrt{N}} \tag{5.3}$$

Where E is the energy deposited in the photon detector and N is the number of photons detected. The number of photons detected is fairly low since at most 6% of the energy deposited in the $CaWO_4$ crystal can be detected by the light detector in the CRESST experiment (considering 100% detection efficiency).

The evaluation of the energy deposited within the $CaWO_4$ absorber using only the light signal is thus more subject to fluctuations than to the signal directly read on the $CaWO_4$ crystal. But despite these fluctuations, which are intrinsic to the light signal, the experiment can benefit from having a light detector with an excellent energy resolution. The reason for this is that it would be ideal to identify the background down to the lowest energies and for this it is necessary to measure a signal down to a single photon detection (the resolution required for this needs to be better than $\sim$3 eV).

When a photon interacts within the silicon, one electron-hole pair is created every time for the case of 430 nm photons [73]. So for a photon signal, no additional fluctuations are induced other than the fluctuation of phonon measurement.

This is not the case for an X-ray, in which case the number of e-h pairs created also fluctuates and is the dominant fluctuation at high energies. In the next chapter it will be shown that using an X-ray source can be very useful to calibrate the detectors. The contribution to the fluctuations induced by the creation of e-h pairs for the interaction of an X-ray is :

$$\sigma_E = \sqrt{E \cdot F \cdot \epsilon} \tag{5.4}$$

With F being the Fano factor for X-rays in Si with a value of $\sim 0.1$ (F for 430 nm photons in Si is $\sim 1$) and $\epsilon$ the average energy needed for an X-ray to create an e-h pair.

### 5.2.3 Energy Resolution

As was seen in the previous section, the energy resolution is limited by Poisson fluctuations, especially at high energies where the number of photons or e-h pairs generated is greater. For 430 nm photons no additional fluctuations are induced by the creation of e-h pairs, and that by being able to detect single photons the optimal energy resolution would be obtained. It was also seen that this is not the case for X-rays, where the fluctuations come from the number of e-h pairs created. By looking at equation 5.4 and considering the previously presented relation for the

amount of e-h pairs created, N = E/$\epsilon$, the following relation for the energy resolution for X-rays is reached:

$$\Delta E = \sqrt{E\epsilon F} = \epsilon\sqrt{NF} \propto \sqrt{N} \tag{5.5}$$

The nature of these fluctuations comes from the fact that the energy deposited in the absorber after a particle interaction, is divided in creating both e-h pairs and optical phonons. The optical phonons quickly decay into acoustic phonons and thermalize providing the heat signal observed for 0 V applied.

For the X-rays interacting in Si, the ratio of e-h pairs created and phonons is $\sim 1/3$. The $\epsilon_{\mathrm{X-rays}}$ is in this case 3.8 eV (at 77 K [72]) and the gap of the Si-diode is 1.17 eV (the minimum required energy to create an e-h pair). Dividing $1.17/3.64 \approx 1/3$. For the 430 nm photons the energy dedicated to create e-h pairs compounds 2/5 (1.17/2.88). In this second case, $\epsilon_{\mathrm{photons}}$ is calculated as $\epsilon_{\mathrm{photons}} = \mathrm{E}_\gamma/\eta$, being $\eta$ the internal quantum efficiency for 430 nm photons in Si and close to 1 in this case [73].

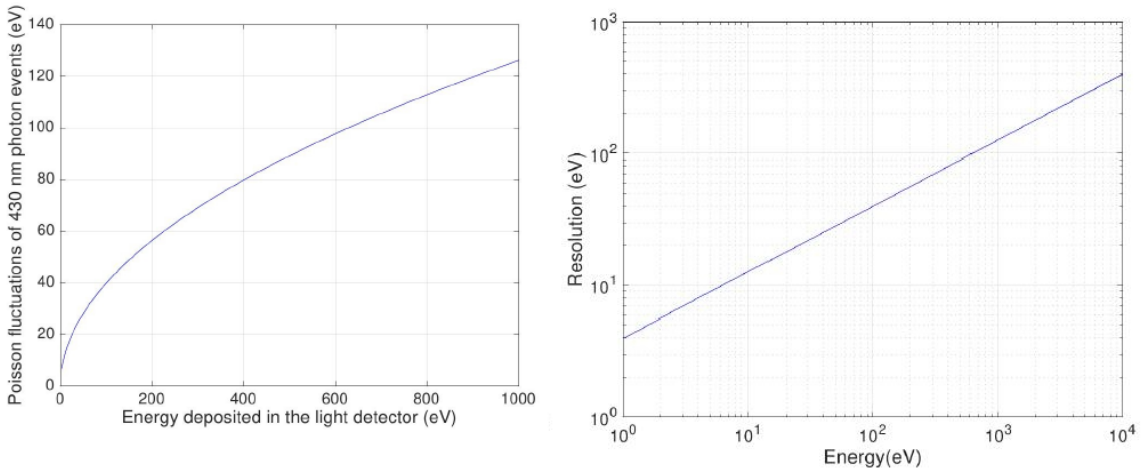


Figure 5.4: On the left: Quadratic evolution of the energy resolution depending on their energy according to eq. (5.5). The fluctuations in the energy resolution for a photon signal and its quadratic behaviour following the Poissonian fluctuation description can be seen. On the right: Evolution of the energy resolution in a logarithmic scale.

The Poisson fluctuations becomes the dominant influence in the energy resolution (the noise is typically independent of the voltage applied). It can be seen in fig. 5.4 that the energy resolution increases quadratically with the energy for 430 nm photons, i.e., with the number of photons detected. At higher energies, the Poisson fluctuations of the signal is also the main contribution to the broadening of the total resolution. This is true for a deposition of energy with photons but also for

X-rays -the number of e-h pairs created is limited. To make these plots, the noise contribution to the resolution has not been taken into account for being typically independent of the energy -offset value.

### 5.2.4 Noise contribution to the Energy Resolution

Apart from the intrinsic statistical fluctuations of the signal, there are noise contributions that are needed to consider as a contribution to the broadening of the energy resolution.

Some known sources are presented in the following:

- The thermodynamic noise that limits the ultimate resolution. At a certain temperature T, this is related with the capacitance C of the device as:

$$\Delta E = \sqrt{T^2 k_B C} \tag{5.6}$$

  Where $k_B$ is the Boltzmann's constant. It is needed to multiply to this expression a dimensionless factor which value depends on the responsibility of the sensor. In addition, the materials being worked with obey the Debye law at low temperatures, therefore $C \propto MT^3$, where M is the mass of the detector. Therefore, $\Delta E \propto \sqrt{T^5 M}$ which for cryogenic temperatures turns in an excellent resolution [58]. When the $V_{NTL}$ increases, this contribution is not dominating, i.e., beyond the thermodynamic fluctuation limit where the heat signal is dominated by the charge creation. However, it needs to be consider at low $V_{NTL}$ and for not voltage applied.

- The thermal fluctuations in the thermal link that joins the sensor and the cryostat. At the temperature of the transition, these thermal fluctuations contribute creating changes in the overall resistor power. This noise is thus function of both the temperature and the thermal conductance of the thermal link.

- The Johnson noise associated with the shunt resistor $R_{shunt}$. This noise accounts for the thermal fluctuations of any resistor at a given temperature.

- Another contribution comes from the input photon noise. The flux of infrared photons on the detector can add a significant power with fluctuations degrading the detector resolution. For example, the flux of photons coming from the optical fibre connected to the 300 K stage, can emit a significant amount of black-body radiation. Photons below 1.1 eV cannot create e-h pairs but can still contribute to the baseline noise.

- The SQUID amplifier circuit has, of course, an intrinsic noise.

- A specific noise contribution to the NTLE-detectors has been observed; this noise increases when increasing the $V_{NTL}$ and could be due to the un-trapping of charges when the external field increases [67]. This contribution will be further studied in this thesis in section 7.4.2.

These noise contributions have different origins: the normal noise from the power supply which contributes with the known 50 Hz, the noise from the electronics (which is referred to as the SQUID's noise), the Johnson noise coming from the TES, the noise from the LED's cables, microphonics, etc. However, as will be seen in section 6.5, the total experimental noise contribution to the energy resolution can be calculated.

Being able to identify all contributions to the noise is of major importance – knowing their origin may help to reduce their effect as much as possible.

# Chapter 6

# Experimental Techniques

In this chapter the experimental set-up used for the experiments will be described. For all the measurements a detector module consisting of a PIN-diode and two sources (radioactive source and optical light) were mounted inside a dilution refrigerator (see appendix C for more details on the working principle of a dilution refrigerator). For most of the experiments the cryostat located in the shallow Underground Laboratory ($\sim$ 15 m.w.e.) at the physics department of the Technical University of Munich, Germany was used. Moreover, some additional experiments were also performed at the Centre de Sciences Nucléaires et de Sciences de la Matière (CSNSM) in Orsay, France. To see more technical details and characteristics of every particular experiment see the appendix A.

## 6.1 Setup

A schematic drawing of the experimental set-up is shown in fig. 6.1. Each detector was mounted inside a copper housing (see fig. 6.2 and fig. 6.3) and held by either ceramic or Sintimid plastic clamps. The sensor (a TES or a NTD) is glued with epoxy-glue on the back surface of the diode, i.e., the dark side of the photodiode. The sensor is usually placed in the middle of the surface to limit any position dependence. Aluminum wires bonds are used to connect the diode with the cooper bond pads of the holder where the $V_{NTL}$ is applied. There is a blade on each side of the holder so the $V_{NTL}$ can be applied across the bulk. A gold wire is bonded from the copper holder to a gold strip on the TES to establish a thermal link.

Additionally, a heater and a resistive thermometer are installed on the holder to have a more precise temperature control on the diode. The holder is directly mounted in the cryostat. A copper thermal link is installed between the detector and the cryostat.

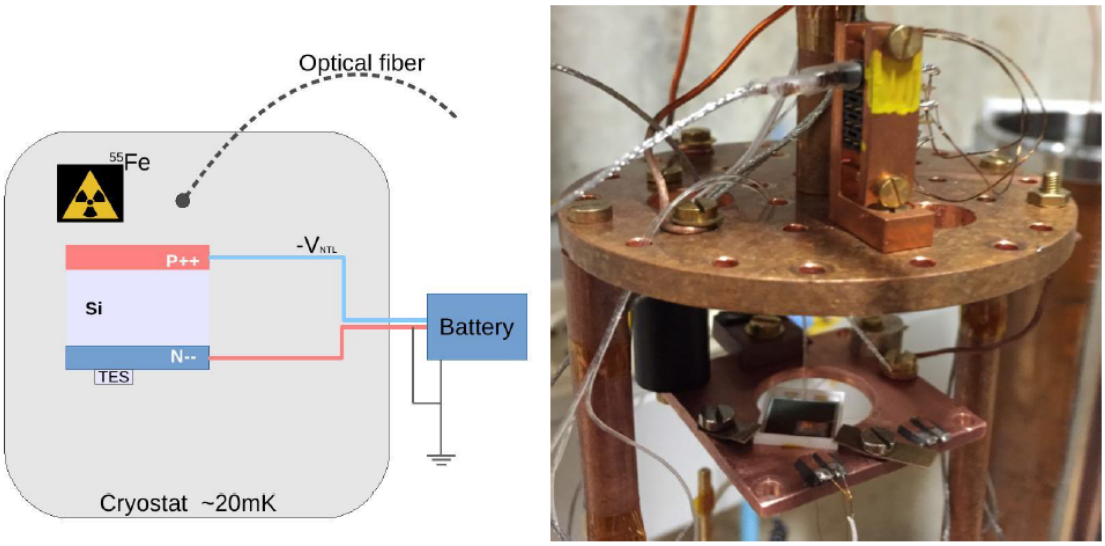


Figure 6.1: On the left: scheme that shows the experiment from inside the cryostat with the main basic elements of the experiment. On the right: Picture of one of the experiments. The copper plate where the detectors are mounted can also be seen. In the same plate where the detector is mounted, there are the thermometer (black cylinder on the left back corner of the detector holder) and the heater (back right corner of the holder). Both the heater and the thermometer allow for better control of the temperature of the diode. On the top place there is the radioactive source (element with the yellow mark on it) and the optical fiber to radiate the detector.

To apply the $V_{NTL}$, a battery was used in order to limit the extra noise introduced in the system by ground loops and pick-ups from the mains. This made it possible to deliver voltages as high as 300V.

The tungsten TESs used were produced in-house at E15. For details of the particular TES used in each of the experiments, i.e., their transition curves, check the appendix B. A schematic picture of the holder with the detector and sensor with connections is shown below in fig. 6.2. The possibility of gluing the TES with epoxy is very important since the fabrication of the photo diode and of the TES can be completely independent. The TES can therefore be selected before installing it on the photodiode.

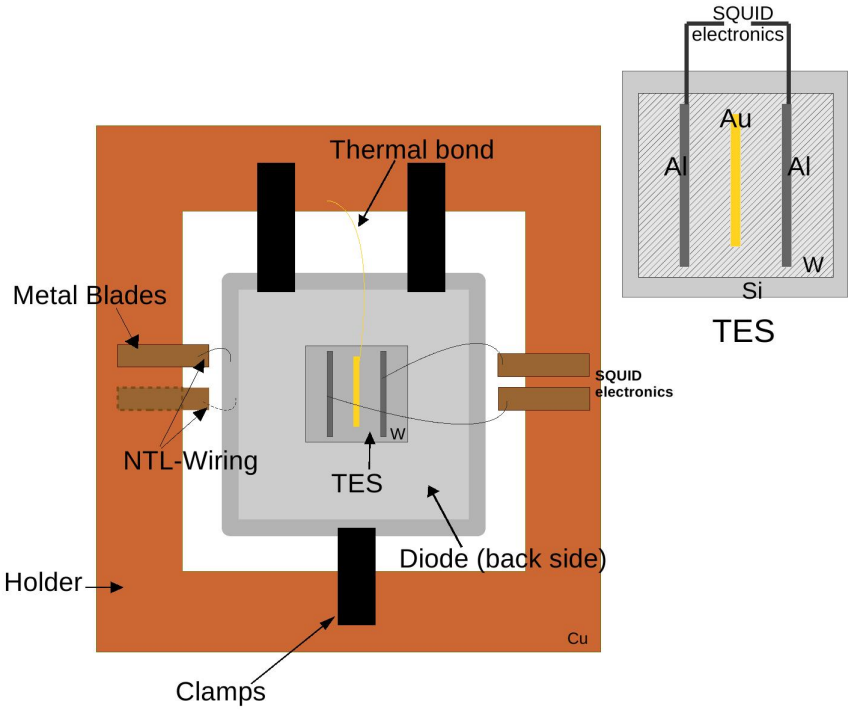


Figure 6.2: Scheme of detector in its copper holder (seen from the TES side). On the top right is a detail of the TES.

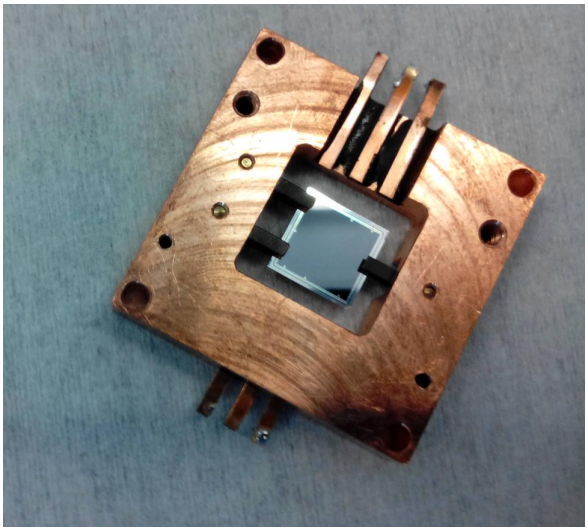

Figure 6.3: This picture depicts one of the diodes. The surface shown is the photo-sensitive. The Sintimid-plastic clamps holding the diode in a copper holder are also visible. On the sides of the holder, there are the copper band pads where all the connections are made.

## 6.2 Choice of the Sensor

In chapter 4, the TES sensor used in the CRESST experiment was described. However, for the experiments here both TESs as well as Neutron Transmutation Doped (NTD) sensors were used. In the following the advantages and disadvantages of using one or the other type of sensor will be presented.

### Neutron Transmutation Doped (NTD)

NTD sensors are made from a high purity semiconductor (usually Si or Ge) that has been irradiated by a thermal neutron flux. For a Si NTD, the thermal neutrons are captured by a $^{30}$Si isotope, which has a 3% abundance in pure Si. Due to the high neutron/proton ratio of $^{31}$Si, this unstable isotope will decay emitting a $\beta^-$ and converting a neutron to a proton, the $^{31}$Si atom transmutes to a $^{31}$P atom and the semiconductor becomes a n-doped semiconductor (five electrons in their outermost shell).

NTDs exhibit a predictable temperature dependence of the resistivity down to a few mK after a Coulomb interaction ($\rho \propto T^{-1/2}$ in the absence of magnetic fields). This is the reason NTD-thermistors can also be used as a low temperature thermometer [76].

These sensors can be used for a larger temperature range in comparison to the TES (which used is limited to the transition temperature of the sensor). Consequently, this facilitates the experimental performance.

Besides, NTDs do not need of additional expensive elements, such an SQUID and its reading electronics, to measure the changes in resistance because it uses conventional voltage amplifiers. This implies a considerable reduction in the experimental costs.

The NTDs available for these experiments were Ge-NTDs. This condition is not optimal, since the detectors were made of Si and the change in the semiconductor material from the detector to the sensor creates mismatched phonon properties.

### Transition Edge Sensor (TES)

A TES can have a very high count rate if biased with an electro-thermal feedback [77]. They are also much more sensitive to changes in temperature, especially in the range of mK, which make them more appropriate for the requirements here than the NTDs. On the other hand, they are heavily affected by weak magnetic fields [78].

The biggest disadvantage for using TESs is the high price of their electronics (SQUID, read-out channels, etc.) in comparison to the NTDs. Nonetheless, for most of the

experiments TESs were used as the sensors since the primary aim is having a good sensitivity.

## 6.3 Choice of the Semiconductor Absorber

The typical materials used for the semiconductor absorber are germanium and silicon. Germanium has the advantage of being highly pure, having an impurity concentration only in one part of $10^{10}$ (being the one for pure silicon of one part of $10^9$). This characteristic reduces the possibility of encountering defects or traps that can retain free charges on their way to the electrodes. In real detectors, the thermal gain is usually reduced by space charges that create a counter electric field with time. The result is a reduced effective voltage and a degrading signal ([64, 65, 66]).

However, germanium is not easily found in nature and because of this, its price is much higher than silicon's, which is widely encountered in nature and in industry and thus much cheaper.

But the main reason to choose silicon over germanium relies on the fact that silicon naturally grows a stable oxide on its surface, a thin layer of $SiO_2$. Silicon oxide is a very good insulator, which is ideal when forming junctions because prevents the diffusion of the dopants into the absorber acting as a blocking layer. The properties of the silicon oxide are very useful to prevent leak currents occurring on the surface. One of the main limitation of Ge-NTLE-detectors is due to surface leak currents since germanium does not have a natural oxide.

Moreover, the penetration depth of optical photons is higher in silicon than in germanium which decreases the sensitivity to surface trapping effects.

When an X-ray interacts within the absorber the average energy ($\epsilon$) to create an e-h pair in silicon is higher than in germanium. This limits the resolution because of the reduced amount of pairs created ($\sim$ 3.6 eV compared to $\sim$ 3 eV). But the detection of 430-nm-photons is desired – the average energy to create an e-h pair is the energy of the photon itself (see section 5.2.1).

The heat capacity of germanium is also about four times bigger than the one in silicon. As was seen in eq. (5.2), the amount of heat released in a totally efficient NTLE-process, is equivalent to $Q\Delta V$, being $\Delta V$ the external voltage applied. For what the temperature change induced is given by $\Delta T \propto Q\Delta V/C$ according to eq. (4.1), with C the absorber's heat capacity. Thus, this change in temperature will be greater for a smaller heat capacity. The smaller the heat capacity the better the ultimate energy resolution is (section 5.2.4).

Silicon is also present in processing technologies which facilitates the consequent implementation of thermal sensors. To summarize, Si-characteristics and its strong

presence in technology industries enable Si-detectors implemented with NTLE to have the potential to be produced in a reproducible way and be adapted relatively easily to specific demands. For an extension on the choice of semiconductor absorbers see appendix D.

### 6.3.1 The use of PIN-diodes

A standard NTL-detector (like the one in fig. 5.1) can present *large* free surfaces where charges can get trapped. The trapping is an issue since it induces degradation: the collection of the charges evolves in time and therefore the signals too ([64, 65, 66, 67]). By applying the electric field perpendicular to those surfaces and placing the electrodes over the surfaces, the charge trapping can be reduced tremendously. Also, considering the thickness of the detector and the depletion of the diode, the electric field applied can be very high [63].

Semiconductor's PIN-diodes when operated as light detectors are some of the most sensitive detectors. Their operation relies on the creation of carriers, in this case e-h pairs, by absorbed radiations. Thus, their own operation system make them suitable candidates to study the NTLE.

Knowing the advantages that Si presents over Ge for the purposes here (section 6.3), Si PIN-diodes were chosen for this work [63]. The PIN-diode structure is made out of a high purity silicon wafer heavily doped, as will be seen in the next section. Various industrially-produced diodes were used to perform the experiments.

### 6.3.2 Diode specifications

The NTLE detectors used for this work were PIN diodes. Several commercially available diodes that fitted the requirements for these experiments were tested. Some of the most important requirements included silicon photodiodes with high purity silicon absorbers, specified sizes and ohmic contacts on the surfaces. All he PIN-diodes used have two thin highly doped surfaces serving as the electrodes of the detector. The contact of the doped layers is made with thin aluminum layers ($\sim$ 100 nm) on both surfaces (see fig. 6.4). The influence of the Al has been studied and will be discussed later (section 7.7).

The P-doped surface consists of boron and constitutes the entrance window for the radiation. The thickness is lower than 50 nm to allow a large fraction of the photons to be absorbed within the active volume of the diode. The intrinsic part between the two electrodes consists of high-purity Si. The N-doped surface consists of phosphorous and is $\sim$200 nm thick. The total thickness of the detector is 300 $\mu$m for the 10x10 mm$^2$ diodes, and 500 $\mu$m for the larger diodes (see table A.1 in appendix A). Because the high purity of the Si, the passivation due to the $SiO_2$ and the small barrier of the Si, these diodes can withdstand huge electric fields –

typically 100 V/300 $\mu$m which corresponds to 3000 V/cm [63].

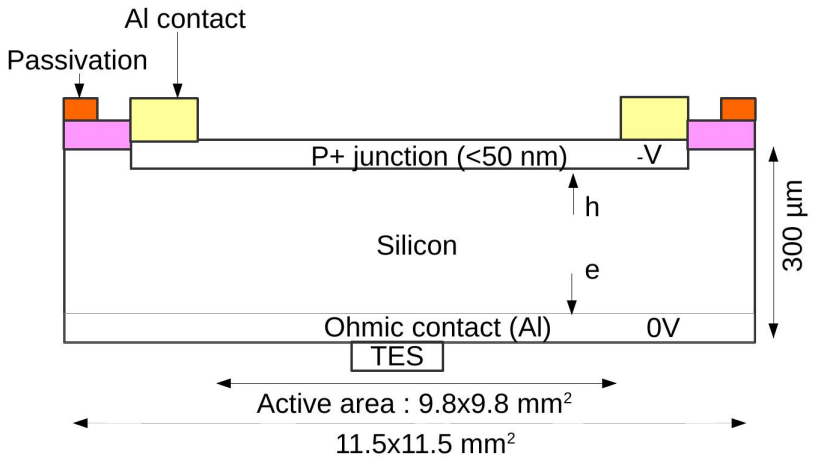


Figure 6.4: Scheme of a planar configuration NTLE PIN-diode detector as the ones that were used in these experiments. It can be seen the size of the different regions and a representation of the most important elements, i.e., the Al-contacts, the passivation, the position of the TES, etc. Source: [63].

### 6.3.3 Energy level diagram

It is also convenient and interesting for the understanding of the results presented in this work to study the NTLE from a solid state physics point of view. For that a energy-band diagram like the one below was considered (see fig. 6.5).

The diagram in fig. 6.5 represents the energy levels in a PIN-diode corresponding to its three regions. The two shown energy bands correspond to the conduction band and below, the valence band. In the valence band electrons which are still attached to their parent atom are found. For a semiconductor at 0 K this band represents the highest possible energy state available for the electrons. All the electrons are distributed in the energy levels below the valence band filling all the levels until this one. These electrons are the valence electrons. The conduction band is occupied by electrons which are free from their parent atom but, in the absence of radiation, this band is empty. In semiconductors, there is a gap between the valence and the conduction bands. This energy gap reflects the amount of energy that is required for an electron to go from the valence band to the conduction band and create an e-h pair. Because increasing the temperature some e-h pairs can be created due to the thermal energy of the system, this explains why the higher the temperature, the better is the conductance in a semiconductor. With temperature the electrons might acquire the needed energy to overcome the gap and take part to the conduction. In intrinsic Si at 0 K the valence band is completely filled, i.e., there are no free electrons and the conduction band is completely empty. Thus, the only carriers that can be found are photo-generated e-h pairs.

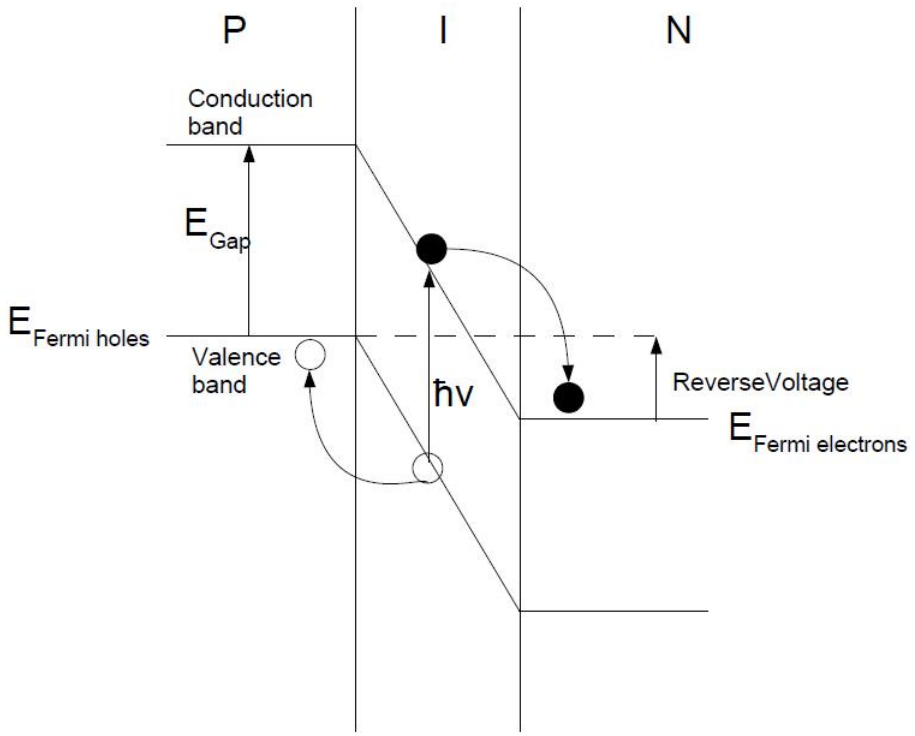


Figure 6.5: Energy level diagram for a PIN-diode. This figure shows how the valence-band and the conduction-band are distributed at the different areas in the diode.

As was already mentioned, the electrodes of the PIN-diode are heavily doped to ensure conductance at low temperatures and an uniform field. The n-type region in Si has a lower internal energy potential than the p-type. When the PIN-diode is at equilibrium, the total chemical potential or Fermi-level is constant across the diode.

The equilibrium is reached through two microscopic mechanisms: diffusion and drifting of carriers. Electrical currents are generated in these two ways and when $I_{diffusion} = I_{drift}$ the Fermi level becomes constant across the diode. The diffusion is produced due to the difference in concentration between the p- and n-contacts. Free charges move to equalize the concentration throughout the diode. On the other hand, the difference in potential between both regions creates a second electric current by the drifting of charges to their opposite-sign side. When the two currents equalize, an area with no free charges is generated: the depletion area where the potential is constant.

When a forward bias is applied, the potential barrier decreases. Eventually, a current appears due to the diffusion of charges. In the case of a reverse bias, the barrier increases and there is no possibility of any diffusion current; this is the non-conducting mode of the diode. In this mode, when a photon interacts with the detector, free

charges (e-h pairs) are created in the depletion area and those are then drifted by the potential.

This feature provides an intrinsic build-in electric field characteristic of the diode. This field is applied across the photodiode even when no potential is applied to the photodiode. The electrodes are then the only place where a permanent exchange of electrons and holes exist. The energy dissipated by a drifting carrier is proportional to the change in its potential energy (see eq. (5.1)).

### 6.3.4 Quantum Efficiency

For every photon detection device, it is very important to determine the light absorption capabilities. This is determined by the absorption coefficient $\alpha$ which depends on both the material of the absorber and on the wavelength of the incident photons. The fraction of light absorbed depends on $\alpha$ as $P_L = (1 - e^{-\alpha d})$ where "d" is the thickness of the absorption layer. The photons absorbed need to have an energy larger than the energy gap – for photons with longer wavelengths the absorption drops sharply (see fig. 6.6).

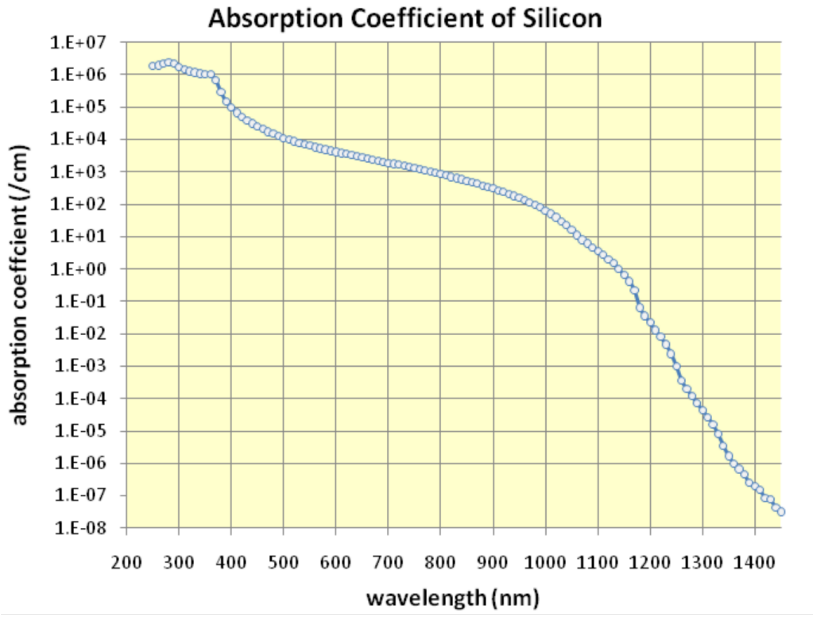


Figure 6.6: Absorption coefficient for Si at room temperature. It can be seen that for wavelengths longer than $\sim$ 1400 nm, $\alpha$ drops to zero. Source: [69, 70].

On the other hand, the longer the wavelength, the deeper the light can be transmitted into the absorber (see fig. 6.7). The values presented here are all taken at room temperatures, therefore, it will be necessary to study these values at mK for a proper characterisation of the absorbed light in the detector.

To quantify the absorption a parameter called external quantum efficiency denominated $\eta_{\text{ext}}$ is used. This parameter quantifies the number of e-h pairs created for an number of incident photons and it is defined as:

$$\eta_{ext} = (1 - R)(1 - e^{-\alpha d}) \tag{6.1}$$

Where R is the reflectivity of the exposed material (see fig. 6.8).

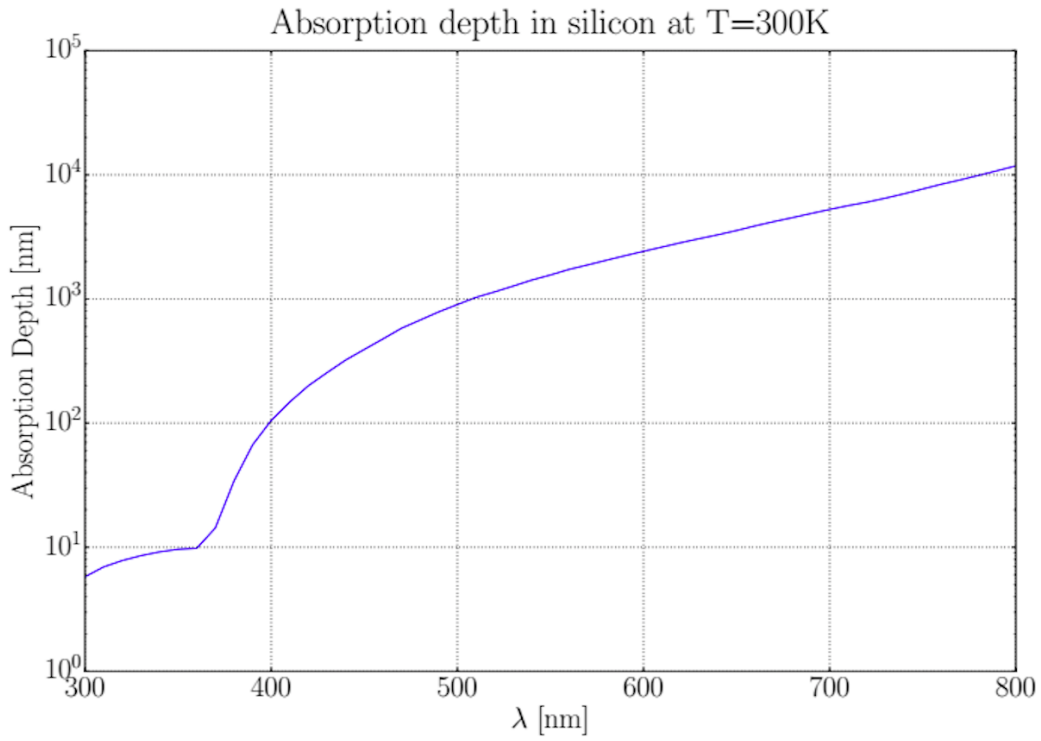


Figure 6.7: Measured absorption depth for different wavelengths in silicon at room temperature. Source: [69, 70].

The quantum efficiency presented here is also denominated External Quantum Efficiency (EQE) and it is always smaller than the Internal Quantum Efficiency (IQE) – the ratio of the number of charge carriers collected by the number of photons for a given energy that irradiate on the detector and are **absorbed** by the detector.

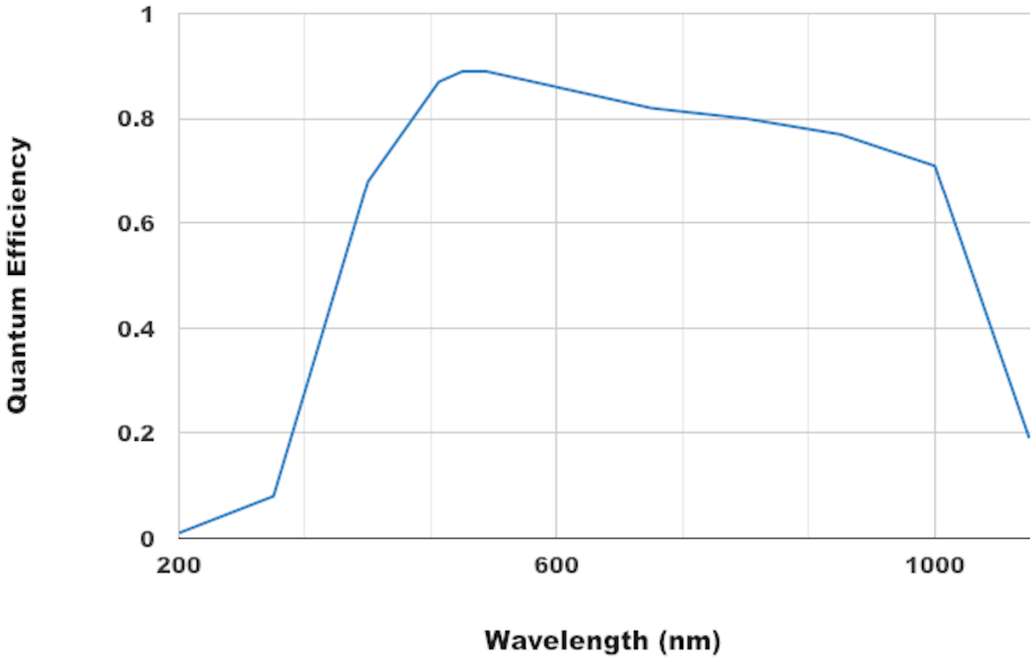


Figure 6.8: Absorption coefficient for a Si PIN-photodiode as the ones used for the experiments. The values are taken from the diode provider and correspond to room temperature. The sudden drop in $\eta$ can be seen when the wavelength is longer than the $\lambda_C$ corresponding to the energy of the Si band gap.

For 430 nm photons in some of the Si-photodiodes at room temperature, the IQE has typically a value of $\sim 0.76$ and a reflectivity of the 44% given by the manufacturer. It is possible to drastically decrease the reflectivity of a photodiode (to a transmission close to 90%) by applying an ARC-coating.

### 6.3.5 Avalanche Photodiode

With a working principle similar to the PIN-photodiodes, the avalanche photodiode (APD) is a similar device that is able to multiply the photo-generated carriers.

APDs multiply the primary photo-current within the diode itself. The photo-generated carriers traverse a high-field region where they collide with bound electrons that become ionized due to the high energy of the carriers – also called impact ionization. This process is then repeated by the newly created charge carriers and the process repeats generating the avalanche effect (see fig. 6.9).

Hence, this device is a very good candidate for testing the NTLE [71] (see section 7.8).

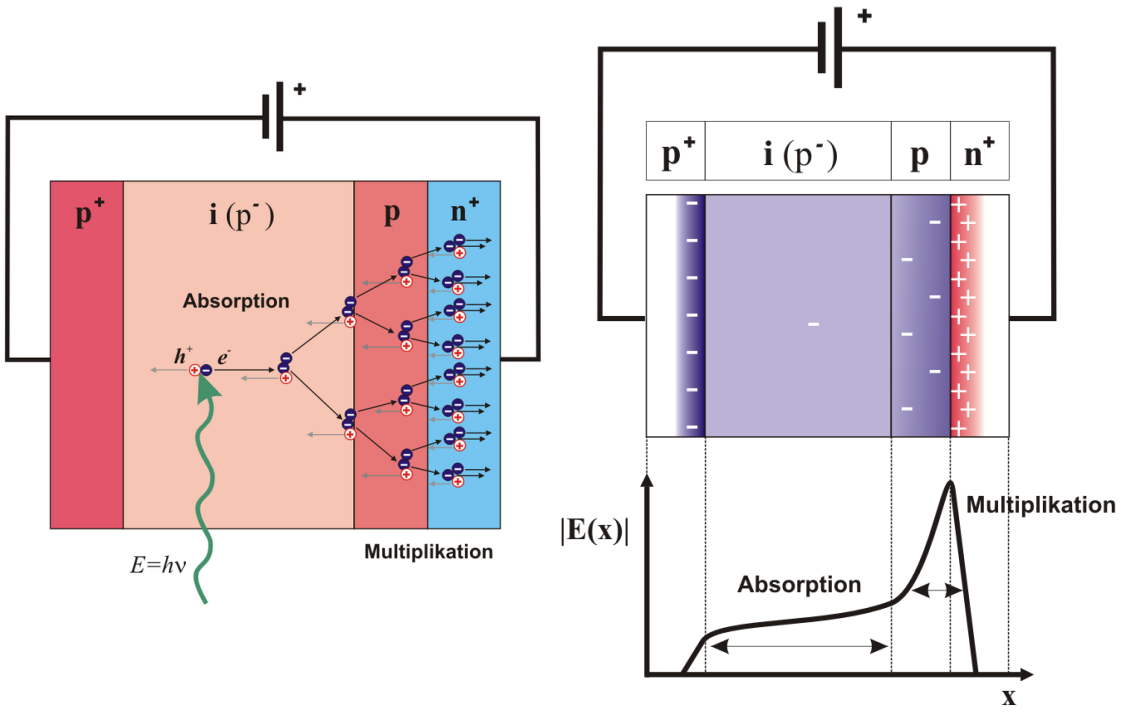


Figure 6.9: On the left: Charge carrier multiplication in a Si-Avalanche-photodiode (APD) under reverse voltage. Colors indicate doping of the corresponding layer. On the right: Si-Avalanche-photodiode (APD) with space charge distribution under reverse voltage (top), and corresponding electric field distribution (bottom).

## 6.4 Charge amplifier

In addition to the experiments measuring the heat signals for different values of $V_{NTL}$, it is also important to measure the charge collection in the detector when varying the applied $V_{NTL}$. These measurements are of great importance since they allow the precise determination of the charge collection efficiency and its evolution with the $V_{NTL}$ voltage applied. This information is thus, complementary with the NTLE amplification measurement (see fig. 6.10).

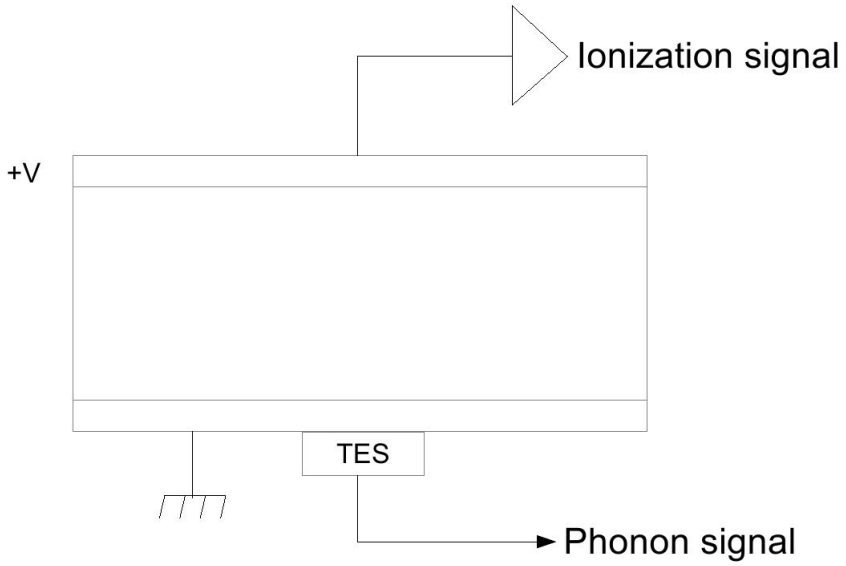


Figure 6.10: In this figure a scheme of the experiment used to measure simultaneously the heat signal and the charge collection from the photodiode is shown.

## 6.5 Energy calibration

The detector was calibrated in two different ways. The first one consists of using an X-ray source which emits at a known energy: this allows measurement of the energy of events by comparing the signal amplitude to the X-ray lines. The detector was also calibrated by sending flashes of 430 nm photons matching the wavelength of the scintillation light from $CaWO_4$ (see in section 6.6.2 how to do the energy calibration with such an excitation). The calibration using X-rays or photons is complementary since the interactions of these radiations is very different.

The sources irradiated the surface of the diode where there was no TES. The reason for irradiating light only on this surface relies on the fact that the TES would contribute with a non-amplified signal disturbing the calculation of the gain. Also, the surface with the TES is reduced in area by the area occupied by the TES. Doing it this way the collection of light is maximized. The reason to shine over the p-doped or boron side is because it provides a very thin window needed to detect the 430 nm photons – the electrode on the n-doped side is too thick for the photons to penetrate into the active volume.

Some characteristics of the X-ray source include:

- The $^{55}$Mn decays emitting Auger electrons at 5.19 keV (these electrons are filtered in the experiments), $K_{\alpha 1}$ and $K_{\alpha 2}$ X-rays at 5.898 keV, and 5.887 keV respectively (because these two energies are so close, they are usually treated as mono-energetic radiation of 5.9 keV), and $K_{\beta}$ at 6.49 keV.

- The radiation is randomly emitted in both time and space. However, when the detector is irradiated the energy deposited is localized to a very small volume.

- The penetration depth is of $\sim$29 $\mu$m for the $K_\alpha$ and $\sim$38 $\mu$m for the $K_\beta$ – most of the X-rays are stopped within the 300 $\mu$m of the photodiode's bulk. Therefore the interaction within the 50 nm boron layer is negligible and all radiation is absorbed in the active volume.

The main features about the interaction of photons with the photodiode are, however, different:

- InGaN-LEDs (Light Emitting Diode) were used to irradiate monochromatic photon-flashes on the detector – it allows the irradiation the detector at a determined time and frequency and with the amplitude (number of photons) required. Light was transmitted to the experiment via an optical fiber. The LED source is outside the cryostat and, therefore, at room temperature.

- Different LED sources with wavelengths ranging from 430 nm to 1080 nm were used. Working with different LEDs makes possible to probe the photodiode in different places because the penetration depth varies by about 2 orders of magnitude between 430 nm and 800 nm photons.

- In contrast with the $^{55}$Mn source, a flash of photons implies that several photons are simultaneously absorbed across a large surface of the photodiode and not at a single position.

- The only part of the photodiode that is sensitive to the 430 nm photons is the entrance window since the back of the photodiode is opaque to this wavelength.

## 6.6 Treatment of the Signal

To make the energy calibration an energy spectrum or histogram is used. To generate this histogram the energy deposited for every event needs to be determined, i.e., sorting out all the events by energy.

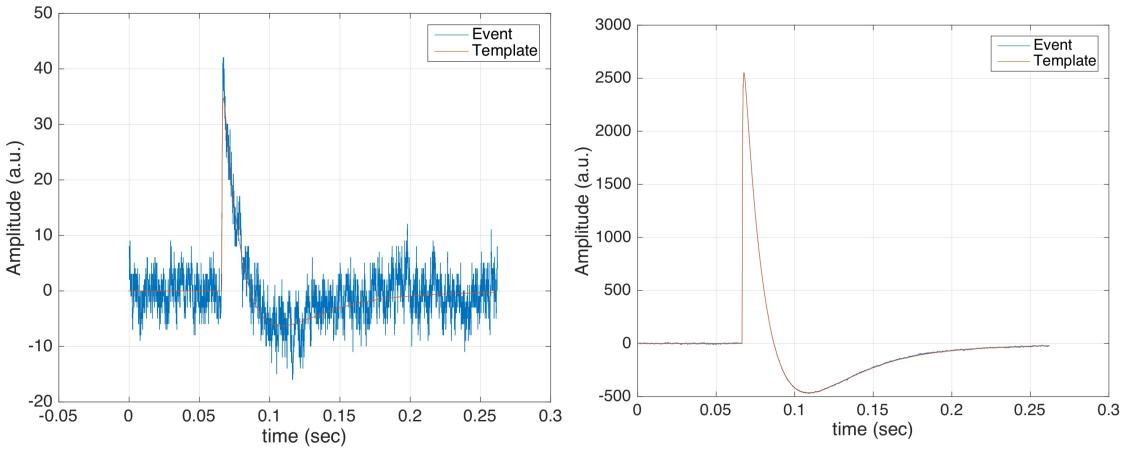


Figure 6.11: On the left: template fitting of a low energy event (pulse in blue, template fit in red). On the right: template fitting of larger energy event. It is noticeable the similarity in the shape of both events despite of the difference in their energies.

For this process a template pulse is produced by averaging selected pulses. In this case $K_\alpha$ pulses were selected to create the template because the energy of the $K_\alpha$-rays emitted by the $^{55}Fe$ is known. To average the selected pulses, the amplitude of the pulses is evaluated at the same height level in two different times (before the rise time and at the end of the decay time). This allows the discrimination of double pulses. It is thus important, to trigger the signal (set the height level) as low as possible to obtain all the possible information about the shape of the pulse. To generate the template, the very noisy events and events with strange shapes were remove from the samples.

Once the template pulse is created, all the recorded signals with the template pulse are fitted – signals that are above the trigger level. The events to fit are taken during not very noisy periods to avoid huge microphonics. No difference in the shape of the pulse was noticed for different nature of event. When the events are all fitted, they can be sorted by energy through their size-ratio with the template pulse – how much is the template pulse stretched or shrink to fit the event pulse. In fig. 6.11 the fitting of a low energy event and a larger energy one can be seen.

The template pulses are also used to obtain the baseline noise. The baseline noise is obtained by treating random trigger samples like signals, that is, events that do not correspond to a particle pulse. The random noise samples are hence acquired by setting a random trigger additionally to the other trigger. The noise samples are fitted with a template in the same way as the thermal signals. Once the energy spectrum is generated (fig. 6.12), the noise peak is centered at zero and fitted with a Gaussian. The FWHM of this peak gives the $1\sigma$ baseline noise (FWHM$= 2.35\sigma$). The amplitude of the thermal signal divided by the $1\sigma$ width of the baseline noise gives the signal-to-noise ratio.

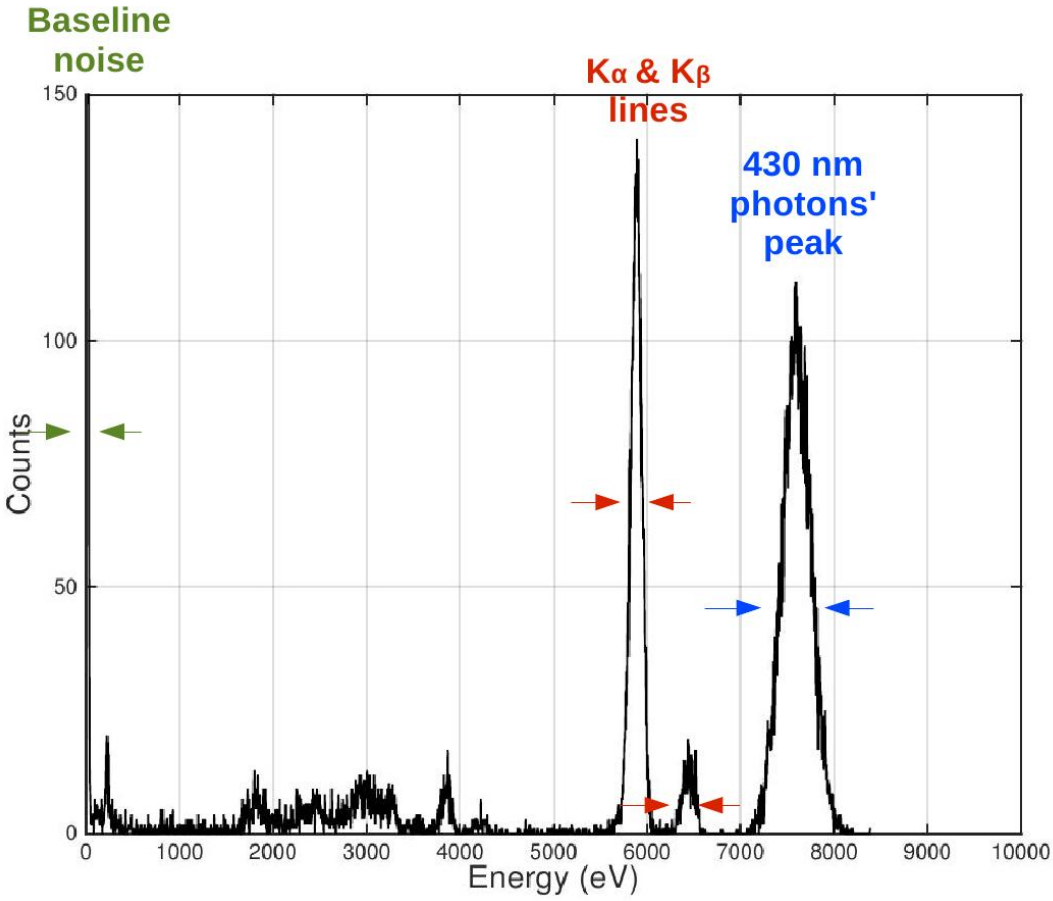


Figure 6.12: Energy spectrum for the signals taken at 97 $V_{NTL}$. The FWHM is indicated for the baseline noise, the K-$\alpha$ and the K-$\beta$ lines and the 430 nm photon peak.

### 6.6.1 Energy calibration using the $^{55}$Fe's lines

The $^{55}$Fe emits X-rays at rather high energy; X-rays deposit all their energy in one small volume of the bulk of the detector. To make the energy calibration using the $^{55}$Fe, it is necessary to build up an histogram that registers the events in the diode at different energies (see fig. 6.13). This process was done at a fixed $V_{NTL}$ – depending on the experiment and the diode.

It is immediate to identify the $K_\alpha$ and $K_\beta$ lines of the $^{55}$Fe because of their distance and height ratio – their high energy deposition and their proportions between each other (the flux of $K_\alpha$-rays is roughly 10 times higher than the $K_\beta$ ones).

Once those two lines are well identified and set at their corresponding energies (5.9 keV and 6.49 keV), it is possible to start the identification of the other lines and studying their origin depending on their energy.

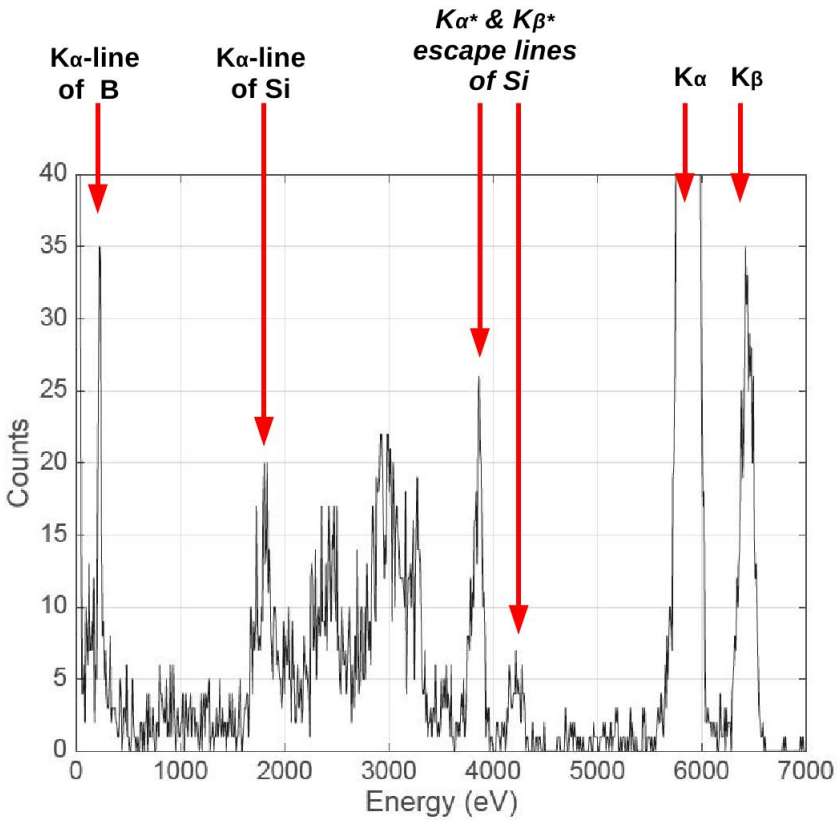


Figure 6.13: In this figure an energy spectrum made at 97 $V_{NTL}$ can be seen. The $K_\alpha$ and $K_\beta$ lines of the $^{55}$Mn that serve as reference to make the calibration can be clearly seen. These lines not only provide an energy mark-point, but are also quite distinctive because of their profile (amplitude, distance between each other...); thus, they provide a very effective way to calibrate the energy.

In other words, this process consists of identifying straight forward the contribution to the total energy deposition from the different signals occurring in the diode which allows the study of its origins. Therefore, this method is very useful when the resolution is good enough to define the $^{55}$Fe lines.

The histogram of the amplitude of the events is shown in fig. 6.13. Besides the $K_\alpha$ and the $K_\beta$ other features at different lower energies can be distinguished. When the incident photons ($K_\alpha$ or $K_\beta$ from the $^{55}$Fe source) enter the silicon detector, 90% of them are absorbed by the Si K-shell electrons and Si $K_\alpha$ is yielded in the relaxation process. Most of the time this secondary radiation is deposited within the detector. Considering the time scale, this process is invisible. But if the Si $K_{\alpha*}$ photon escapes from the detector, the total energy deposited is decreased by 1740 eV (the $K_\alpha$ of the Silicon giving an energy E = 5.9 keV - 1.8 keV). The same happens for the $K_\beta$. This is how the escape peaks occur. In addition to the escape lines, the presence of even lower energy events are noticeable. During these events, the initial photon excites an atom of Si or B before escaping. Only the $K_\alpha$ of Si or Boron are left.

### 6.6.2 430 nm-photons calibration

The LED emits a packet of 430 nm photons (each having an energy of 2.88 eV which corresponds to 430 nm) illuminating the whole surface of the detector for each event. The number of photons fluctuates for every event and follows a Poissonian distribution (section 5.2.2). The trigger signal for the LED is recorded to identify the signal on the detector as a photon signal. Additionally, a random triggering is used to take noise samples and compute the energy threshold (see section 7.4.3).

As mentioned before, when energy is deposited within the detector and the temperature rise is measured with the TES. In order to estimate the energy deposited for every event, the signal is fitted using a pulse template as explained in section 6.6.

A 430 nm LED was used for this calibrations. By sending 250 ns pulses on the LED at 3 Hz during two minutes, and changing the pulse voltage from 1.5 to 4 volts, the amplitude of the LED-pulses (i.e. the average amount of photons sent for each pulse) was modified. This process was done at 97 $V_{NTL}$. Each obtained peak is fitted with a Gaussian. After obtaining a series of different peaks corresponding to each amplitude, the width of the Gaussian fits is plotted as a function of the mean of the Gaussian ($\sigma$) – sigma versus amplitude [66, 67]. See fig. 6.14).

The fluctuations have two main contributions; the noise component ($\sigma_{\text{cnt}}$), which is constant, and the poissonian contribution ($\sigma_{\text{Poisson}}$), which is energy dependent. Therefore, the relations between the hights of the pulses and the number of photons N and their resolutions can be expressed as:

$$x = aN \tag{6.2}$$

$$\sigma_{Poisson} = a\sqrt{N} \tag{6.3}$$

$$\sigma^2 = \sigma^2_{Poisson} + \sigma^2_{cnt} \tag{6.4}$$

$$\sigma = \sqrt{a^2N + \sigma^2_{cnt}} = \sqrt{xa + \sigma^2_{cnt}} \tag{6.5}$$

Where $a$ is a scaling factor and $x$ is the amplitude. It can be seen from equation 6.5 that it is possible then to relate the resolution $\sigma$ with the pulse height. It is also possible to determine the scaling factor as well as the value of the constant contribution to the resolution by fitting this equation as in Figure 6.14. When determining them, the number of photons for each peak can be calculated. Since the energy of 430 nm photons is known (2.88 eV), by multiplying this energy by N the total energy emitted by the light source can be obtained and then the detector can be calibrated using this energy peak.

This method can be used to not only make an energy calibration, but also to determine the energy resolution. Moreover, small energy depositions are also measurable, which is of great interest in the context of CRESST.

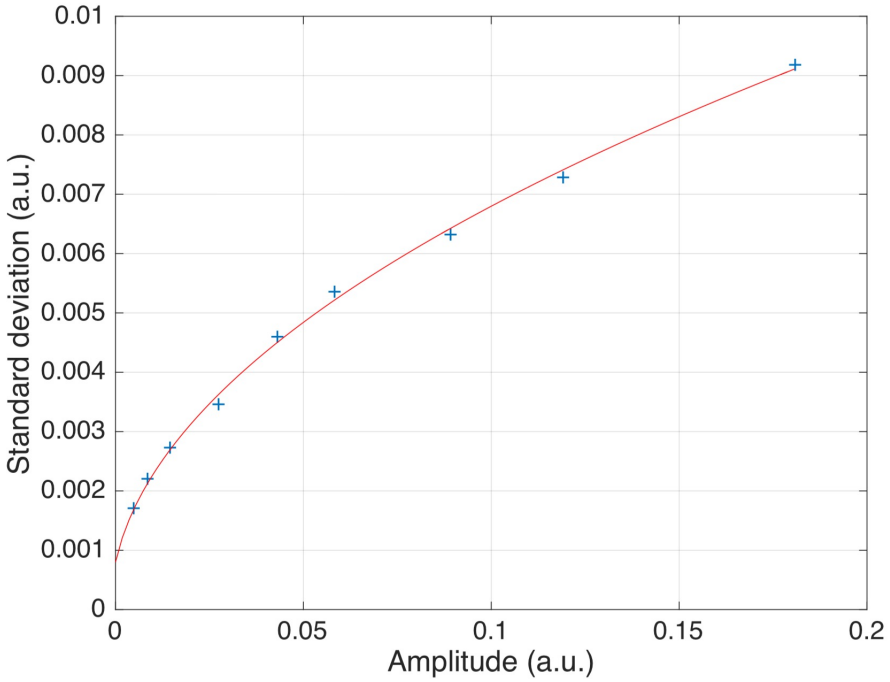


Figure 6.14: Plot of the $\sigma$ values vs. the amplitude for several photon pulses, used for the LED-calibration. Despite the fact that there are not plenty of data points (particularly at low energies) the validity of the result can be studied by comparing it with the value obtained with the X-ray resolution as will be seen in section 7.4.

# Chapter 7

# Results

## 7.1 Proof of principle

In this chapter the most important results obtained within this thesis will be presented and discussed. However, in order to provide the reason to do certain experiments, it is convenient to present a few preliminary experiments and their results, since they provide the preamble to the experiments conducted later on.

In March 2015, the first experiment taking advantage of a planar geometry for NTLE-detectors was performed at the E15. This experiment used a modified commercial device (see Fig.7.1) and a TES produced at the E15. The detector consisted of a Si-photodiode with implanted contacts. The study consisted mainly of a proof of principle.

However, several factors influenced negatively on the outcome of the experiment:

1. The TES had to be glued on the active surface since the other surface was covered by the ceramic housing of the diode.

2. The PIN-diode was impossible to be unglued or removed from this ceramic housing.

3. The back part of the photodiode was entirely covered by gold, which increases dramatically the heat capacity of the device.

The first and second aspects reduced significantly the detecting surface of the detector and the absorbed light. Placing the TES on the surface also produced an input signal from the TES itself – in Fig.7.3 it can be seen that for different $V_{NTL}$ applied the signal develops into two different signals with different time constants. Meanwhile one (the fast one) remains the same for different $V_{NTL}$, the other (the slow one) evolves in both the simulations and in the experimental data, into a longer pulse. Only the slow one exhibits amplification, for being the one coming from the photodiode. The fast pulses correspond to the photon interacting directly within the TES.

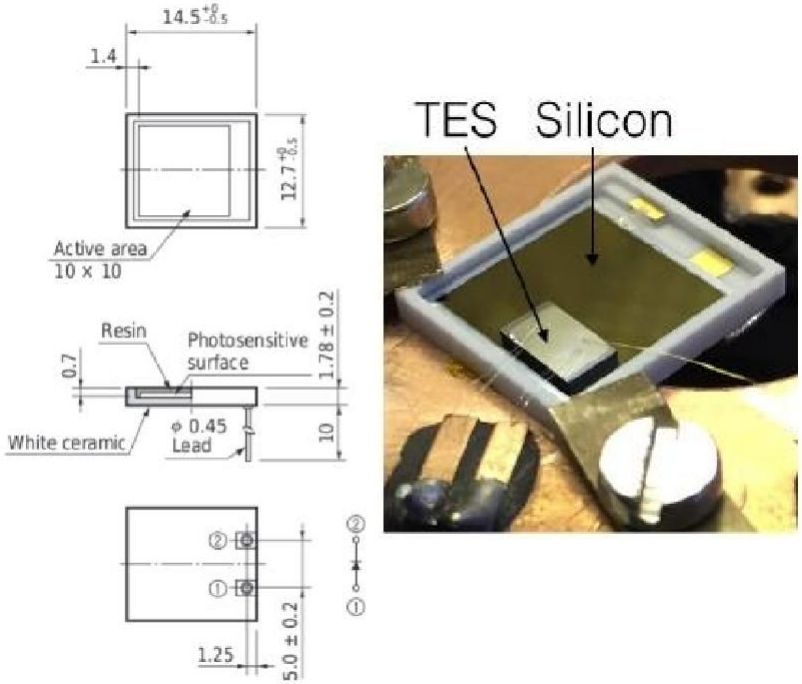


Figure 7.1: Left: Scheme of the Hamamatsu photodiode used for the first experiment. Right: Picture of the photodiode with the TES attached and the bonded links to the SQUID and the thermal bath.

This can also be seen by observing the plot of the decay time versus pulse height; for the amplified NTL-signals, the slow component is proportional to the pulse increase. Meanwhile the other contribution is not influenced by the $V_{NTL}$ as would be expected from a signal coming from the TES.

The ceramic housing and the gold, on the other hand, produced a very large heat capacity. These factors affected the possible resolution achievable by such a neat NTLE-detector. Nevertheless, this experiment was the first proof of principle showing the viability of such an NTLE-device.

The next step consisted of using a same quality bare photodiode that could be delivered without any sort of external packing and with no coating on the surface. Also, following the discussion about the noise from section 5.2.4, it is very important to enhance the thermal contacts. This detector presented an unique feature with respect to the bare photodiodes used for further experiments: it had an ARC-coating (Anti Reflecting Coating) on the surface that could not be delivered for the other photodiodes later on used.

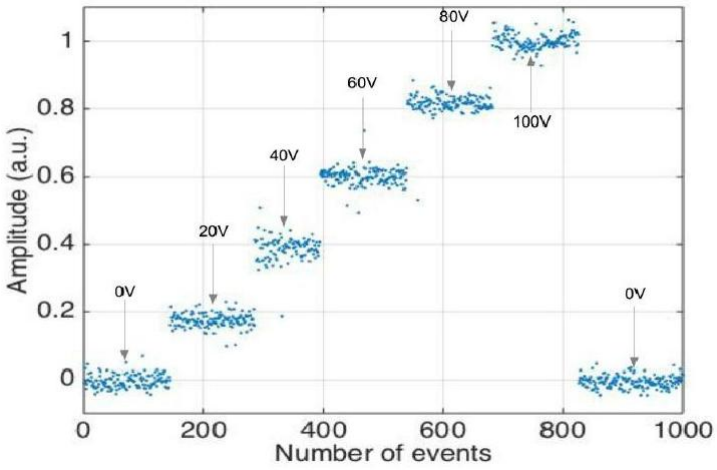


Figure 7.2: This plot shows the amplitude of the low time constant thermal signal from 425 nm photon flashes (emitted by an LED) for different $V_{NTL}$ applied on the photodiode. The amplitude of the signal increases linearly with the voltage applied across the photodiode which validates the principle of the detector.

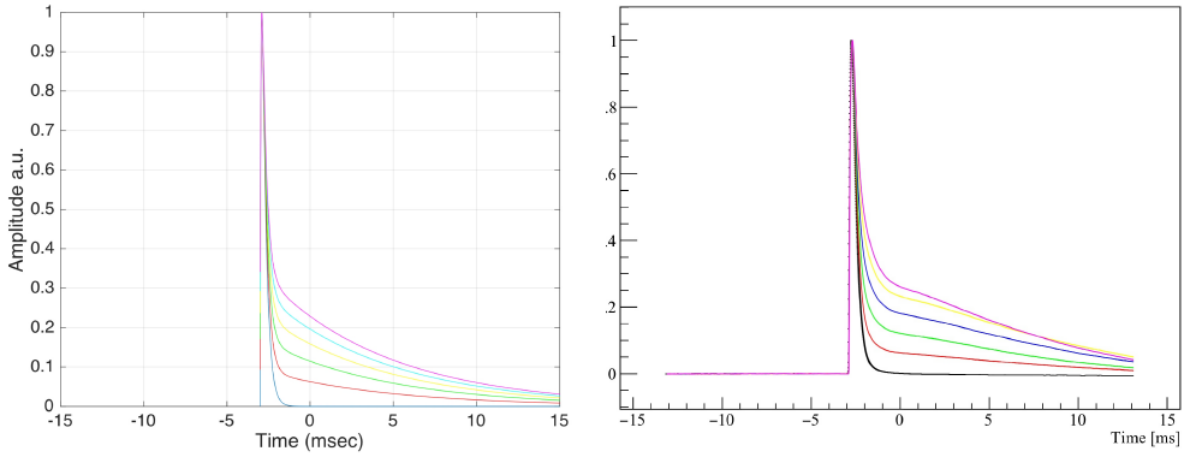


Figure 7.3: Left: simulations of the pluses amplitude vs. time for the Hamamatsu photodiode at different $V_{NTL}$. Each colour corresponds to a different $V_{NTL}$. For the higher $V_{NTL}$ the amplitude exhibits a double decay time (one faster that coincide with the tail at 0 $V_{NTL}$ in blue, and one slower that elongates the tail).
Right: plot of the data obtained for different $V_{NTL}$ applied. It can be seen that the experimental results match the predictions very well.

## 7.2 Experiment with custom photodiode

In the following, the experiments using several Si-PIN-diodes with no-packaging to conduct different studies on the NTLE are presented. To see in detail what diode was used for each experiment, see appendix A.

The entrance window consisted of a very shallow boron implanted contact featuring a high transmittance for 430 nm photons. A bulk of the NTLE detector is made of high-purity intrinsic silicon, and the back electrode consisted of an ohmic contact with an Aluminium layer. The specific details about the experiment can be found in chapter 6.

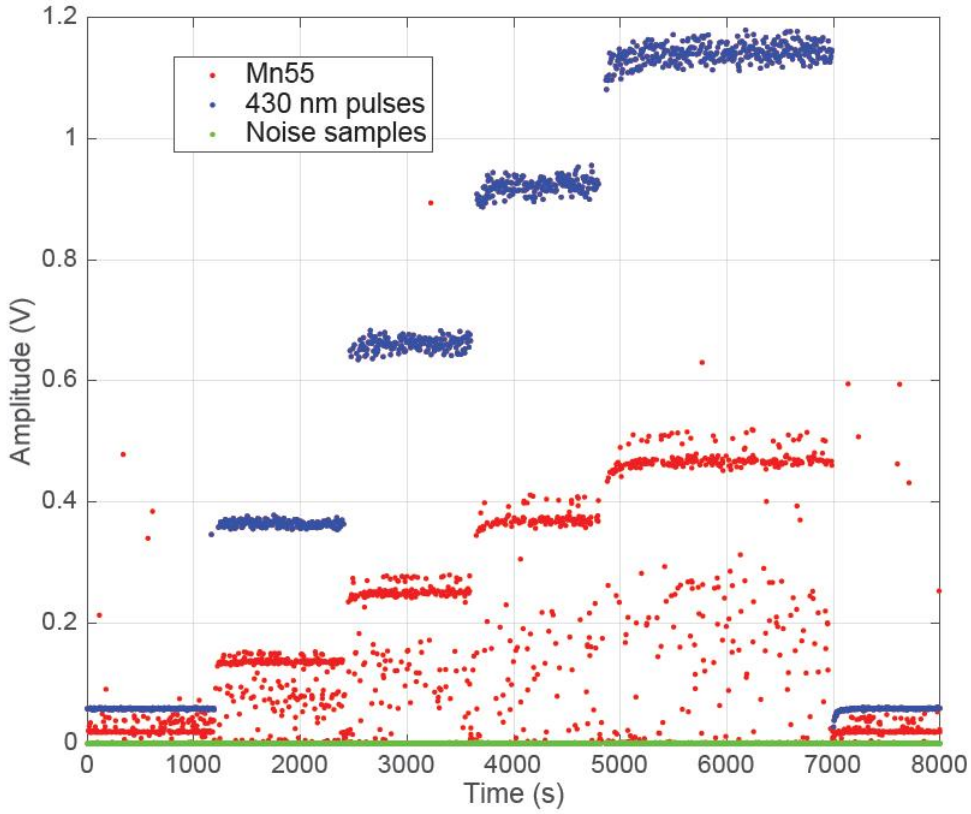


Figure 7.4: Amplitude vs. Time for different $V_{NTL}$. Photon's amplitudes are represented in blue and X-rays' in red. The different amplitudes from left to right correspond to the five steps at 0 V, 25 V, 50 V, 75 V and 97 V. For both signals, 430 nm photons and X-rays, increase with the $V_{NTL}$. The K-$\alpha$ and the K-$\beta$ lines can also be seen.

The first experiment consisted of irradiating the detector with blue photons and X-rays for $V_{NTL}$ going from 0 V to ~100 V in five different steps. The outcome of this experiment is shown in fig. 7.4. Here it can be seen how the amplitude of the

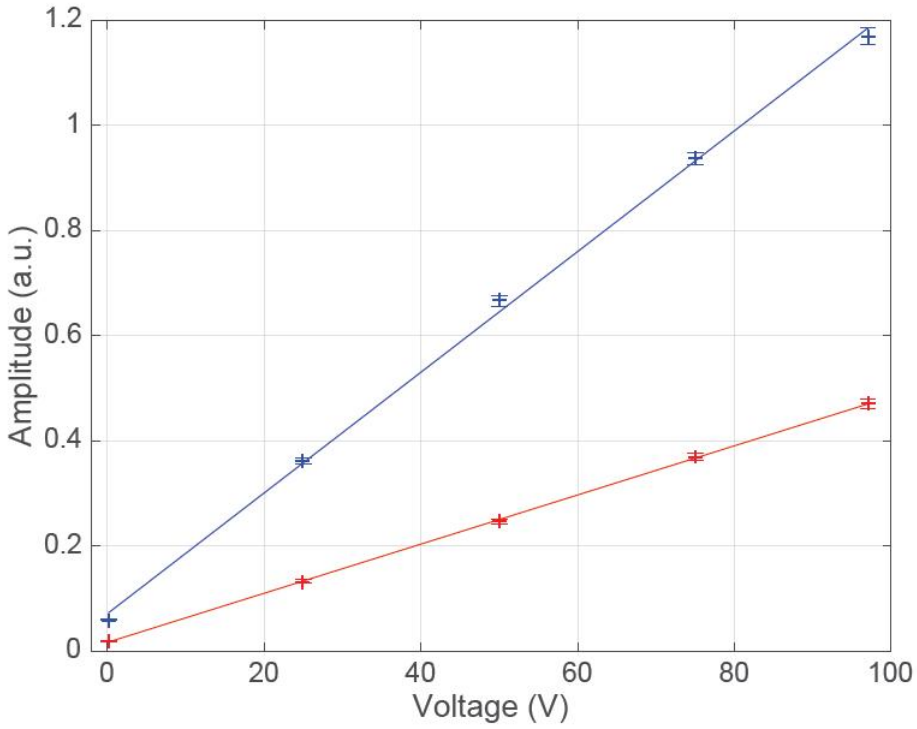


Figure 7.5: Plot of the signal's amplitude vs. voltage applied. In blue the line for 430 nm photons and in red the one for X-rays. Source: [63].

pulses increases when increasing the $V_{NTL}$. The blue dots represent 430 nm photon flashes events (unambiguously determined by the trigger signal from the LED) and the red dots represent events from $^{55}$Fe. From the plot, it can be also been seen that this increase of the signal with the $V_{NTL}$ follows a linear behaviour for both the photons and the X-rays. This is expected from the theory, but is seldom obtained by experiments using configurations other than the planar geometry. Another thing to note is that the higher the $V_{NTL}$, the better the resolution seems to be. Even this does not look so obvious for the photons (the Poisson effect on the width of every signal can be seen), it is clear for the $^{55}$Fe where the K-$\alpha$ and the K-$\beta$ lines can be distinguished. The next section will show this in more detail. Figure 7.5 shows a straight line fitted to the data for amplitudes vs. the voltage applied.

## 7.3 Charge Collection Measurements

Knowing when the the detector is fully depleted is crucial to determine when it is possible to assume there is a total collection of the e-h pairs generated. Figure 7.6 shows how the charge collection increases with the $V_{NTL}$ until it reaches a constant value at $\sim$ 40 V for 430 nm photons. For 700 nm photons, the depletion occurs at a lower $V_{NTL}$ already. For longer wavelengths, the photon penetration is deeper.

The maximum electric charge measured was normalized to one. By looking at the fig. 7.6 it can be assumed that when a photon penetrates within the intrinsic part, the probability to create an e-h pair is very close to 1.

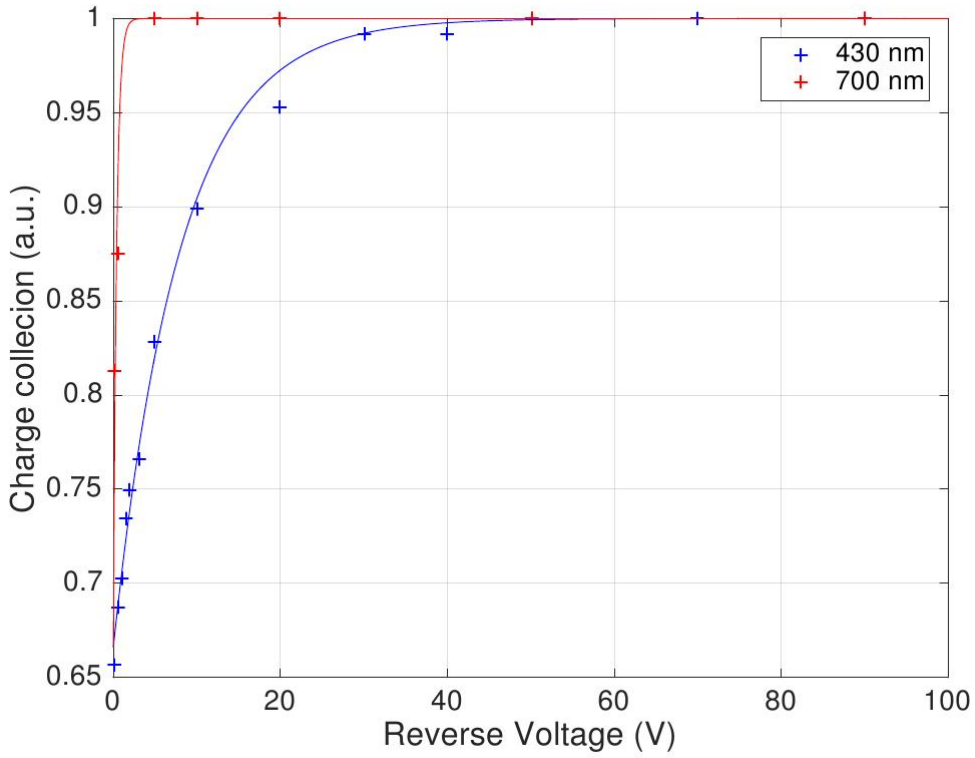


Figure 7.6: This graphic shows the charge collection for both 700 nm photons (in red) and 430 nm photons (in blue) plotted against the $V_{NTL}$ applied. It can be seen that for the photons with larger wavelength, the charge collection is maximal at a much lower V than for the shorter wavelength photons. This occurs due to the fact that the 700 nm photons penetrate deeper into the absorber where the diode is already depleted for low $V_{NTL}$.

The QC needs, therefore, to be taken into account in the equation of the gain (eq. (5.2)) to account for the effect of the collection at the different $V_{NTL}$ applied. This will be seen in the next section.

The nature of the absorbed photon signal is already Poissonian and no additional Poisson fluctuation is added by creating e-h pairs. In other words, since no additional energy is given to the system and it is possible to quantify all of it, fluctuations in the total energy are not longer expected as it happens at 0 $V_{NTL}$. This is particularly important for the purposes of this work, since measuring and determining a number of photons is the ultimate goal.

## 7.4 Thermal Gain

In this section the results of the obtained energy resolution, energy threshold and base-line noise are provided. The obtained results and their implication in the context of the CRESST experiment will be commented.

One of the most important study of this masters is the evolution of the amplitude of the phonon pulses as a function of $V_{NTL}$: the thermal gain induced by the NTLE.

### 7.4.1 Transmission contribution to the Gain

To calculate the energy gain for the different $V_{NTL}$ applied experimentally, the signal's amplitude at each $V_{NTL}$ is divided by the amplitude at 0 V. The experimental gain data points for the 430 nm photons and the theoretical line (in red) are shown in fig. 7.7. To calculate the theoretical gain, equation 5.2 must be modified by adding a couple of terms regarding the charge collection efficiency and the transmission of the entrance window:

$$G = 1 + \frac{e \cdot V_{NTL} \cdot T \cdot QC(V)}{\varepsilon_{e-h}} \tag{7.1}$$

Where T is the transmission and QC is the charge collection efficiency. Adding these terms, a theoretical line for the gain which matches accurately the experimental one obtained.

For a fixed $\epsilon_{e-h} = 2.883$ eV, and considering the values from the charge collection at different $V_{NTL}$ taken from the charge collection experiment (see fig. 7.6), a value for the transmission of $T = 0.764 \pm 0.005\%$ was obtained. The transmission value given by the producer of the PIN-photodiode at room temperature is T=0.756%. The provider did not provide error bars for this value.

In fig. 7.8 the experimental gain for 430 nm photons is shown for both forward (in blue) and reverse (in red) $V_{NTL}$ applied (from ∼1 V to 10 V). The red line corresponds to the fit to the reverse bias data points. The first thing to observe is that the gain seems to be larger for forward voltages than for reverse voltages. The reason for this constant difference in the gain is due to the fact that in the forward voltage regime the field applied is increased by the internal field of the photodiode. This is also a very remarkable result because proves that for low $V_{NTL}$ the NTLE is still valid for forward voltages even higher than the gap. For forward voltages higher than +9 V the leak currents were too significant. Hence, it can be deduced that in this regime the total energy increases with the $V_{NTL}$ and the detector is collecting charges of the opposite sign. A way to explain this phenomenon is due to the formation of a potential barrier between the impurities band at the n-region and the conduction band at the intrinsic region. In the same way, this potential barrier

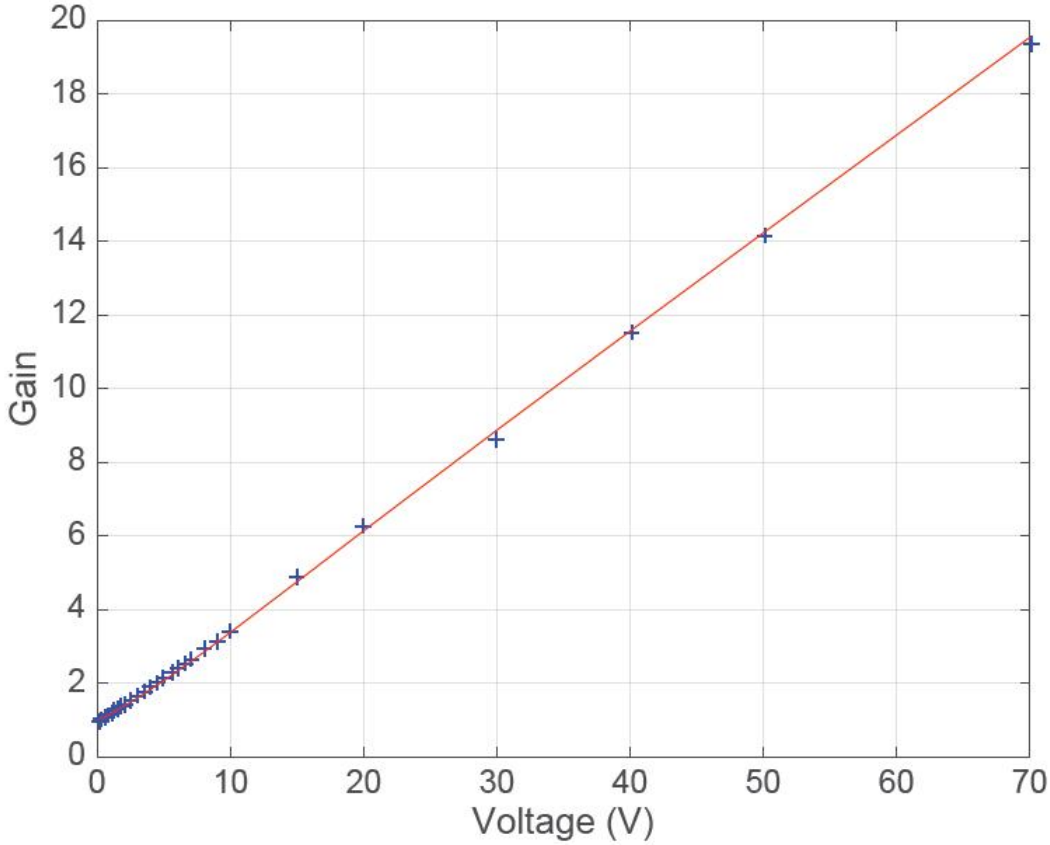


Figure 7.7: Plot of the Gain for 430 nm photons at different $V_{NTL}$ (blue data points). The red line represents the theoretical gain for 430 nm photons according to equation.5.2 with an $\epsilon_{ph} = 2.88$ eV.

would exist between the impurity band at the p-region and the conduction band at the intrinsic region [74, 75].

The second important thing to be observed is that in the region of very low voltages (below 2 $V_{NTL}$) the response of the detector is not as good as for high $V_{NTL}$ applied. The explanation for this phenomenon comes from the fact that the penetration depth of the 430 nm photons is very short in comparison to the detector's thickness. This means that for low voltages, there is a local area in the detector, near the electrodes, that has not been fully depleted. This area corresponds to the reaching location for the 430 nm photons. This, in turn, means that when a 430 nm photon reaches this area at low voltages, the e-h pairs created are not fully collected and the gain is not complete. This effect is also apparent in the experiment of the charge collection: from observing fig. 7.6 the detector is not fully collecting the charges until a $V_{NTL}$ of 40 V is applied in the case of the 430 nm photons.

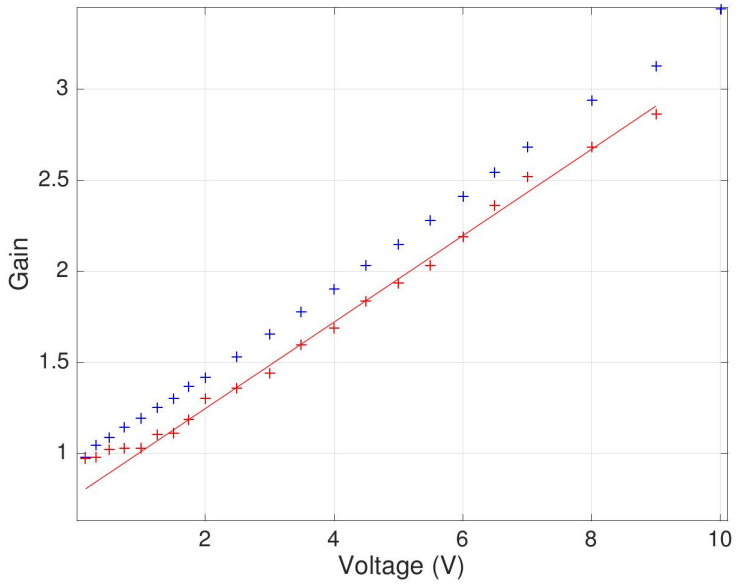


Figure 7.8: Gain plot for both reverse (red) and forward (blue) low $V_{NTL}$.

### 7.4.2 Evaluation of the baseline noise

In fig. 7.9 the first pulse for 0 V applied and for ∼100 $V_{NTL}$ is shown. At first sight it is striking to see how the signal *smooths-up* when a high $V_{NTL}$ is applied. What this smoothness shows is the improvement gained in the signal-to-noise ratio (amplitude of the thermal signal divided by the 1-$\sigma$ width of the baseline noise).

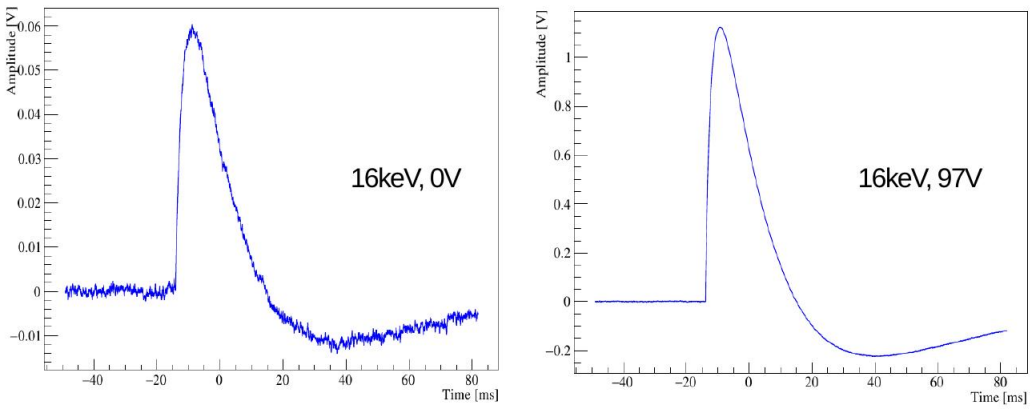


Figure 7.9: In these two graphs, the thermal pulse signal for 430 nm photons at 0 $V_{NTL}$ (left) and for 97 $V_{NTL}$ (right) are shown.

During all the measurements, the amplitude of the baseline noise (see section 6.6) remained independent of the NTLE voltage applied (see fig. 7.10). This implies that the signal-to-noise ratio increases proportionally with the $V_{NTL}$. This also means a

significant improvement compared to other NTLE-detectors geometry [64, 65, 66, 67]. Usually, increasing the $V_{NTL}$ would also affect the noise.

The $1\sigma$ width of the baseline noise calibrated with the $^{55}$Fe calibration lines corresponds to a value of 5.33 $\pm$ 0.41 eV. Using the LED-calibration (fig. 6.14) a $1\sigma$ baseline noise of 5.00 $\pm$ 1.30 eV was obtained. This value is consistent with the one obtained with the $^{55}$Fe's calibration. All values were obtained at 97 $V_{NTL}$.

Figure 7.11 shows the evolution of the signal-to-noise for different $V_{NTL}$. First thing to notice from the plot is that the signal-to-noise ratio has a steeper slope for the $^{55}$Fe than for the 430 nm photons. This is due to their different values for the gain and the transmission. Second, is the the linearity of the lines. This is, of course, a consequence of the linearity in the amplification and also from the steady behaviour of the noise. It can also be seen in the plot the values of this ratio from a lateral field configuration experiment [66] – the planar field NTLE-detector's geometry thus presents an improvement in terms of noise as well.

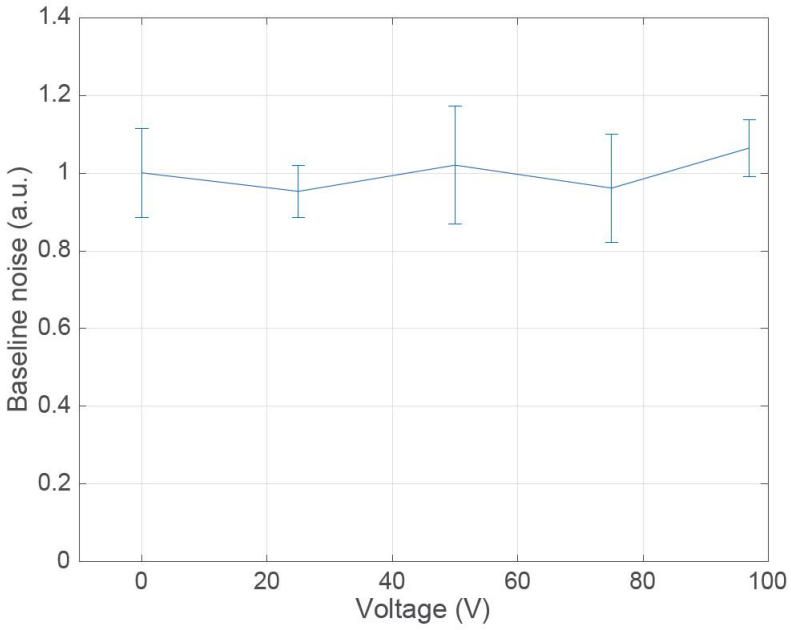


Figure 7.10: Evolution of the baseline noise for different $V_{NTL}$ applied. The five data points were normalized to the baseline value at 0 V. The data points correspond to 0 $V_{NTL}$, 25 $V_{NTL}$, 50 $V_{NTL}$, 75 $V_{NTL}$ and 97 $V_{NTL}$ respectively.

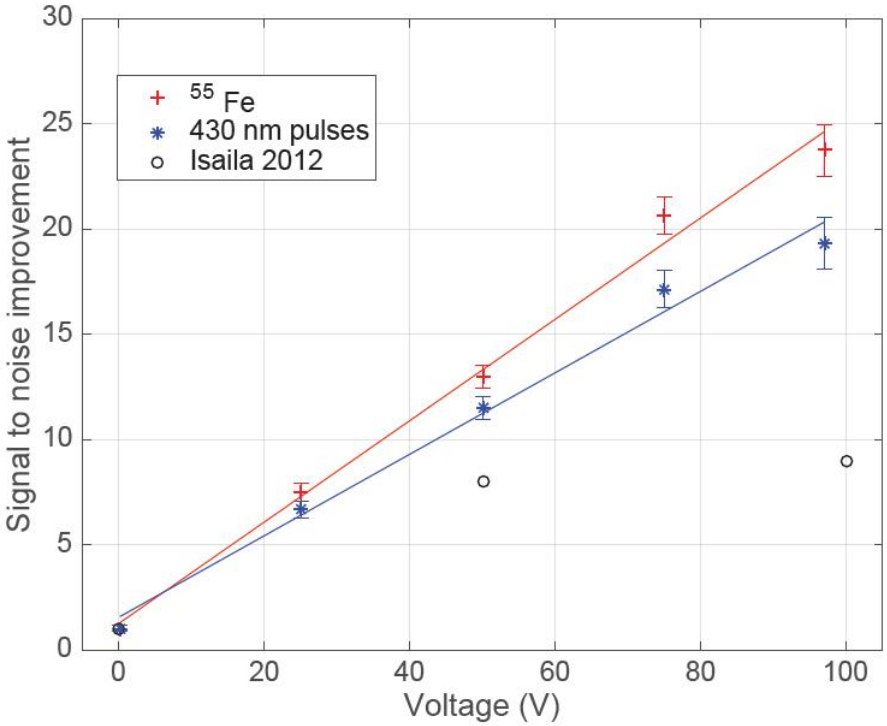


Figure 7.11: Evolution of the signal-to-noise ratio for different $V_{NTL}$. In red the values for the $^{55}$Fe, in blue the values for the 430 nm photons and the black circular dots corresponding to the data obtained for a lateral-field configuration NTL-detector from [66].

### 7.4.3 Energy Threshold

The energy threshold can be calculated straight from the $1\sigma$ baseline noise that for the case here is $\sim$5 eV at 97 $V_{NTL}$. Multiplying the $\sigma$ by a factor 5 an energy threshold $E_{Th}$ is obtained:

$$E_{th} = 5 \ \cdot 5 \text{ eV} = 25 \text{ eV} \tag{7.2}$$

Considering that the photon energy for the 430 nm photons is $E_{ph} = 2.88$ eV, the baseline noise result needs to be improved by a factor 4 to be able to resolve single photons.

### 7.4.4 Energy resolution of the X-ray peak

To measure the energy resolution of the X-ray peak, the K-$\alpha$ and the K-$\beta$ lines of the $^{55}$Fe were used (fig. 7.12). By fitting a Gaussian to the result the sigma value can easily be obtained and used to calculate the energy resolution at a given energy. The resolution of the detector at 5.9 and 6.4 keV has a value of $127.4 \pm 3.8$ eV. This value is compatible with the 120 eV theoretical resolution obtained from eq. (5.5) with an $\epsilon = 3.6$ eV. Looking at the result it can be concluded that the resolution

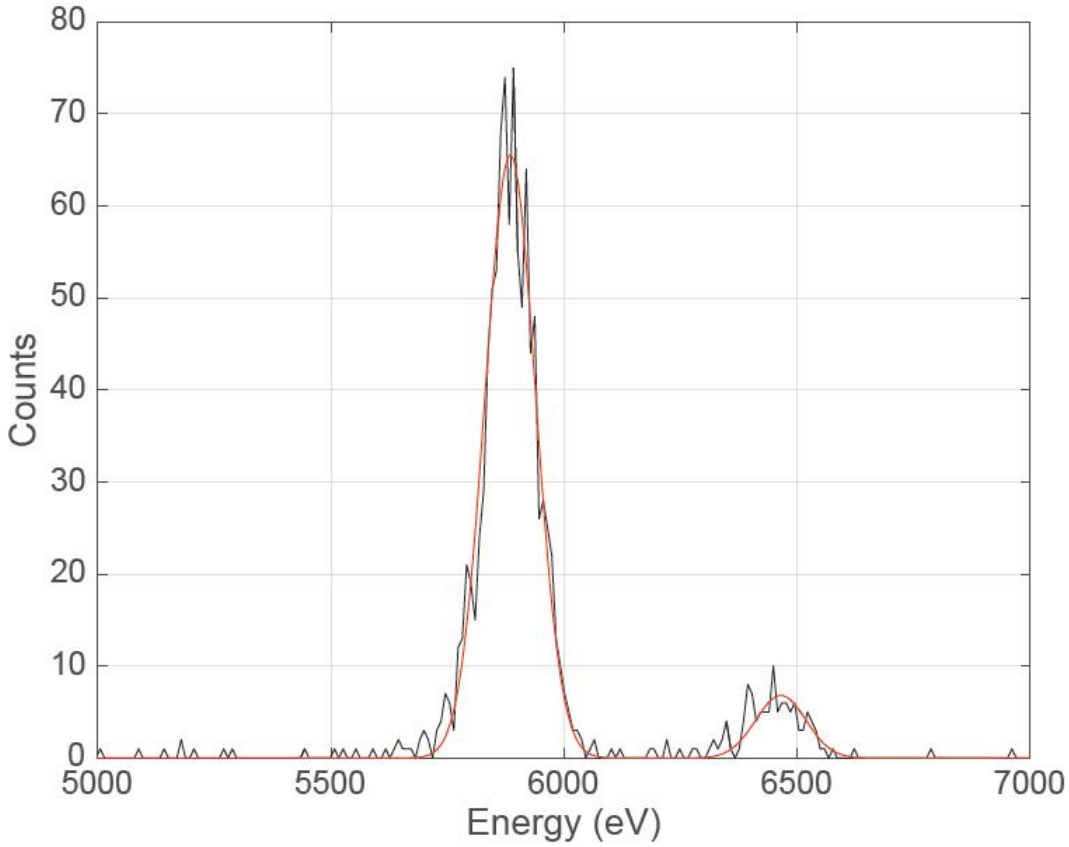


Figure 7.12: In this graph the $^{55}$Fe spectral peaks can be seen. The red line corresponds to the Gaussian fit. Source: [63].

of the detector indicates an homogeneous collection, i.e., there is negligible position dependence. For a detector with position dependence, the obtained FWHM would be wider and the experimental result would not match the theoretical value. This also implies that the resolution at these energies of this detector is mainly limited by the Poisson statistical fluctuations.

## 7.5 Study of the degradation

Historically, one of the obstacles found when studying the implementation of NTLE-detectors, is their degradation with time. It happens that after certain time of applying the $V_{NTL}$, a decreasing in the thermal signal's amplitude has been observed (see [67] for example). This degradation with time is probably due to the charges trapped on defects and on the surface near the electrodes. The accumulation of these charges with time creates a counter-electric field that reduces the NTLE expected for certain $V_{NTL}$.

The main motivation to start the study of the planar geometry for NTLE-detectors was to reduce this degradation – by placing the electrodes over the surfaces, the possibility to trap charges on the surfaces would, in theory, disappear to a great extent because the improvement in the charge collection (explained later in section 7.3).

For all the planar geometry detectors studied in this thesis, i.e., different sizes, Al and no-Al coating (section 7.7), long runs at high and lower $V_{NTL}$ etc., no degradation was observed whatsoever.

Therefore, a dedicated experiment thought to create the optimal conditions for degradation in the diode was performed in order to see how the detector would degrade. The detector was exposed to a very high flux of photons and then the evolution of the amplitude of the phonon signal was studied under different conditions. This experiment consisted of three steps:

1. The detector is calibrated with $^{55}$Fe and 430 nm photon flashes during 300 seconds with a $V_{NTL} = 97$ V. The photon flashes were at a rate of 0.5 Hz.

2. After this time, the flux is multiplied by 10000 times to 5000 Hz. This corresponds to a power of 100 MeV/s. This created a large number of charges. During this phase, no signal could be measured from the TES because the signals consisted of pile-up events only. The NTLE voltage is kept at 97 V during the ∼150 s this step lasted. The large number of charges created constitutes extreme degradation conditions.

3. Then the rate was decreased back to 0.5 Hz and it was observed how, after just a few seconds, the signal recovered the same value it held before changing the flux frequency (see fig. 7.13).

This experiment proves the non-degrading feature that the planar geometry presents for NTLE-detectors. This result is very important for the application of NTLE detectors in rare event experiments, since it implies that such a detector, in contrast with previous NTLE detectors, does not need any charge regeneration procedure and presents a very reliable charge collection.

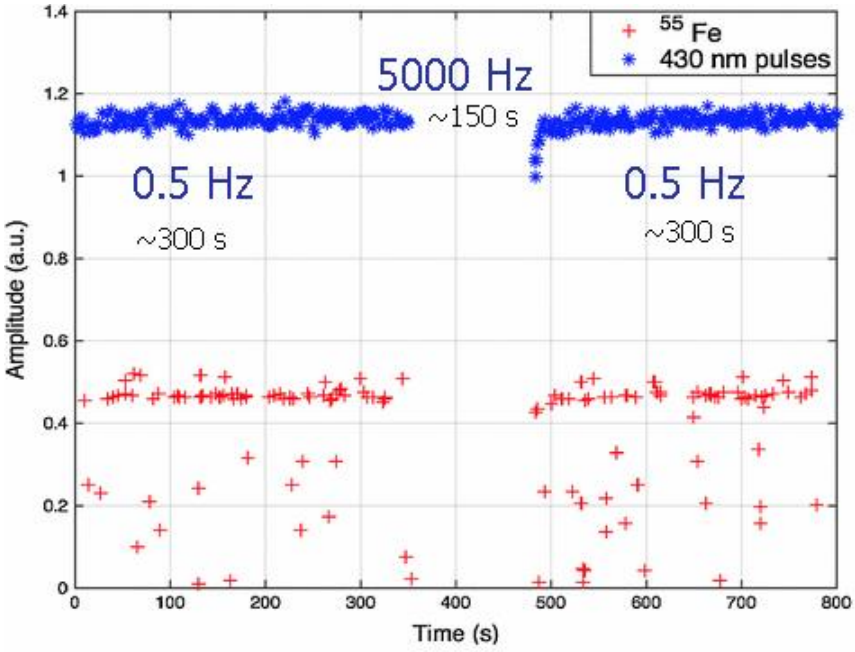


Figure 7.13: In this graph, the signal amplitude is shown for 430 nm photons at 97 $V_{NTL}$ for different photon's fluxes. The first 300 s, the flux has a rate of 0.5 Hz. For the next 150 s the flux is increased to a rate of 5000 Hz. After that time, the flux is back to 0.5 Hz. Since the value of the amplitude gets reestablished after setting the detector in pile-up mode (during the high flux), it is possible to determine that the detector does not degrade. Source: [63].

## 7.6 Measurements for different wavelengths

Other interesting experiments to perform on NTLE-detectors consist of studying this effect for different light sources. section 7.3 already showed how the photon's wavelengths influence the charge collection of the detector. In previous sections the causes of this effect in terms of the penetration depth of the light source were discussed and how this can be an issue for low voltages.

It was also seen that the collection in forward bias was possible at low temperatures and low forward $V_{NTL}$ for 430 nm photons. After repeating this experiment for 950 nm photons (section 7.4.1 another striking result was seen. Having a look at fig. 7.14 the 950 nm photons (in red) have a different behaviour in the region from 0 V to 1.1 V compared to the 430 nm photons. However, this is not true for longer wavelengths which allow us to keep collecting the same way even for forward bias. An explanation for this relies again on the fact that 430 nm photons, due to their energy, can only reach the area near the B-junction where the electrode mainly recombines and at certain low voltages it is no longer possible to collect. The 950 nm interact in the bulk and thus the e-h pairs created are in the intrinsic part of the PIN-diode – they keep being accelerated by the intrinsic electric field of the diode

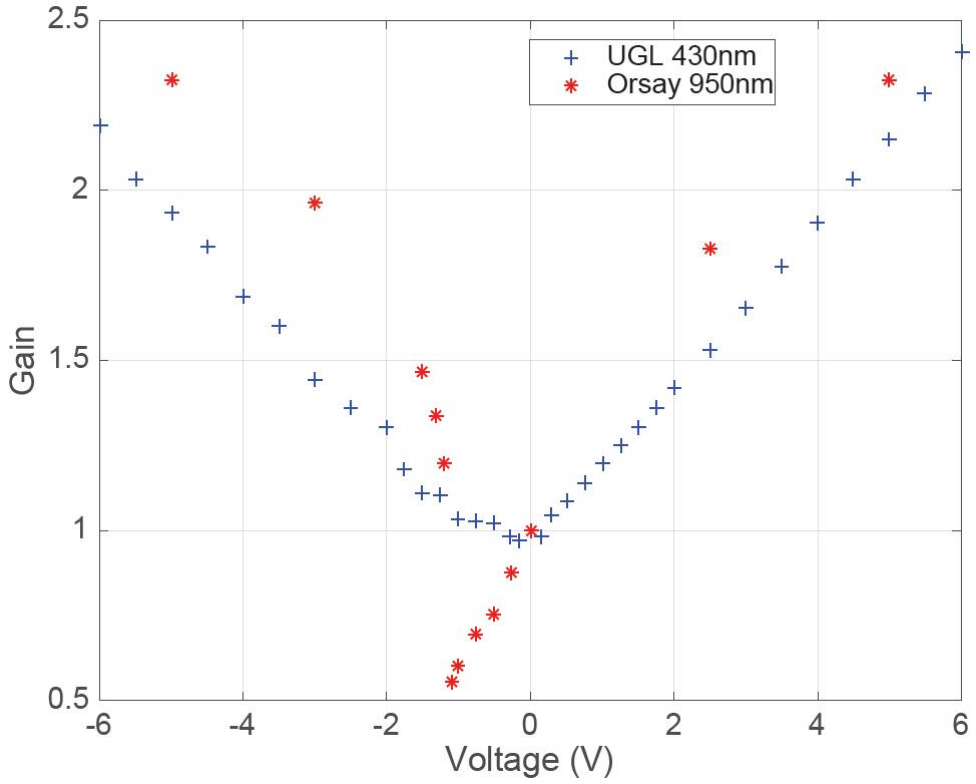


Figure 7.14: In this graph the gain for two different wavelengths at different $V_{NTL}$ are shown with both reverse and forward bias. In red are the data points for 950 nm photons and in blue for 430 nm photons. It can be seen how, due to the different penetration depths, the gain is different for both light sources. Meanwhile for the 950 nm photons the detector keeps collecting at 0 V and until a forward value equal to the Si gap (1.1 V), for the 430 nm photons the battery gets recharged. This experiment was performed in Orssay for a 10x10 $mm^2$ bare photodiode.

even when no-external voltage is applied. The 950 nm photons contribute at that point (between 0 and 1.1 V) to recharge the battery. When the forward voltage applied overcomes the value of the Si-gap (the 1.1 V), the polarity of the PIN-diode gets *inverted* and the collection of charges also inverts.

## 7.7 Detector time response

One of the results from the first experiment using a bare photodiode featured slow pulses, i.e., the slow rise of the pulse. A reason for this behaviour can be explained by the effect that the Al-layer at the back part of the detector exerted on the optical phonons. When the optical phonons reached this part of the photodiode they were rapidly absorbed by the Al lattice and did not reach the sensor.

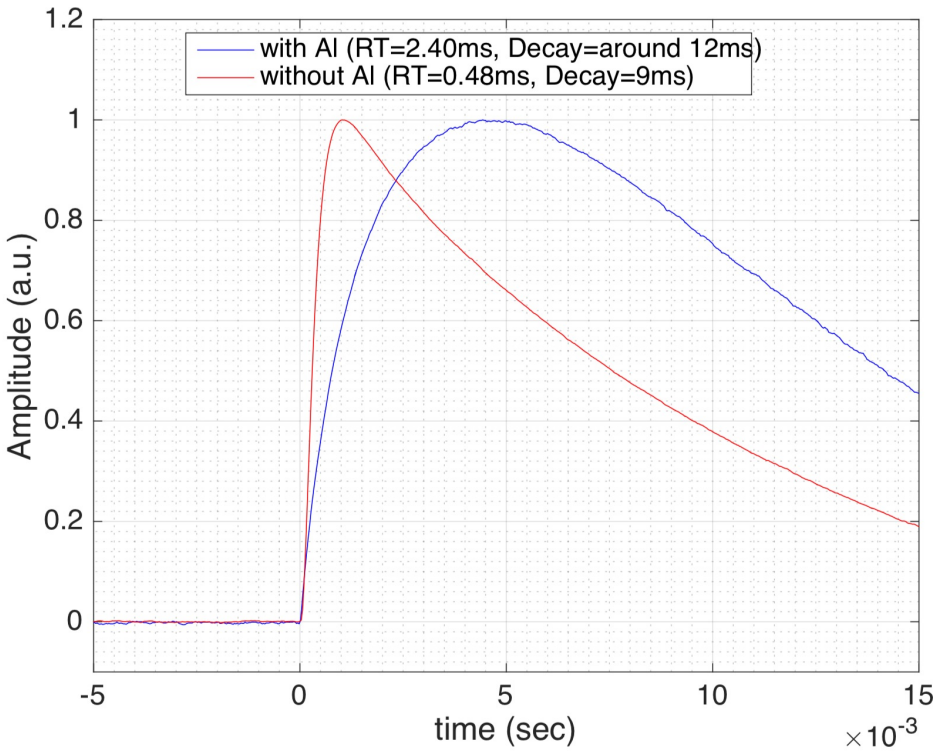


Figure 7.15: Rise time (10-90%) of a pulse from a detector with Al-layer (in blue) and one without Al-layer (in red) at the back part. Both detectors are 10x10 mm commercial Si-PIN diodes operated at ∼100 $V_{NTL}$. The rise time for detectors without Al is observed to be much smaller than the one with the Al.

One can try to understand this effect of the aluminum by analyzing this effect from the point of view of solid state physics. As was already mentioned, when a particle interacts inside the absorber a first burst of phonons is generated due to the initial recoil (so called optical phonons). It was seen that these optical phonons quickly thermalize becoming acoustic phonons. A phonon is a quanta of vibration within the crystal lattice and diffuses very well in the Si lattice. When the phonons arrive in the aluminum layer (which at this temperatures is a superconductor), they break some cooper pairs forming quasi-particles. In the ideal scenario, the quasi-particles diffuse in the aluminium until they reach the W-absorber (the energy gap of the W-Al region is smaller than the energy gap in the Al-region). Then this trapped energy produces a change in temperature that is read by the TES. In this sense the Al is working as a phonon collector. However, there is a trapping length for the quasi-particles in Al and this length is smaller than the width of the detectors used in this study (which are 10 mm wide, see appendix A).

Hence, a bare photodiode without this Al-layer on the back part was used. After measuring the rise time of the pulses obtained it is found that the performance of the detector was much faster (see fig. 7.15) and that the Al had actually an adverse effect in the time response of the detector.

All the diodes used for further experiments had this Al-layer removed. However, the Al-contacts at the front part which formed a squared thin frame around the active area, cannot be removed and still have an influence.

## 7.8 Experiments with APD

In section 6.3.5, the possibility to study the NTLE in an APD was introduced. In principle, the idea is that the avalanche effect characteristic of APDs would increase the gain tremendously.

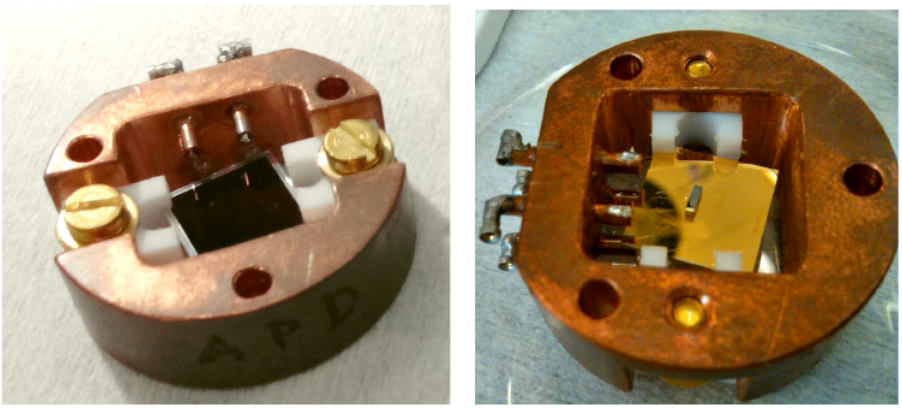


Figure 7.16: Left: Picture of the ADP photodiode used for the experiment. This image corresponds to the detecting surface of the diode. Right: Back part of the APD covered by an Au-layer. It can also be seen the NTD glued on the back part of the diode over the Au-layer.

Hence, an experiment using an APD was performed (see appendix A). However, the results were not as good as the ones obtained using PIN-photodiodes. It was observed that the amplification effect gradually decreases for temperatures below ∼40 K. This complicates the use of APDs for purpose here because this temperature is two orders of magnitude higher than the operational temperature required in the E15 experiments.

Additionally, the APD used here (fig. 7.16) had a golden layer on the back part of the diode which increased enormously the heat capacity of the detector.

## 7.9 Experiments with larger photodiodes

It is also interesting to study how the sensitivity and the amplification are affected when using larger photodiodes. To study that, two larger photodiodes were used

(see appendix A) which consisted of an 14x14 $mm^2$ and a 50x50 $mm^2$ bare Si photodiodes without Al layer on the back part of the diode (see Figures. 7.17 and 7.18). The diodes were also thicker with a thickness of 500 $\mu$m.

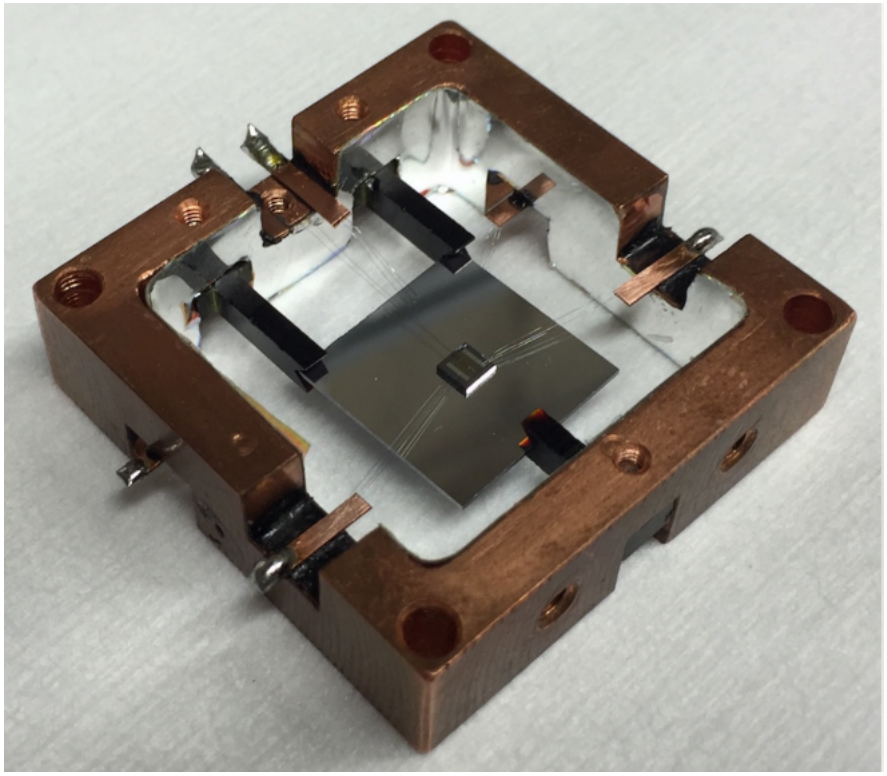

Figure 7.17: The 14x14 $mm^2$ photodiode. The glued TES can be seen on the back side.

In section 5.2.4 was seen that an increase in size implies an increase of calorific capacity. Increasing the calorific capacity has also effects on the energy resolution ($\Delta E \propto \sqrt{T^5 M}$). This effect could be seen especially on the 50x50 $mm^2$ photodiode. For this photodiode was also not possible to resolve the two lines of the $^{55}$Fe. Nonetheless, more tests have to be made with such a large photodiode to understand what was the cause of the low pulse height.

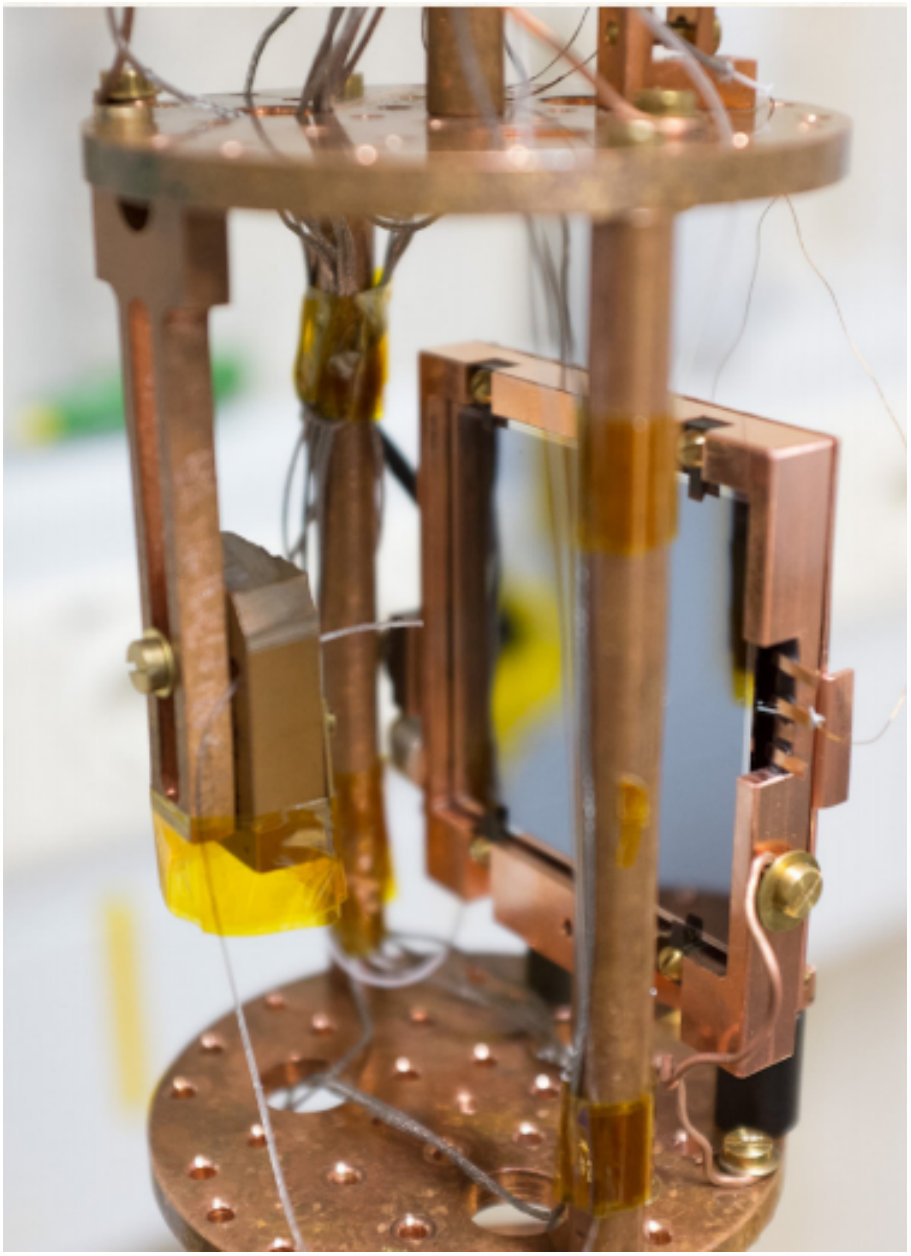

Figure 7.18: The 50x50 $mm^2$ photodiode mounted on the cryostat. The radioactive source can be seen in front of the diode.

# Chapter 8

# Conclusion and Outlook

In this thesis a new type of NTLE detector thought to improve the charge collection of the e-h pairs was investigated. PIN-photodiodes were used taking advantage of a planar geometry and implanted contacts. The proof of concept of a detector with implanted contacts was realised in the initial phase of the study. After validating this principle, several experiments were performed with photodiodes specially designed for this study. Dedicated experiments were made to measure the main characteristics of these detectors [63].

The main results from this study can be summarized as follows:

- The evolution of the charge collection versus the voltage applied for different photon wavelengths was analysed. It was discovered that for 430 nm photons, the bulk of the photodiode can be considered fully depleted for a $V_{NTL} \geq 40$ V. These measurements were crucial to understand the general behaviour of these detectors.

- The evolution of the thermal gain with $V_{NTL}$ was studied providing information about the value of the ratio $T/\epsilon$. The measured gain matches well the theoretical one when the eq. (5.2) transforms in eq. (7.1) providing the value of this ratio. Further experiments should be done to determine the evolution of the transmission T with temperature since the real value for the transmission of the detectors is not known at cryogenic temperatures. Also the $\epsilon$ needs to be determined to see if this value can changed from 70 K to mK temperatures. For the photons, $\epsilon_{photons} = E_\gamma/\eta$ the quantum efficiency $\eta$ can significantly change for Si at these temperatures. Thus, it is needed to study what is the temperature dependence of the quantum efficiency ($\eta(T)$) to evaluate the validity of 7.1. Nonetheless, the fact that the thermal gain yields values matching the theory is very important because shows a clear improvement on conventional NTLE-detectors.

- One of the main characteristics of the detectors studied in this work is the absence of degradation of the signal with time. This is very important for the

reliability of these detectors. It implies as well that regeneration processes are no longer needed.

- The $1\sigma$ baseline noise was measured in two different ways using the $^{55}$Fe and 430 nm photons (see section 6.6). The result exhibits an excellent baseline noise resolution of 5.33 $\pm$ 0.41 eV for the X-rays calibration and 5.00 $\pm$ 1.30 eV for the 430 nm photons calibration.

- The signal-to-noise ratio was improved by a factor $\sim$20 at 97 $V_{NTL}$ compared to the signals at 0 $V_{NTL}$.

- For the first time an NTLE detector exhibited an energy resolution close to the theoretical one for X-rays set by Poission statistics. This result is possible because of both the excellent charge collection on the whole surface of the photodiode and the none position dependence of the diode.

- The study of the impact of the aluminum layer on the collection of phonons showed a clear increase in the rise time of the detectors when the amount of aluminum on the surfaces is minimal. The rise time obtained was typically 300 $\mu$sec.

- The study of detectors with different sizes points out the influence of the heat capacity on the phonon signal. The sensitivity of the detectors is compromised by the increase in heat capacity (being the capacitance for semiconductors at low temperatures C $\propto$ $T^3$ and for electrons $\propto$ T as seen in section 5.2.4). However, it was not possible to determine the contribution to this heat capacity coming from the boron implantation in the entrance window. For the possible implementation of the planar geometry NTLE on the photon detectors in CRESST and other rare-events search experiments, that could benefit from larger photon detectors without compromising resolution, this point needs to be studied.

- Apart from the results that were the original aim of the study, some other interesting effects were discovered; at low temperatures it is possible to drift photo-generated charge carriers under forward voltage, without leak currents, until a maximum of $\sim$10 V on 10x10x0.2 $mm^3$ bare Si PIN-photodiodes.

- In this thesis the possible use of the NTLE in APDs proposed by [71] was also studied. Even though its use was restricted to the range of 20-40 K for PIN-photodiodes, this detector may be a good alternative for experiments that do not operate in the mK temperature range. A possible solution for using it at mK, is to thermally detach it from the rest of the system by maintaining it at a higher temperature, for example with a heater. For further investigations it would also be convenient to use an APD without the Au-layer.

Despite the excellent energy resolution, the resolution achieved is still a factor 4 away from the single photon detection of 430 nm photons. Reaching such a resolution

would be a great asset because it would constitute the ultimate resolution for a 430 nm light detector. It would also allow making a calibration of the photon detectors directly by just identifying the multiple photon peaks (single, double, triple peak...). A study of the different components of the noise must be implemented. The role of the dopants on the heat capacity and on the phonon collect will have to be evaluated. This study is necessary to increase the area of the photon detector while keeping good resolution performances. Additionally, the phonon collection will have to be optimized by increasing the ratio of the surface of the TES in comparison to the aluminum surfaces. The addition of an ARC-coating should also be implemented to increase the EQE.

# Appendix A

# Main features of the different diodes used for the experiments.

In the table A.1 the reader can find all the diodes organized chronologically, i.e., in the order in which the experiments were performed. In the table are also included the specific sensors used for every experiment. The transition curves of each TES used are depicted in appendix B. Additionally, the active area and main characteristics of every diode are provided, along with the main results obtained in the experiments conducted with them.

The sources used for most experiments are $^{55}$Fe and 430 nm photons. However, for some of the experiments other wavelength sources were used to study the effect of longer wavelengths under the NTLE. Not all of the wavelengths have been specified, alternatively, it has been pointed out the use of different wavelengths by writing "800 nm". In the case of the experiments performed in Orsay, only 950 nm-LED were available.

The sensors used for the experiments in Orsay are always NTD. TESs could not be used since the SQUIDs circuits were available only in Munich.

Table A.1: Diodes in chronological order.

| Diode | Period | Place | Sensor | Sources | Size(mm) | Characteristics | Results |
|---|---|---|---|---|---|---|---|
| Hamamatsu | Dec 2014 | UGL | TES (Si585H) | 430nm + $^{55}$Fe | 10x10 | Ceramic carcase covering one of the surfaces. Au contact on the detecting surface. TES glued on detecting surface. ARC coating. | Amplification achieved at low temperatures. Superimposed thermal signals coming from the TES and from the diode. |
| Canberra | Apr 2015 | UGL | TES (Si585H) | 430nm + $^{55}$Fe | 10x10, 300$\mu$m thick | Bare. Al Ohmic surface on the back part. | 100V amplification. Resolution of $^{55}$Fe. Well defined individual pulses. |
| Canberra | Oct 2015 | Orsay | NTD | 950nm + $^{55}$Fe | 10x10, 300$\mu$m thick | NTD was glued without removing the TES. NTD was removed after the experiment. The same Voltage supplier (300V) was used. T( mK). | Radiactive source was not powerful enough to be able to see it and LED pulses very small. |
| Canberra NA 1 | Oct 2015 | Orsay | NTD | 950nm + $^{55}$Fe | 10x10, 300$\mu$m thick | This diode it is like Canberra but without Al on the surface. NTD was removed after the experiment. | Faster pulses. |
| APD | Oct 2015 | Orsay | NTD | 950nm + $^{55}$Fe | 10x10, 300$\mu$m thick | Au layer on the back surface. | Amplification lost $\leq$ 40 K. |
| Canberra NA 2 | Nov 2015 | UGL | TES | 430nm -800nm + $^{55}$Fe | 10x10, 300$\mu$m thick. | This diode it is like Canberra NA 1. | Faster pulses and excellent energy threshold and resolution. |
| 16x16 | Feb 2016 | UGL | TES (J0) | 430nm -800nm + $^{55}$Fe | 14x14, 500$\mu$m thick. | Surface are much larger. TES glued on the bottom. No Al on the surface. | Worse energy resolution. |
| Diodezzila | Feb 2016 | UGL | TES (I0) | 430nm -800nm + $^{55}$Fe | 50x50, 500$\mu$m thick. | Surface are much larger. TES glued on the bottom. No Al on the surface. | Worse energy resolution. |

# Appendix B

# Transition curves of the TESs used in the different experiments.

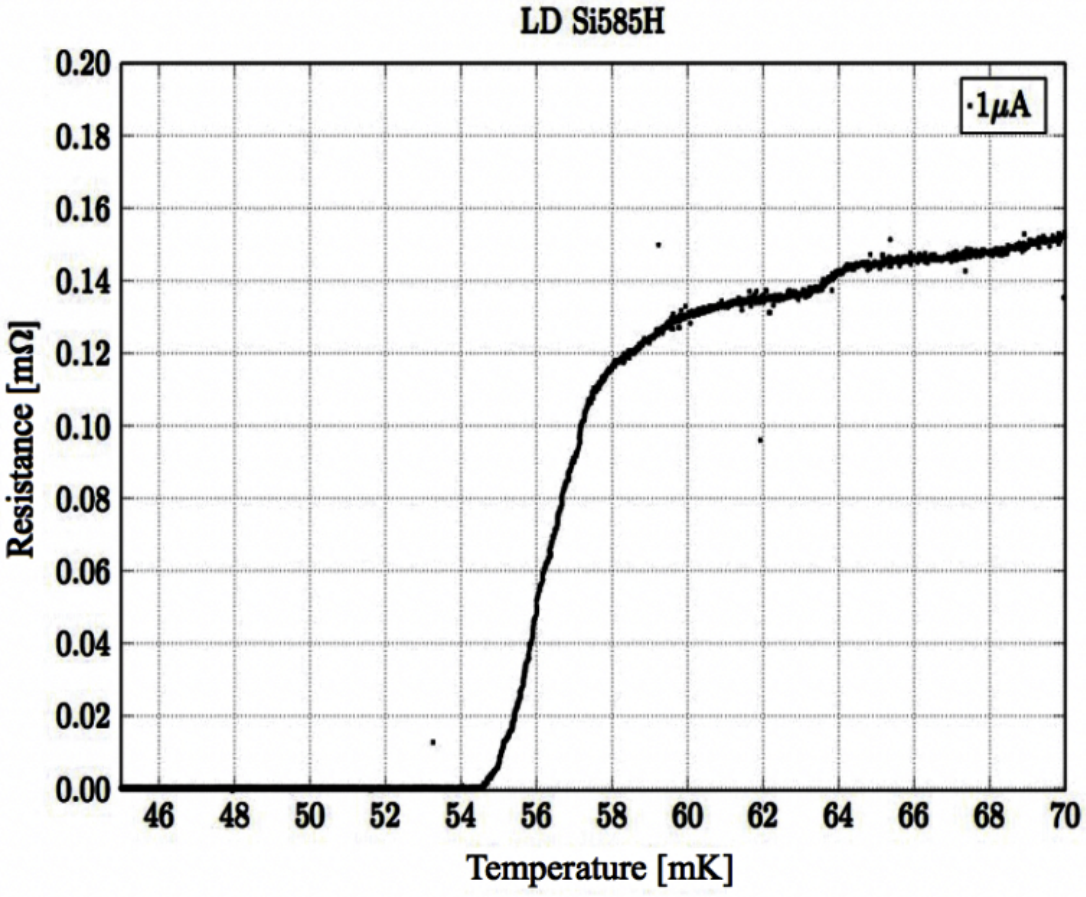


Figure B.1: Transition curve corresponding to the TES-Si585H.

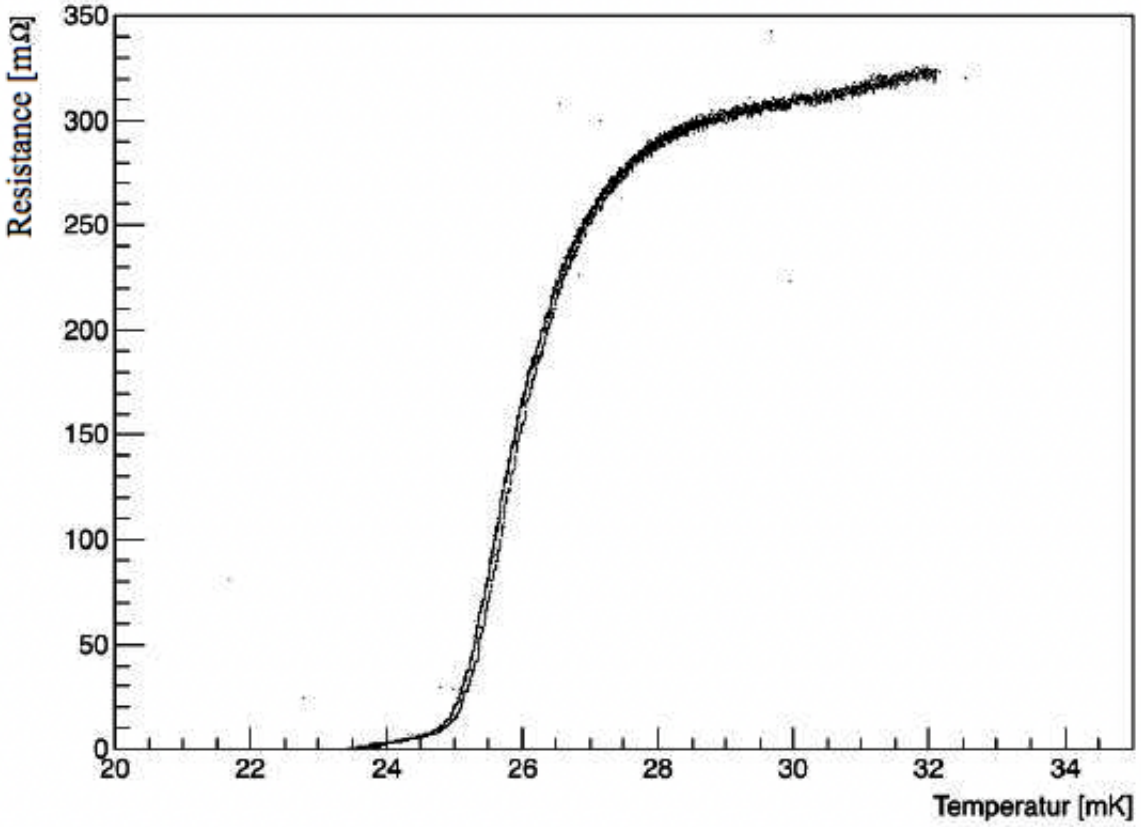


Figure B.2: Transition curve corresponding to the TES-IO.

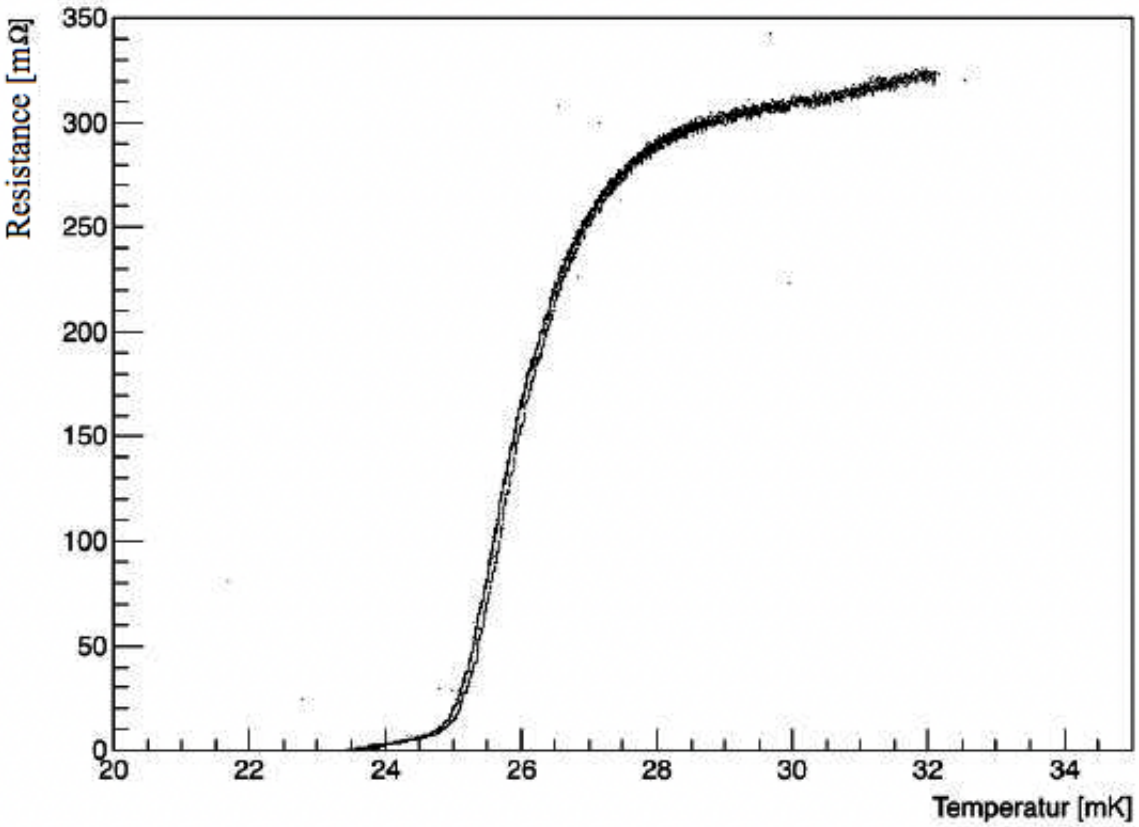


**Figure 4: # 20150615 I0**

Figure B.3: Transition curve corresponding to the TES-JO.

# Appendix C

# Dilution Refrigerator

The cryostat used for our experiments is a dilution refrigerator, a cryogenic device proposed in the 1950s by Heinz London.

To refrigerate uses a mixture of $^3$He and $^4$He. This mixture undergoes spontaneous phase separation into a concentrated and a diluted $^3$He one, when the temperature is below $\sim$ 800 mK. The diluted phase contains about 6.6% of $^3$He. In the mixture chamber the two phases are in equilibrium and separated by a phase boundary.

At equilibrium, the $^3$He flows from the concentrated phase through the boundary into the dilution phase – the heat required for the dilution is the cooling power of the refrigerator. Since both phases are at equilibrium, it is necessary that the concentration remains constant, which induces the dilution process. The transfer of the $^3$He is an endothermic process and thus, it removes heat from the mixing chamber environment while the entropy increases following the equation:

$$dQ = TdS \tag{C.1}$$

Using a U-tube, the $^3$He from the dilute phase is pumped up cooling down the downward flowing through the heat exchangers (see fig. C.1) until it reaches the still. In the still the pressure is kept at about 10 Pa and the temperature at 500-700 mK. Under these conditions, $^3$He is in vapor-state flowing through super-fluid $^4$He. The difference in pressure in the still and in the mixing chamber, creates an osmotic pressure that drives $^3$He from the concentrated to dilute phases in the mixing chamber, and then up from the mixing chamber to the still. Heat is supplied to the still to maintain a steady flow of $^3$He. The pumps compress the $^3$He to a pressure of a few hundred millibar and feed it back into the cryostat, completing the cycle.

The cryostat in the UGL is an OXFORD Kelvinox100 Cryostat (fig. C.2)

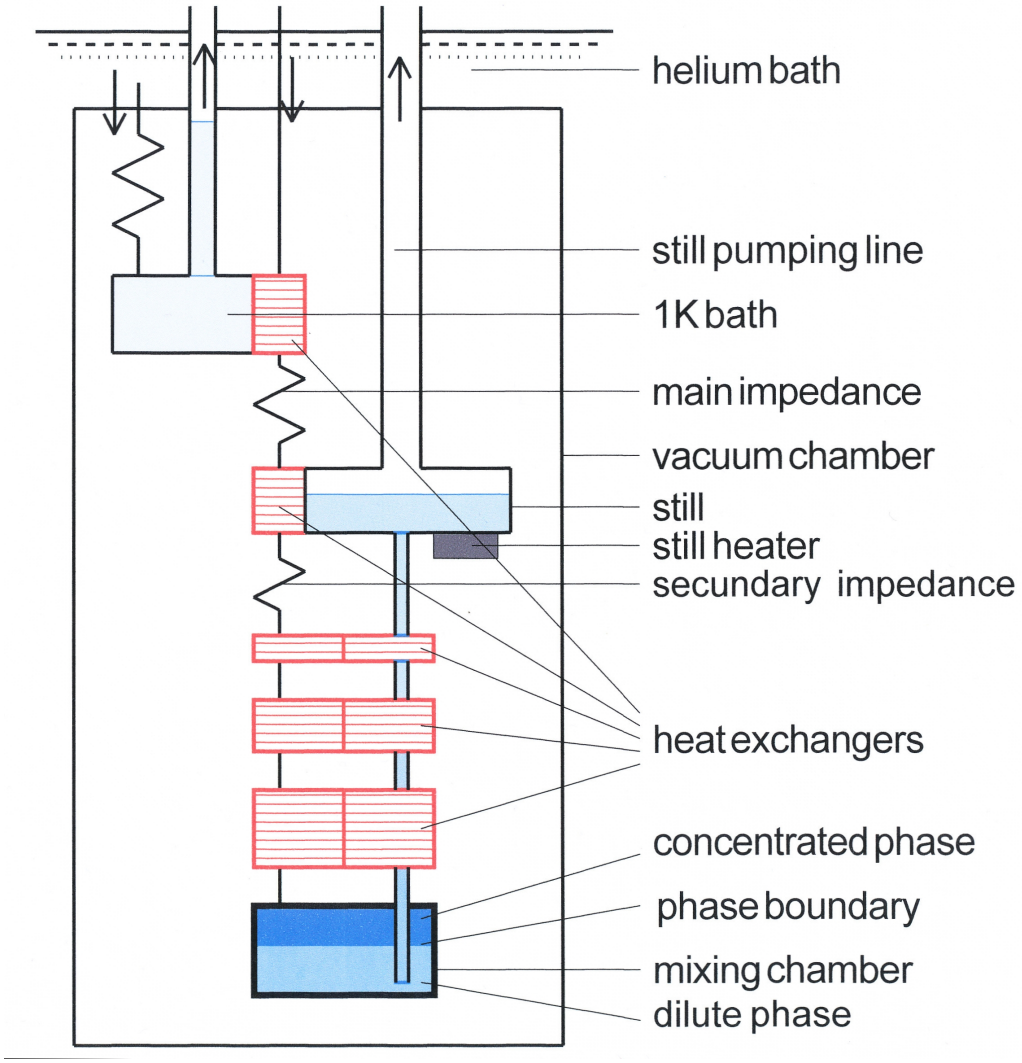


Figure C.1: It can be seen in this scheme the different parts involved in the cooling process in a dilution refrigerator.


Figure C.2: This picture corresponds to the cryostat OXFORD Kelvinox100 used for the experiments performed at the TUM.

# Appendix D

# Extension on the choice of the absorber

At room temperature, the use of Si presents another important advantage over Ge. The band-gap value for Si (0.7 eV) is higher in comparison with that of the Ge (0.2 eV). The generation of e-h pairs is for this reason smaller in Si, which might seems in principle a disadvantage.

However, this also implies that the reverse current in a Si PIN-diode ($\sim$nA) is smaller than for Ge ($\sim \mu$A) and that Si can withstand higher voltages compared to Ge before leak currents appear.

This is the reason why Ge photodiodes need a smaller voltage to break down in reverse bias ($\sim$ 50V) whereas Si retains it to a larger extent (70-100 V). This allows amplifying the signal also to a larger extent which is crucial for exploiting the NTLE (see FigD.1). Bear in mind though, that is behaviour is characteristic at room temperature, it cannot simply be assumed that in the range of $\sim$mK the same behaviour holds.

Ge has one major advantage over Si though: Its higher electron and hole mobility. This last aspect is very important for the case of lateral field configurations, where the e-h pairs need to travel a larger distance to the electrodes because trapping length and mobility are strongly correlated.

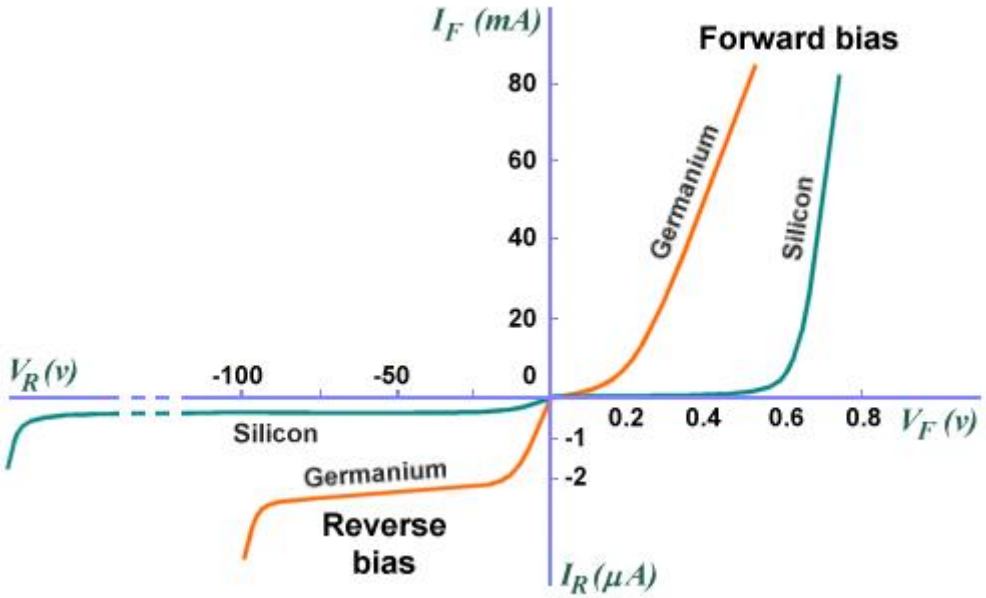


Figure D.1: In this current vs. voltage plot the curves for Si (in green) and Ge (in orange) for different voltages applied are shown. It can be seen that Si can withstand a much higher voltage than Ge before leak currents appear in both the reverse and the forward bias regimes. Source: [79].

# Acknowledgements

I would like to express my gratitude to my supervisor, Dr. Xavier Defay, for his useful comments, remarks, and engagement throughout the learning process of this master's thesis. The door to Xavi's office was always open whenever I ran into a trouble spot or had a question about the research or writing. He consistently steered me in the right direction whenever he thought I needed it, and was extremely patient with me throughout this process.

I am also very grateful to Prof. Dr. Stefan Schönert for being incredibly supportive, for his remarks, and especially for the great learning opportunity I had while working at the E15. Furthermore, I would like to thank Dr. Jean-Côme Lanfranchi for introducing me to the topic and to this wonderful group. I also want to thank Prof. Dr. Lothar Oberauer for all his help and support.

I would also like to thank the experts who were involved in the validation survey for this research project and contributed valuable ideas to this work: Dr. Walter Potzel, Dr. Andreas Ulrich, Dr. Emiliano Olivieri, Dr. M. P. Chapellier, and Dr. Michael Willers. Without their passionate participation and input, the validation survey could not have been successfully conducted.

I would also like to acknowledge James as the second reader of this thesis, and I am deeply indebted to him for his very valuable comments.

Thanks also to the Seed Money Project from the Excellence Cluster Universe for their funding support.

I would like to thank the entire E15 for being such a special workplace. In particular, thanks to Birgit, Christoph, and Konrad for their help and for the good moments we shared during this period.

Finally, I must express my profound gratitude to my loved ones for providing me with unfailing support and continuous encouragement throughout my years of study and during the process of researching and writing this thesis. This accomplishment would not have been possible without them. Thank you.

E. M. C.

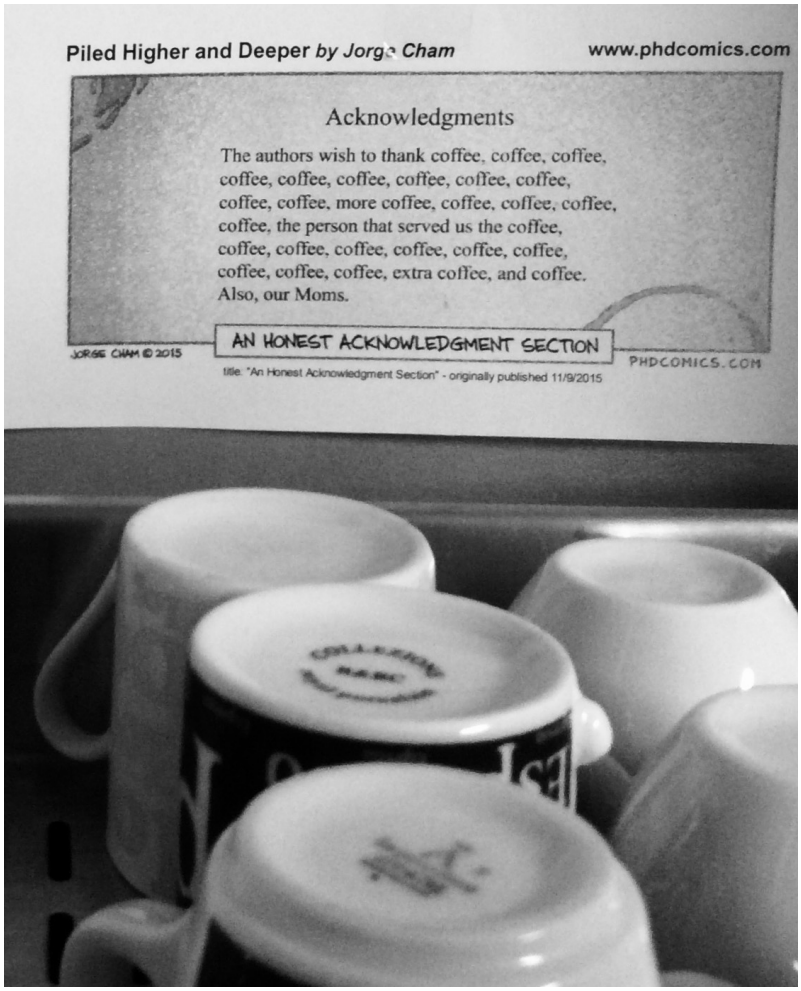


Figure D.2: Detail of the E15 seminar room at the TUM.

# Bibliography


[1] Francis, Matthew (22 March 2013). "First Planck results: the Universe is still weird and interesting". Arstechnica

[2] Zwicky, F., *Astrophysical Journal* **86: 217**., (1933)

[3] V. Rubin, N. Thonnard, W. K. Ford, Jr, *Astrophysical Journal* **238: 471**., (1980)

[4] S. W. Allen, P R. W. Schmidt and A. C. Fabian, *Mon. Not. R. Astron. Soc.* **334, L11–L15** (2002)

[5] www.hep.shef.ac.uk

[6] ESO/L. Calçada

[7] M. Markevitch et al. *The Astrophysical Journal* **606.2** (2004)

[8] Jennifer K.; Abazajian Kevork N.; Adelman-McCarthy. *The Astrophysical Journal Supplement* **182, Issue 2** (2009)

[9] Volker Springel, Simon D. M. White, and Adrian Jenkins. *Nature* **435** (2005)

[10] "Flanck reveals an almost perfect Universe". Max Planck Gesellschaft. (2013)

[11] ESA and the Planck Collaboration

[12] Chandra X-ray Observatory

[13] Lars Bergström, *Rep.Prog.Phys.* **63, 793–841** (2000)

[14] J. L. Feng, *arxiv:1003.0904v2* (2010)

[15] Anthony H. Gonzalez Douglas Clowe Marusa Bradac. *The Astrophysical Journal Letters* **648.2** (2006)

[16] Bulbul, E. et al. *ApJ* **789, 13** (2014)

[17] Boyarsky, A., Ruchayskiy, O., Iakubovskyi, D. & Franse, J. *Phys. Rev. Lett.* **113, 251301** (2014)

[18] James Bateman, Ian McHardy, Alexander Merle, Tim R. Morris & Hendrik Ulbricht. *Scientific Reports, Nature* **5, 8058** (2015)

[19] R. J. Scherrer and M. S. Turner. *Phys. Rev* **D33, 1585** (1986)

[20] E. W. Kolb and M. S. Turner. *Front.Phys.* **69, 1** (1990)

[21] http://fermi.nasa.gov

[22] P. Meunier, et al., *Appl. Phys. Lett.* **75** (1999)

[23] CRESST Collaboration, G. Angloher et al., *Astropart. Phys.* **23, 325**, (2005)

[24] R. Strauss, et al., *The European Physical Journal C.* **74:2957**, (2014)

[25] A. Münster, et al., *JCAP05*, **018**, (2014)

[26] R. Strauss, et al., *Journal of Cosmology and Astroparticle Physics*, **Volume 2015**, (2015)

[27] K. D. Irwin and G. C. Hilton, *Topics Appl. Phys.*, **99, 63-149**, (2005)

[28] J. Clarke, A. I. Braginski, *Vol. I Fundamentals and Technology of SQUIDs and SQUID Systems.*, **ISBN: 3-527-40229-2**, (2004)

[29] D. Drung, et al., *IEEE Transactions on Applied Superconductivity.*, **17 (2), 699–704** , (2007)

[30] F. Reindl, *(Dissertation), Max-Planck-Insitut* für *Physik and Technical University of Munich.*, (2011)

[31] M. Aglietta, et al., *Astroparticle Physics*, **Volume 2, Issue 2, 103-116.**, (1994)

[32] A. Drukier and L. Stodolsky. *Phys. Rev.*, **D 30, 2295**, (1984)

[33] Lars Bergström, *Ann. Phys.*, **524, No. 9–10, 479–496**, (2012)

[34] Agnese, R. et al., *Run. Phys. Rev. Lett.*, **116**, (2016)

[35] http://cresst.de

[36] The CRESST Collaboration, *The European Physical Journal C.*, **76:25**, (2016)

[37] A. Gütlein et al., *Astroparticle Physics*, **69, 44-49**, (2015)

[38] XENON100 Collaboration, *Phys. Rev. Lett.*, **109, 181301**, (2012)

[39] LUX Collaboration, *arXiv:1608.07648*, (2016)

[40] L. Hehn et al. *Eur. Phys. J.*, **C76, 548** (2016)

[41] R. Bernabei et al., DAMA Collaboration *Eur. Phys. J. C.*, **56, 333-355** (2008)

[42] C. E. Aalseth et al., CoGeNT Collaboration, *Phys. Rev. Lett.*, **106, 131301** (2011)

[43] Z. Ahmed et al., The CDMS-II Collaboration, *Science.*, **327, 1619–1621** (2010)

[44] E. Aprile et al., XENON100 Collaboration, *Phys. Rev. Lett.*, **105, 131302** (2010)

[45] S. C. Kim et al., *Phys. Rev. Lett.*, **108, 181301** (2012)

[46] http://lumineu.fr

[47] H.J. Lee et al., *Nuclear Instruments and Methods in Physics Research A.*, **784, 508–512** (2015)

[48] G. B. Kim et al., *Advances in High Energy Physics.*, **817530** (2015)

[49] G. B. Kim et al., *arXiv:1602.07401*, (2016)

[50] R. Agnese, et al., *Phys. Rev. Lett.*, **112, 041302**, (2014) .

[51] E. Armengaud, et al., *Phys. Rev. D.*, **86, 051701**, (2012) .

[52] R. Strauss, et al., *XIV International Conference on Topics in Astroparticle and Underground Physics, IOP Publishing Journal of Physics: Conference Series.*, **718, 042048**, (2016)

[53] R. Strauss, et al., The CRESST Collaboration, *Nuclear Instruments and Methods in Physics Research Section A.*, **0168-9002** (2016)

[54] The CRESST Collaboration., *Astroparticle Physics*, **Volume 31, Issue 4, 270–276**, (2009)

[55] F. Pröbst, et al., *J. Low Temp. Phys.*, **100 69–104**, (1995)

[56] M Shubin, T. Sunada, *Pure and Appl. Math. Quarterly.*, **2: 745–777**, (2006)

[57] B. Neganov, V. Trofimov, *Otkryt. Izobret.*, **146** (1985)

[58] P. N. Luke, *J. Appl. Phys.*, **64** (1988)

[59] M. Willers, *(Dissertation), Technical University of Munich.*, (2015)

[60] M. Willers, et al., *Journal of Instrumentation.*, **10, P03003** (2015)

[61] A. Münster et al. *Nucl. Instrum. Methods Phys. Res. A.*, (2016)

[62] A. Langenkämper, *(Master's Thesis), Technical University of Munich.*, (2016)

[63] X. Defay, E. Mondragon et al., *J Low Temp Phys.*, **184, Issue 1, 274–279.**, (2016)

[64] M. Stark, et al., *Nucl. Instrum. Methods Phys. Res. A.*, **545, p. 738** (2005)

[65] C. Isaila *(Dissertation), Technical University of Munich.*, (2009)

[66] C. Isaila et al., *Physics Letters B.*, **716** (2012)

[67] S. Roth, *(Dissertation), Technical University of Munich.*, (2013)

[68] C. Isaila, et al., *Nucl. Instrum. Methods Phys. Res. A.*,**559, 309-401** (2006)

[69] M. A. Green and Keevers, M. J., *Progress in Photovoltaics: Research and Applications.*, **vol. 3, pp. 189 - 192**, (1995)

[70] Martin A. Green., *Solar Energy Materials and Solar Cells.*, **92:1305–1310**, (2008)

[71] Chapellier, M.P. *J Low Temp Phys*, (2015)

[72] G. Bertolini, A. Coche, *Elsevier-North Holland Publ. Co.*, (1968)

[73] V.S. Vavilov, *Phys. Chem. Solids.*, **8, 223**, (1959)

[74] E. Simoen et al.,*Journal of Applied Physics*, **70, 1016**, (1991)

[75] D. D. Coon and S. D. Gunapala, *Journal of Applied Physics*, **57, 5525**, (1985)

[76] E. Pascaa et al., *Nuclear Instruments and Methods in Physics Research Section A.* **575, 3** (2007)

[77] K.D. Irwin *Appl. Phys. Lett.*, **66, p. 1998**, (1995)

[78] A. Peruzzi et al., *Metrologia*, **37 (2), p. E1143**, (2000)

[79] www.technologyuk.net